2002

Effects of Heat Treatment on Microstructure and Mechanical Properties of a Near-a Titanium Alloy

Jose C. Arteiro
University of Rhode Island

EFFECTS OF HEAT TREATMENT ON MICROSTRUCTURE AND MECHANICAL PROPERTIES OF A NEAR-α TITANIUM ALLOY

BY

JOSÉ C. ARTEIRO

A THESIS SUBMITTED IN PARTIAL FULFILLMENT OF THE

REQUIREMENTS FOR THE DEGREE OF

MASTER OF SCIENCE

IN

MECHANICAL ENGINEERING AND APPLIED MECHANICS

UNIVERSITY OF RHODE ISLAND

MAY 2002

MASTERS OF SCIENCE THESIS

OF

JOSÉ C. ARTEIRO

APPROVED:

Thesis
Committee:

Major
Professor Hamouda Ghoneim

DEAN OF THE GRADUATE SCHOOL

Abstract

This thesis is concerned with the effect of heat treatment on the microstructure of the near-α titanium alloy IMI 834. Furthermore, it investigates the crack growth rate behavior in two microstructures of this alloy differing in their primary alpha (α_p) volume fractions. IMI 834 is an aerospace high temperature material that possesses the highest creep resistance of duplex near-alpha alloys at temperatures up to 650°C. A series of heat treatment experiments are carried out to examine the influence of recrystalization temperature, cooling rate, aging time and over-aging time, on the volume fractions of the primary alpha as well as the corresponding hardness characteristics. It is shown that for α_p volume fractions up to 20%, colony size decreases with increasing the volume fraction. For higher α_p volume fractions, the colony size remains relatively constant. Results show that between approximately 10% and 30% α_p volume fractions, the material has a constant hardness, defined by the cooling rate. On the other hand, the hardness decreases significantly for volume fractions lower than 10% and for volume fractions higher than 30%. It is also found that element partitioning effects are most dominant in volume fractions above 30%. Over-aging specimens with 5%, 23% and 39% α_p volume fractions at 650°C shows that only S_2 type silicides precipitated in IMI 834. Furthermore, results show that the critical silicide size is achieved at about the same over-aging period, 2,000 minutes, for α_p volume fractions greater than 23%. Over-aging the material with 5% α_p volume fraction results, however, in precipitation of S_2 type silicides after a shorter time, 80

minutes, and a noticeable increase in hardness is observed when compared with that of the other two microstructures. The influence of two selected α_p volume fractions, 20% and 30%, on the fatigue crack growth rate (FCGR) is examined at 650°C for three different loading frequencies, 10 Hz, 0.05 Hz, and 0.003 Hz. It is shown that for the 10 Hz and 0.05 Hz tests, the FCGR is similar in the two microstructures. The fracture mechanisms under these two test conditions involves transgranular cracking of both the α/β colony and the α_p particles. For the loading frequency of 0.003 Hz, the fatigue crack growth is higher in the 30% α_p volume fraction than in the 20%. For this loading condition, the fracture mechanism involves transgranular cracking in the α/β colony accompanied by interboundary cracking in the α_p particles. These fracture mechanisms are discussed and explained in terms of phase strength and toughness as well as silicide density and size in each of these two microstructures.

Acknowledgements

Firstly, I would like to extend my gratitude and appreciation to Dr. Hamouda Ghonem for the opportunity he gave me to work on this thesis. His perseverance on excellence has driven me to new heights in my studies.

In addition, I would like to thank Dr. Frederic Sansoz who helped me in every step of this thesis and continuously provided me with ideas, guidance and support.

TIMET Corporation of Henderson, Nevada, U.S.A, has supplied all the IMI 834 material used in this study.

My sincere gratitude to my friends, colleagues, faculty and staff in the Mechanical Engineering Department and the Naval Undersea Warfare Center who made my graduate school experience a pleasant one. In particular, I would like to acknowledge Dr. Robert Koch and Robert Doleski, David LePagne and Debbie Osborne.

Thank you Naval Undersea Warfare Center (NUWC) Long Term Training (LTT) selection committee for putting your trust in me, and NUWC for allowing me the opportunity to fulfill my goal of completing my Master's degree.

To my beautiful wife, Françoise and my children, Mary and Henry, my eternal thanks for making me want to be a better man. Thank you Mom, Dad, Sister and Grandma for your words of support and your prayers when I needed them most. I love you all.

Table of Contents

ABSTRACT ..... **II**

ACKNOWLEDGEMENTS ..... **IV**

TABLE OF CONTENTS ..... **V**

LIST OF FIGURES ..... **VIII**

CHAPTER 1: INTRODUCTION **1**

CHAPTER 2: ROLE OF HEAT TREATMENT IN TI-ALLOYS **6**

INTRODUCTION: 6

2.1 REVIEW OF NEAR-ALPHA TITANIUM ALLOYS 6

2.1.1 Role of Alloying Elements *6*

2.1.2 Example of Near-α Alloys and their Mechanical Properties *12*

2.1.3 Processing and Heat Treatment of Duplex Microstructures *19*

2.1.4 Effects of Heat Treatment on Mechanical Properties *25*

2.2 MATERIAL OF THE STUDY 33

2.2.1 Effect of Heat Treatment on Phases Morphology *33*

2.2.1.1 Experimental Procedure 34

2.2.1.2 Results and Analysis 37

2.2.2 Influence of Heat Treatment on the Hardnesss of IMI 834 ..... *44*

2.2.2.1 Experimental Procedure 44

2.2.2.2 Results and Analysis 47

2.3 SUMMARY AND CONCLUSIONS OF CHAPTER 2 56

CHAPTER 3: LONG TERM EXPOSURE EFFECTS AT 650^{O}C ON THE STRUCTURAL STABILITY OF NEAR-α ALLOYS **58**

INTRODUCTION: 58

3.1 ROLE OF LONG TERM EXPOSURE AT ELEVATED TEMPERATURE ON THE STRUCTURAL STABILITY OF TITANIUM ALLOYS 58

3.1.1 Effects of Over-Aging on Aluminides *61*

3.1.2 Effects of Over-Aging on Silicides *63*

3.1.3 Role of Over-Aging on Room Temperature Hardness *73*

3.1.4 Summary on the Role of Aluminide and Silicide Formation in Ti-Alloys *83*

3.2 SIGNIFICANCE OF OVER-AGING ON IMI 834 AT 650°C 83

3.2.1 Experimental Procedure *84*

3.2.2 Results and Analysis *86*

3.3 SUMMARY AND CONCLUSIONS FOR CHAPTER 3 91

CHAPTER 4: FCGR OF IMI 834 AT 650°C 93

INTRODUCTION: 93

4.1 EXPERIMENTAL PROCEDURE 95

4.2 EXPERIMENTAL RESULTS 101

4.3 DISCUSSION 111

3.2 SUMMARY OF CHAPTER 4 RESULTS 116

APPENDIX A 117

BASIC MECHANISMS OF CREEP AND FATIGUE FRACTURE 117

LIST OF REFERENCES 127

BIBLIOGRAPHY 133

LIST OF TABLES

Table 2-1: Characterization of Ti-alloys based on Al and Mo equivalent concentrations (from ref. [53]). 10

Table 2-2: Composition of selected near-alpha titanium alloys (from ref. [16]). 15

Table 2-3: Mechanical properties at room temperature of selected near-alpha titanium alloys (from ref. [16]) 15

Table 2-4: Element partitioning on Ti-6-22-22 following solution treatment at 1000°C for 1-hour, heat treatment at 925°C for 1 hour, and aging at 540°C for 8-hours (from reference [40]). 31

Table 2-5: Tensile properties at RT and 600°C in IMI 834 (from ref. [13]). 32

Table 3-1: Average size of silicides after oil quenching different solution treatments for 2-hours followed by aging at 700°C for 2-hours on IMI 834 (from reference [44]). *(Size determination from projected images a and b refers to major and minor axes of the projected ellipsoid). 66

Table 3-2: Average size of silicides after water quenching solution treatments at 1050°C and aging for 24-hours followed by air-cooling at various temperatures on IMI 829 (from reference [19]). *(Size determination from projected images a and b refers to major and minor axes of the projected ellipsoid.). 68

Table 4-1: List of microstructures and corresponding loading frequencies for fatigue crack propagation testing of IMI 834 at 650°C. 105

List of Figures

Figure 2-1: Classification scheme for binary alloys of titanium based on phase diagrams (from ref. [12]). 8

Figure 2-2: Main characteristics of the different titanium alloy families (from ref. [2]). 9

Figure.2-3: Effect of silicon content on the creep behavior of IMI 834 alloy (from ref. [11]) 14

Figure.2-4: Aluminum and molybdenum equivalencies for Titanium Alloys (from ref. [32]) 16

Figure.2-5: Creep properties in Ti6242 alloy, IMI-834 alloy and Ti-1100 alloy with α/β and β processing as indicated (from ref. [8]). 18

Figure 2-6: Microstructure of IMI 834 (heat-treated and aged to 23% α_p volume fraction). 21

Figure 2-7: Thermal cycle applied in duplex microstructures (β transus in IMI 834 occurs at approximately 1060°C [21]) 22

Figure 2-8: Schematic of the mechanism of globularization from lamellar microstructures: (a) unrecrystalized, (b) beginning of recrystalization, (c) α_R moving into a side plates, (d) α_R consuming into a side plates (from ref. [51]). 24

Figure 2-9: Schematic of the mechanism of globularization at grain boundary (from ref. [52]). 24

Figure 2-10: Important processing parameters, resulting microstructural features, and major influences on mechanical properties (arrows) for duplex microstructures (from ref. [13]) 26

Figure 2-11: Effect of cooling rate on creep strain of near-α titanium alloy IMI 834 (from ref. [13]) 28

Figure 2-12: Influence of slip length (α colony size) on mechanical properties (schematically) (from ref. [13]). 29

Figure 2-13: IMI 834 pancake with water jet cuts. 36

Figure 2-14: Water-quenched IMI 834 microstructures 39

Figure 2-15: Air-cooled IMI 834 microstructures. 40

Figure 2-16: Effects of aging on the α_p volume fraction for air-cooled specimens of IMI 834. 41

Figure 2-17: Effect of cooling rate on the α_p volume fraction of IMI 834. 42

Figure 2-18: Colony size measurements from selected water-quenched specimens and from literature for IMI 834. 43

Figure 2-19: Schematic representation of Post Age Heat Treatment (PAHT) process in IMI 834. 46

Figure 2-20: Rockwell "C" hardness results for water-quenched/aged and air-cooled/aged IMI 834. 48

Figure 2-21: Stress-strain curves for α and β (from ref. [54]). 49

Figure 2-22: Effect of α_2 removal on hardness R_C in IMI 834. 52

Figure 2-23: Difference of Rockwell "C" hardness results for water-quenched/aged and water-quenched/aged/PAHT IMI 834. 53

Figure 2-24: Effect of PAHT on hardness of low and high α_p volume fraction of IMI 834. 54

Figure 2-25: Colony size and partitioning element effects for-water-quenched IMI 834 specimens. 55

Figure 3-1: Lattice Structure of α_2 (Ti_3Al) intermetallic. 60

Figure 3-2: Schematic representation of silicide average size and shape change with recrystalization temperature (from table 3-1). 67

Figure 3-3: Schematic representation of silicide growth and shape change with aging temperature over 24-hours (from table 3-2) 69

Figure 3-4: Schematic representation of TEM observations of IMI 829 aged for 24-hours at 625°C (from ref. [19]). 70

Figure 3-5: Schematic representation of TEM observations of IMI 829 aged for 24-hours at 700°C (from ref. [19]). 71

Figure 3-6: Schematic representation of TEM observations of IMI 829 aged for 24-hours at 800°C (from ref. [19]). 72

Figure 3-7: Effects of temperature on the aging characteristics of Ti-5%Zr-1%Si (from reference [45]). 77

Figure 3-8: Effects of silicon content on the aging characteristics of binary Ti-Si alloys at 550°C (from reference [45]).... 78

Figure 3-9: Effects of temperature on the aging characteristics of Ti-1%Si (from reference [45]). 79

Figure 3-10: Effects of aluminum content on the aging characteristics of the quaternary Ti-5%Zr-1%Si-Al alloy at 550°C (from reference [45]).....80

Figure 3-11: Effects of aging on air-cooled Ti-1100 heat treated at 1093°C and "stabilized" at 593°C for 8-hours (from ref. [49]).....82

Figure 3-12: Thermal cycle applied in duplex microstructures showing over-aging process. 85

Figure 3-13: Effect of over-aging on hardness R_C for water-quenched and aged 5%, 23%, and 39% α_p vf IMI 834. 90

Figure 4-1: Specimen geometry for fatigue crack growth testing (CT 12.5) and location of potential drop wires. V1 represents the potential drop across the crack mouth and V2 is the potential drop reference away from the crack. A pulsed 3 Amp current traverses this specimen. through the load train, as shown in Fig. 4-3. 98

Figure 4-2: MTS servo-hydraulic material testing system with clamshell furnace controlled by the Test Star IIS computer environment. 99

Figure 4-3: Clamshell furnace and loaded specimen with spot-welded thermocouples and Potential Drop (PD) wires.....100

Figure 4-4: IMI 834 solution treated at 1035°C for 2-hours and water-quenched followed by aging at 700°C for 2-hours (20% α_p vf). 103

Figure 4-5: IMI 834 solution treated at 1010°C for 2-hours and water-quenched followed by aging at 700°C for 2-hours (30% α_p vf). 104

Figure 4-6: Effect of loading frequency and 5 minute hold time at peak stress on Fatigue Crack Growth Rate of IMI 834 at 650°C. 106

Figure 4-7: Fracture surface on the 20% α_p vf specimen for test conditions (a) 10 Hz (b) 0.003 Hz. 107

Figure 4-8: Fracture surface on the 30% α_p vf specimen for test conditions (a) 10 Hz (b) 0.003 Hz. 108

Figure 4-9: Fracture path for test conditions 0.05 Hz on the (a) 20% α_p vf specimen (b) 30% α_p vf specimen. 109

Figure 4-10: Fracture surface showing the transition between test conditions 0.05 Hz and 0.003 Hz as well as between 0.003 Hz and failure on the 20% α_p vf specimen. 110

Figure 4-11: Schematic of possible crack path in both α/β colony and primary alpha: (a) trans-colony / trans-alpha particle; (b) trans-colony / inter-alpha boundary. 115

Figure A-1: Typical shape of a creep curve 120

Figure A-2: Typical shape of a fatigue curve 121

Figure A-3: Schematic representation of creep cause by climb-glide sequence. 122

Figure A-4: Schematic representation of diffusion creep 123

Figure A-5: Schematic representation of crack propagation by ductile tearing. 124

Figure A-6: Schematic representation of crack propagation by cleavage. 125

Figure A-7: Schematic representation of intergranular and transgranular fracture mechanisms. 126

Chapter 1: Introduction

Titanium and its alloys are extensively used in aerospace and industrial applications due to their lightweight, high ability to withstand extremes of temperature and excellent resistance to corrosion. For instance, titanium is lighter than steel with equivalent strength, and heavier than aluminum, but twice as strong. Pure titanium metal promotes an allotropic solid phase with very slow transformation at 883°C. Below 883°C, its crystalline form is hexagonal close packed (HCP), or alpha (α), whereas at temperatures above, its form is body centered cubic (BCC), or beta (β) [1]. The manipulation of these crystallographic variations is performed by the addition of alloying elements and the thermo-mechanical process. Alloying elements are classified according to their ability to change the temperature of either alpha or beta phase transformation [2]. Alpha stabilizing elements in titanium alloys are usually non transition metals, such as aluminum (Al) or gallium (Ga), as well as non-metals, such as oxygen (O) and nitrogen (N). Transition metals, such as molybdenum (Mo), niobium (Nb) and vanadium (V) are beta stabilizers [3, 4]. Based on its chemical composition and the predominant room temperature constituent phase(s), titanium alloys can be classified as α, near-α, α/β, or β-alloys [5-7]. Alpha alloys usually have creep resistance superior to that of beta alloys [8], but beta alloys offer increased fracture toughness at a given strength level [9]. Alpha alloys cannot be strengthened by heat treatment because the alpha structure is a stable phase, whereas beta alloys have excellent hardenability and response to heat treatment [2, 10]. The principal

alloying element in alpha alloys is aluminum. When these alloys contain small amounts of beta-stabilizing elements [10], they are classified as super alpha or near alpha alloys. Near-alpha titanium alloys are processed to achieve either equiaxed alpha microstructures, acicular transformed beta microstructures, or a mixture of equiaxed grains embedded within transformed beta matrix, so-called duplex microstructures. Acicular microstructures possess better creep resistance than duplex microstructures. On the other hand, the latter has excellent fatigue strength, crack initiation resistance and higher ductility [11-23].

The increase in performance requirements for use in turbine engines and other high temperature applications has led to demands of titanium alloys with combined high creep and fatigue resistance. In order to achieve that objective, a considerable amount of research has been carried out over the past decades to enhance the creep resistance of near-α Ti alloys with duplex microstructure. One of these alloys, IMI 834, is an advanced near-α titanium alloy designed for high temperature applications that exhibit a good compromise between creep and fatigue properties [26, 29, 31, 34-37] at temperatures up to 600°C [24-32]. In some applications, however, the alloy is already used for high-temperature components where temperature excursions reach 650°C [33]. Among the chemical changes in IMI 834, the addition of silicon has a major effect on the creep resistance and microstructure of the alloy. Silicon raises the creep resistance in titanium alloys by reducing dislocation movement [29]. Furthermore, silicon lowers the molybdenum content of the β-phase and consequently, for lower cooling rates, the β transforms

to orthorhombic martensite instead of α/β colonies [23, 38]. The most effective concentration of silicon in high-temperature alloys is governed by its tendency to form zirconium silicides. These are undesirable since studies have shown that the precipitates remove silicon from solid solution in the α phase and reduce ductility of the alloy [10]. Typically, silicides precipitate slowly at the aging or service temperatures of the alloys, resulting in a reduction in material stability. In addition to silicides, Ti_3Al precipitates, or α_2, also form during high temperature applications. Studies show, however, that α_2 stability is achieved after aging at 700°C for 2 hours only [22]. In order to understand the effects of alloying additions in titanium alloys, a large amount of studies have been carried out to relate the heat treatment [6, 9, 13, 32, 38-43] and the aging [20, 23, 44-49] with the associated mechanical properties up to 600°C. In particular, studies by Madsen and Ghonem [47, 49] on near-α Ti-1100 with basket-weave microstructure showed that the combined effect of creep and fatigue at 593°C and low loading frequency changed the fracture mode from quasi-cleavage to intergranular fracture. This change results in a significant increase in the fatigue crack growth rates. When the material was aged, however, the appearance of silicides in the α/β colonies altered the slip process and the crack tip mechanism becomes transgranular with lower crack growth rates. These results suggest that aging is an important factor on the creep-fatigue effects in near-α alloys. However, in duplex microstructure, such as IMI834, this relationship has never been established and the effect of aging is not fully understood. Moreover, Maier et al [28], in their study of the thermo-

mechanical fatigue behavior of IMI 834 with a bimodal microstructure of α grains and lamellar α/β colonies, have shown that at test temperatures above 600°C, dislocation slip changes from a planar slip mode within the primary alpha grains, to a more wavy type that leads to critical cracks in the lamellar α/β colony. These results suggest that temperature selection is also an important parameter in the damage process.

It is the purpose of the present investigation to explore the role of heat treatment on the microstructure and high temperature fatigue crack growth behavior of the near-α titanium alloy IMI 834 at a single temperature. The next chapter of this thesis reviews the role of alloying elements as well as the thermomechanical processing and mechanical properties of near-α alloys. Additionally, heat treatment and hardness tests performed on the material under study, IMI 834, to explore the effects on phase morphology and yield stress at room temperature are discussed. The effects of long-term exposures at 650°C on the thermal stability of IMI 834 are presented in the third chapter. Background is given in the significance of aluminide and silicide precipitations on the yield stress of near-α alloys during over-aging. Testing and analysis of over-aged IMI 834 conclude the chapter. In the fourth and final chapter the controlling crack tip mechanisms are examined in water-quenched IMI 834 with two different duplex microstructures as a function of the loading frequency through fatigue crack growth testing at 650°C. These tests will be achieved with loading conditions of 10Hz and 0.05Hz. The effect of a 300-second hold time imposed at peak stress level of the loading cycle will be also

addressed for the lower frequency; 0.05 Hz. Results of this study will be discussed and a generalized hypothesis of the crack tip mechanisms at elevated temperature in near-α duplex microstructures will be presented.

Chapter 2: Role of Heat Treatment in Titanium Alloys

Introduction:

This chapter describes the role of heat treatment on the morphology and associated mechanical properties of near-α Ti alloys. It is divided into three sections. The first section is a review on general aspects of physical metallurgy of near-α titanium alloys. Attention is given to the role of the α and β stabilizing elements as well as the thermomechanical processing on the mechanical property changes of near-α titanium alloys. The last two sections will detail experiments and analysis related to the effects of heat treatment on the microstructure and yield stress of IMI 834.

2.1 Review of Near-Alpha Titanium Alloys

As previously discussed, a wide range of titanium alloy microstructures may be attained through routes involving manipulation of alloying additions and thermomechanical processing [1]. In this section, a detailed description is given for the role of the aforementioned processes on the mechanical properties of near-alpha alloys.

2.1.1 Role of Alloying Elements

Typical alloying elements and corresponding phase diagrams for titanium are shown in Figure 2-1. This figure shows that the addition of alpha stabilizing elements, in particular nitrogen and oxygen, significantly raises the temperature of

the $\alpha \Leftrightarrow \alpha+\beta$ phase transformation. On the other hand, beta stabilizers, especially elements such as vanadium, niobium and molybdenum, lower the $\alpha+\beta \Leftrightarrow \beta$ phase transformation — also called β-transus.

Understanding the role of alpha and beta stabilizers is of primary interest as their additions significantly influence the mechanical properties of the alloy. Alpha alloys promote better mechanical properties at high temperatures and offer easier welding in complex components such as turbine blades [2]. On the other hand, β-alloys have higher formability especially in the form of foils. Figure 2-2 shows that α and near-α alloys have better high temperature strength and flow stress compared to α + β, near-β, and β-alloys [12]. However α + β, near-β, and β-alloys have better room-temperature strength and less strain rate sensitivity. In addition, α and near-α alloys have better welding ability, yet α + β, near-β, and β-alloys make forming and heat treatment easier.

Aluminum and molybdenum equivalent concentrations, respectively, are used to give the relative effect of alpha and beta stabilizers in titanium alloy. The two equivalencies are calculated using the following equations [7].

$$[Al]_{eq} = [Al] + [Sn]/3 + [Zr]/6 + 10 * ([O] + [C] + 2[N]) \qquad 2.1$$

$$[Mo]_{eq} = [Mo] + [Ta]/5 + [Nb]/3.6 + [W]/2.5 + [V]/1.5 + 1.25 * ([Cr] + [Ni]) + 1.7 * ([Mn] + [Co]) + 2.5[Fe] \qquad 2.2$$

Table 1-1 characterizes titanium alloys into three basic categories according to the Al and Mo equivalent concentrations: α and near-α alloys, α/β alloys, and β alloys [5, 7].

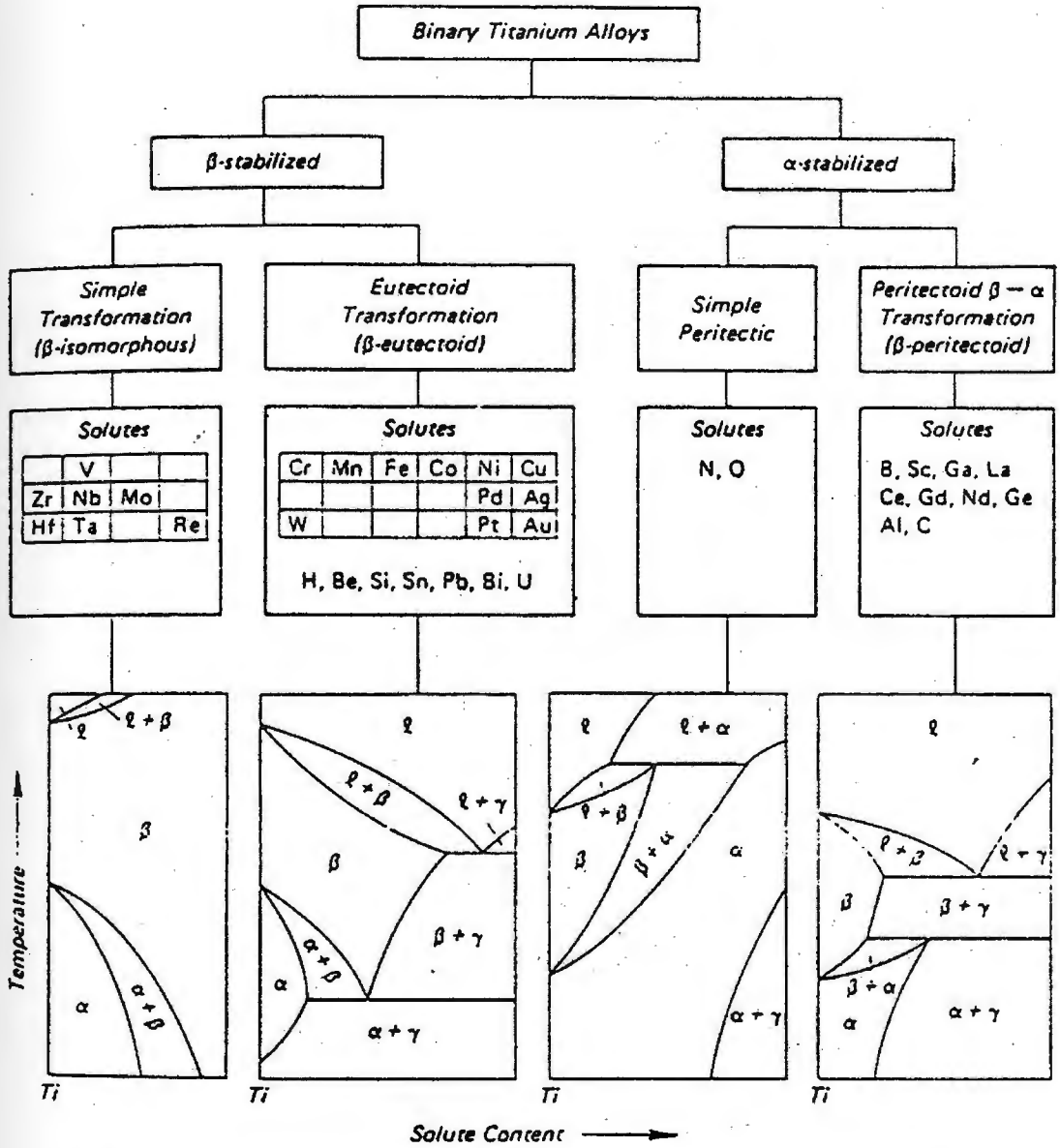

Figure 2-1: Classification scheme for binary alloys of titanium based on phase diagrams (from ref. [12]).

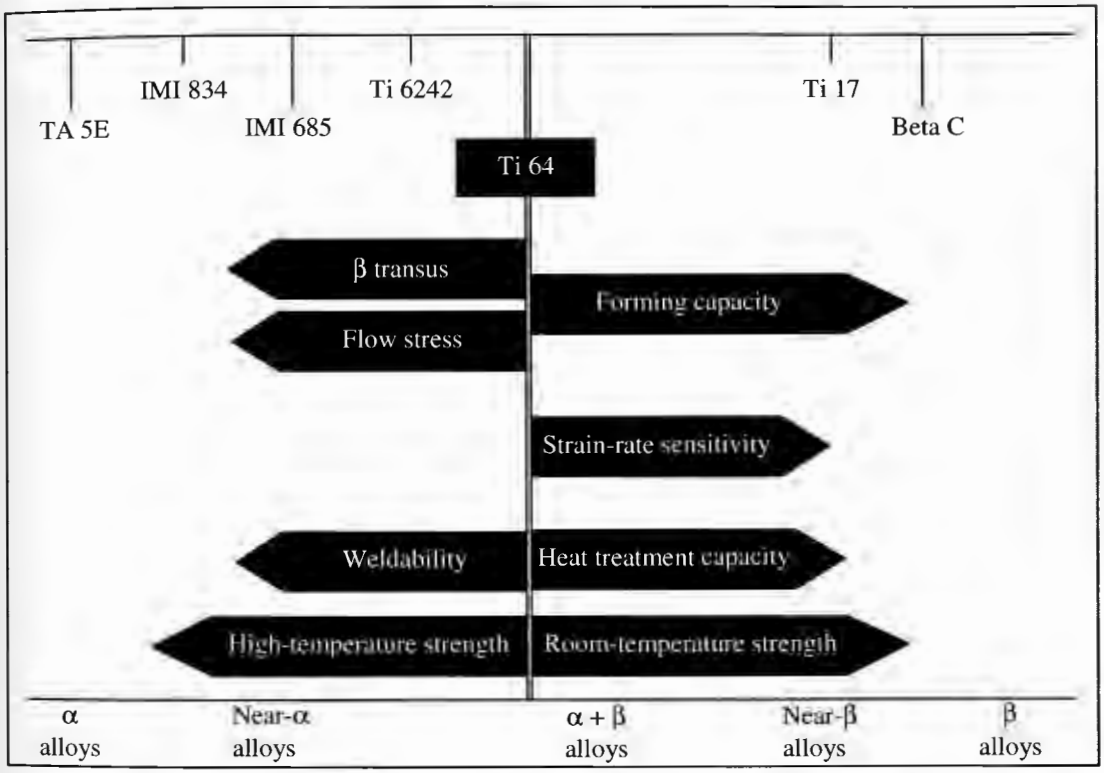

Figure 2-2: Main characteristics of the different titanium alloy families (from ref. [2]).

Ti-alloy	$[Al]_{eq}$	$[Mo]_{eq}$
α and near-α	5-8%	1-2%
α/β	3-6%	2-11%
β	1-4%	10-25%

Table 2-1: Characterization of Ti-alloys based on Al and Mo equivalent concentrations (from ref. [53]).

The role of each alloying element on the mechanical response of titanium alloys is described as follows [16]:

- **Aluminum (Al)** → The addition of aluminum, an α stabilizer, increases tensile and creep properties while reducing Ti-alloys density. Aluminum addition is however limited, as concentrations above 7% promote ordering as well as the formation of Ti_3Al (α_2) aluminides. This precipitate class is the subject of some interest, as at elevated temperatures, it often leads to severe post-exposure embrittlement due to decreased cross slip energy and sheared particles. A decrease in cross slip energy and sheared particles cause the slip to intensify and promote crack nucleation sites that lead to creep failure. Details on the effects of aluminides in titanium alloys are discussed in chapter 3.

- **Molybdenum (Mo)** → Molybdenum is the prime beta stabilizer in near-α alloys and is preferred for its substantial solid solution strengthening at high temperature and for its weight. Addition of this element markedly increases the heat treatment response of the alloy. It has been shown, however, that increases in molybdenum or niobium decrease the creep resistance. Alloys aimed at long-term creep strength, such as Ti-1100 and IMI 834, have lower molybdenum content. Otherwise, alloys aimed at high temperature strength, such as Ti-5524S, or superior strength at lower temperature, such as Ti-6242 and Ti-6246, have greater molybdenum percentages. Moreover, the addition of molybdenum makes the alloy more difficult to weld.

- **Niobium (Nb)** → Niobium is a beta stabilizer and is added primarily to improve surface stability resistance (oxidation resistance) during high-temperature exposure.
- **Silicon (Si)** → Silicon promotes the creep resistance of Ti alloys. Silicon provides a solid solute environment to dislocations and therefore prevents the formation of voids that lead to creep failure. Its role is fundamental at elevated temperature and further details will be given on this alloying element in the following sections. More recently developed alloys, such as IMI 834 and Ti-1100, use higher silicon contents (~0.5%). Beyond these levels, post-creep ductility (stability) is compromised with no further creep enhancement as shown in figure 2-3. The maximum effective concentration of silicon in high-temperature alloys is governed by its tendency to form zirconium silicides, which will be detailed in chapter 3.
- **Carbon (C), Tin (Sn) and Zirconium (Zr)** → Carbon, tin and zirconium are neutral as α or β stabilizers concern, but they are used to strengthen the alloy and to provide thermal stability of the phases.

2.1.2 Example of Near-α Alloys and their Mechanical Properties

Tables 2-2 and 2-3 list three different near-α titanium alloys with their corresponding element additions and mechanical properties, respectively. These tables show that small changes in the concentrations of α and β stabilizing elements change considerably the mechanical properties of the alloys. For this reason, detailed studies are performed to characterize each alloy over a broad spectrum of

temperatures and loading conditions. One method used to help analyze titanium alloys is the aluminum and molybdenum equivalence.

Figure 2-4 is a plot of the aluminum and molybdenum equivalent concentrations for different titanium alloys. The comparison between IMI 834 and Ti-1100, for example, shows that the aluminum and molybdenum equivalences are almost identical. Although they have different chemical compositions, as seen in Table 2-2, their room temperature mechanical properties shown in table 2-3 are closely related, with identical E and YTS and with a small difference in UTS. When comparing IMI 834 and IMI 685, figure 2-4 shows that the two alloys have similar molybdenum equivalencies, but different aluminum equivalencies. The drop in aluminum equivalence seen in IMI 685 is reflected in a drop in the YTS when compared with that of IMI 834. In addition, similar values for molybdenum equivalencies in the two alloys accounts for the small change in their E values. Differences in elongation as seen in Table 2-3 could be the result of aluminum and molybdenum equivalence in addition to variations in their material microstructure. Ti-1100, for example, is a near-α alloy with a Widmanstätten microstructure, which is less ductile than the duplex microstructure of the other two alloys.

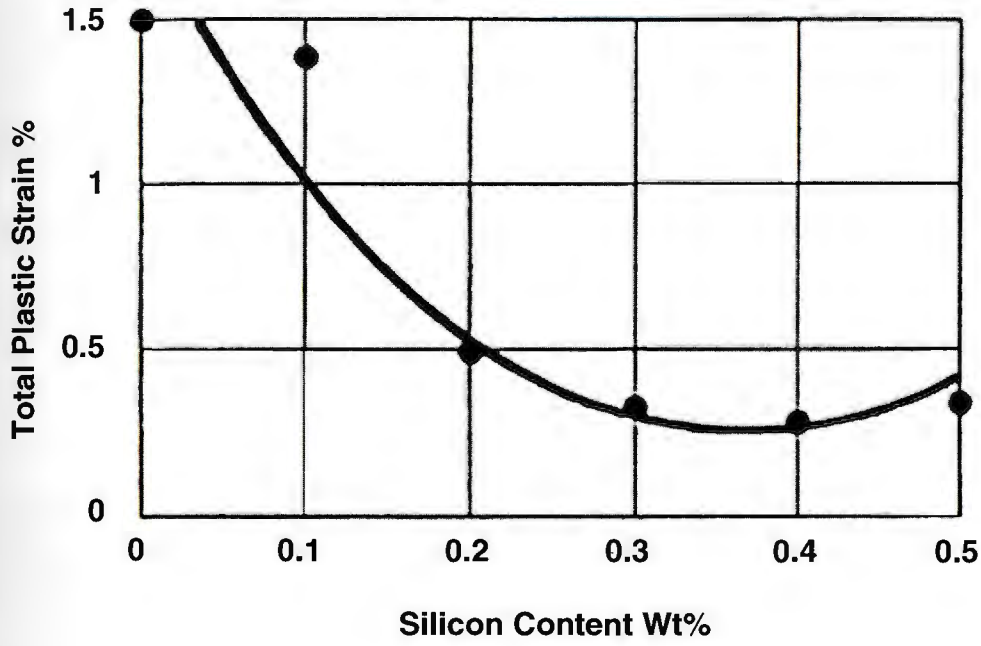

Figure.2-3: Effect of silicon content on the creep behavior of IMI 834 alloy (from ref. [11]).

Name	Al	Sn	Zr	Mo	Nb	Si	Fe	O	C
IMI 685	6.0	--	5.0	.5	--	.25	.02-.03	.15	--
Ti-1100	6.0	2.7	4.0	0.40	--	.45	.017	.07	.022
IMI 834	5.8	4.0	3.5	.5	.7	.35	.02-.03	.1	.06

Table 2-2: Composition of selected near-alpha titanium alloys (from ref. [16]).

Mechanical Properties	Modulus of Elasticity (E)	Yield Tensile Strength (YTS)	Ultimate Tensile Strength (UTS)	% Elongation (ductility)
IMI 685	125 GPa	$\geq$ 880 MPa	$\geq$ 950 MPa	10%
Ti-1100	120 GPa	910 MPa	1000 MPa	8%
IMI 834	120 GPa	$\geq$ 910 MPa	$\geq$ 1030 MPa	12%

Table 2-3: Mechanical properties at room temperature of selected near-alpha titanium alloys (from ref. [16]).

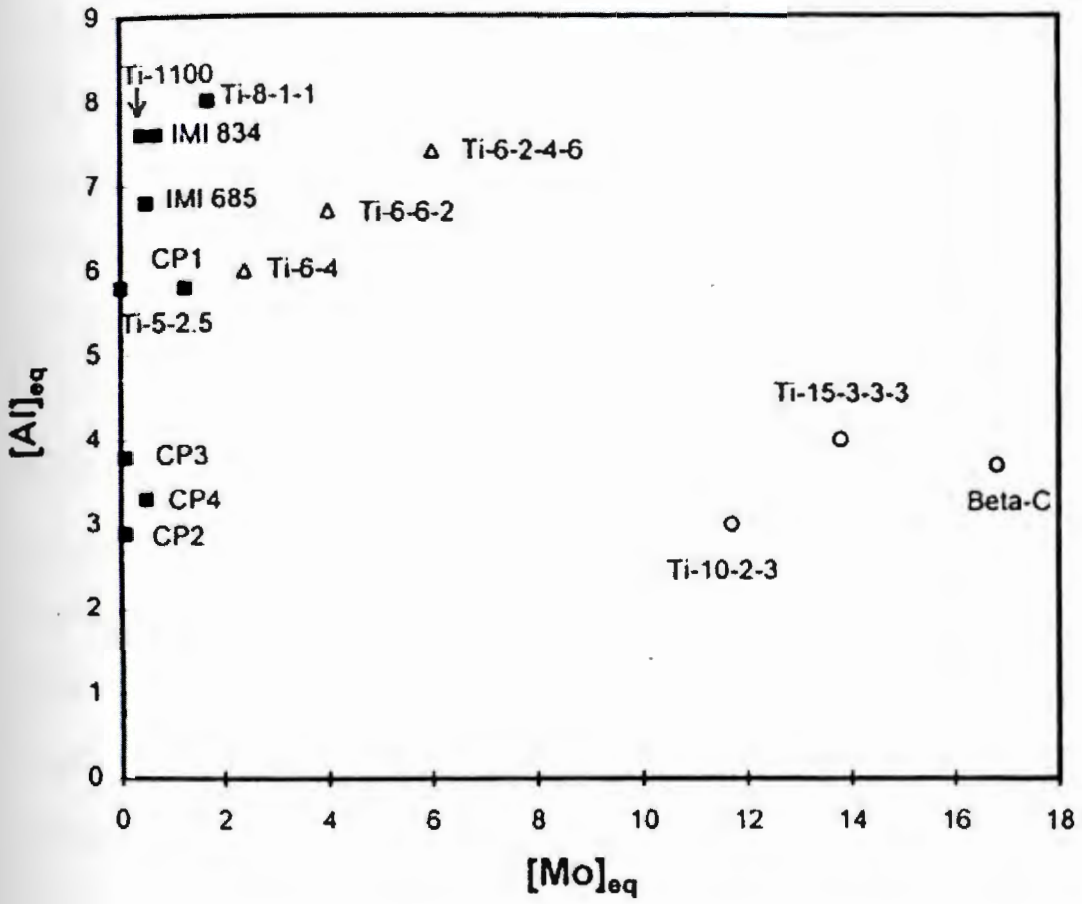

Figure.2-4: Aluminum and molybdenum equivalencies for Titanium Alloys (from ref. [32])

Although aluminum and molybdenum equivalences are useful tools in analyzing titanium alloys, other factors must also be considered. Creep deformation, which is a measure of evolving strain as a function of stress, time and temperature, is often analyzed by methods such as the Larson-Miller parameter [17]. Data in figure 2-5 shows how the yield stress of Ti-6242, IMI 834 and Ti-1100 decreases with time and temperature [18]. The importance of silicon addition to the material is also evident in the figure, where increasing silicon concentrations of 0.1, 0.35 and 0.45, for Ti 6242, IMI 834, and Ti 1100, respectively, shows an increase in creep resistance as a function of time and temperature. The figure also shows that for high temperature applications, there is a limit to the amount of silicon that can be added before creep resistance decreases. The presence of a limit is due to the tendency of the alloy to form Zirconium Silicides, $(Ti,Zr)_5Si_3 - S_1$ and/or $(Ti,Zr)_6Si_3 - S_2$, on the α platelets of the transformed β-phase as well as on the martensite boundary between α/β colonies and α_p. On studies done by Sridhar and Sarma it is shown that the size of silicides increases with aging temperature [19]. The formation of silicides removes silicon from the solid solution thus leading to reduction in ultimate tensile strength (UTS), ductility and creep resistance of the alloy as shown in figures 2-3 and 2-5. The role of silicides in near-α alloys will be presented in detail in chapter 3.

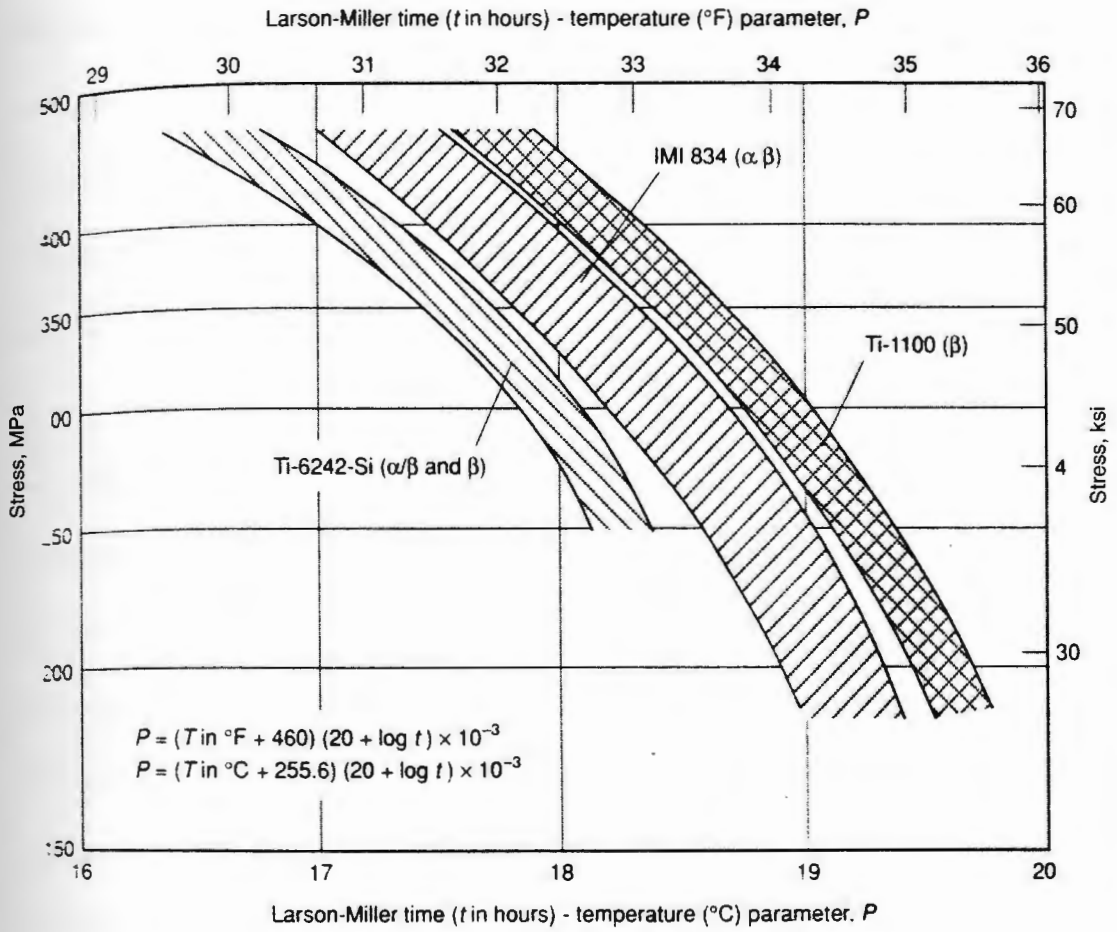

Figure.2-5: Creep properties in Ti6242 alloy, IMI-834 alloy and Ti-1100 alloy with α/β and β processing as indicated (from ref. [8]).

2.1.3 Processing and Heat Treatment of Duplex Microstructures

The processing and heat-treatment of near-alpha titanium alloys leads to two distinct microstructures: Widmanstätten microstructures, made of lamellar colonies embedded within large β grains; and duplex microstructures, composed of fine equiaxed particles of alpha phase, called primary alpha (α_p), and α/β colonies, containing α lamella or needles in retained beta phase. Figure 2-6 is an SEM image showing the duplex microstructure of IMI 834 with 23% α_p volume fraction. Figure 2-6 also shows that colonies and α_p particles have approximately the same size ($\approx$ 40 μm).

Typical processing of duplex alloys consists of four steps as shown schematically in figure 2-7. The first step is comprised of a solution heat treatment or homogenization in the β-phase field. In this step, the alloy temperature is raised above its β-transus to be homogenized. The rate at which the material is cooled following solution treatment dictates the size of the primary alpha particles, making this an important treatment step [13]. Hot working in the α+β phase field, or deformation process, is the second step in processing and it introduces dislocations in the alloy, so that α and β can be recrystalized later. The third processing step consists of recrystalization of the material in the α+β phase field. Recrystalization in this field has a significant effect on the alloy mechanical properties. The recrystalization temperature, indicated by T_s in figure 2-7, determines the volume fraction of the primary alpha, which forms as equiaxed grains at the "triple points" of the recrystalized β-grains. The cooling rate at the end of the recrystalization

process determines the width of the individual lamellae or needles formed within the α/β colonies [13].

Depending on the cooling rate following recrystalization, more or less nucleation and growth of α-crystals occurs as β-phase material passes through the α/β phase field [48]. As the alloy cools down, alpha phase nucleates at sites on the prior beta grain boundaries and grows as parallel platelets or as needles towards the interior of the prior beta grain. Needle or platelet formation becomes more coarse with decreasing cooling rates as the driving force for nucleation within the grain is reduced. Platelets tend to grow in an aligned manner, with all platelets having the same crystallographic orientation. Needles grow in several intertwining orientations forming the so-called "basket weave" morphology. Needle formation is mostly found with high cooling rates (greater than 10^{o}C/min).

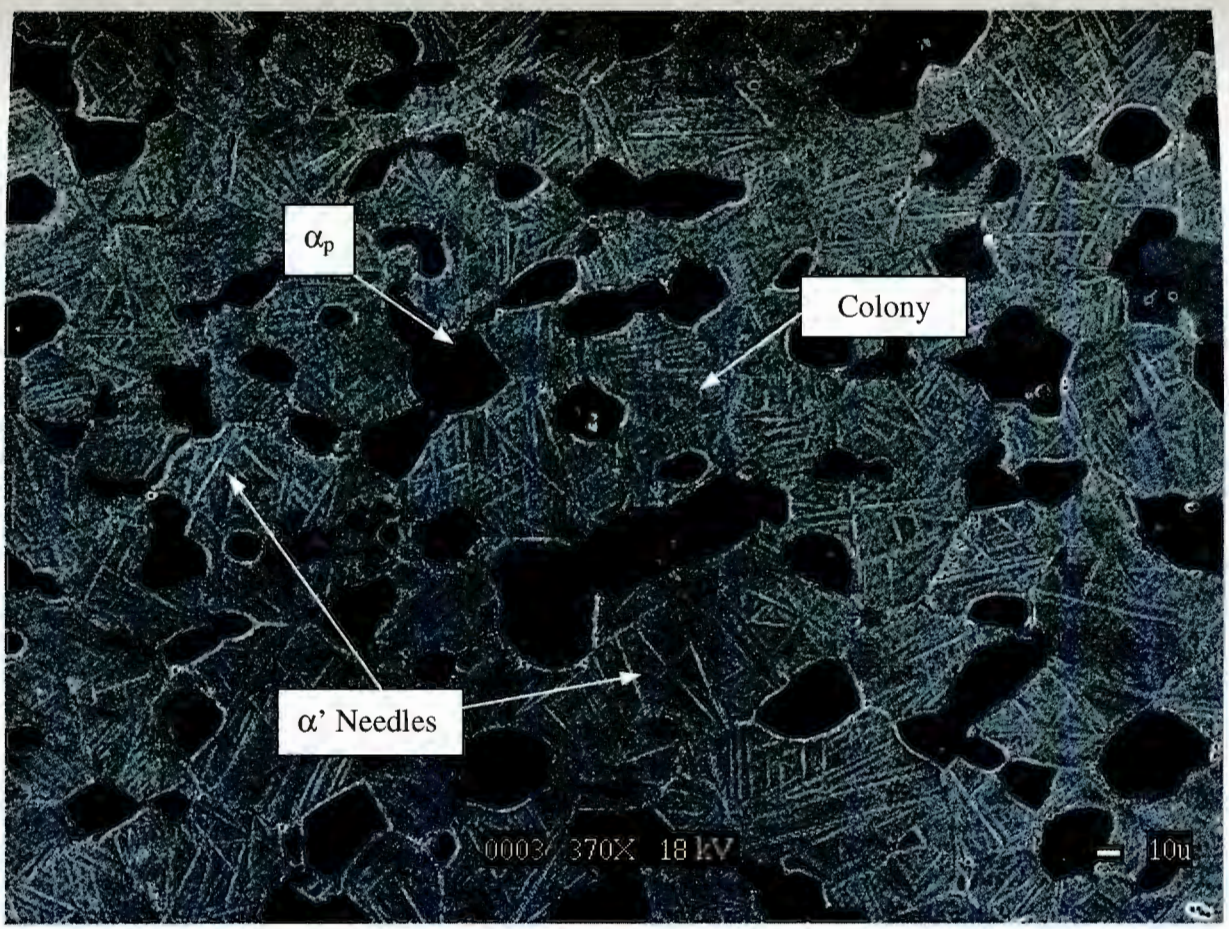

Figure 2-6: Microstructure of IMI 834 (heat-treated and aged to 23% α_p volume fraction).

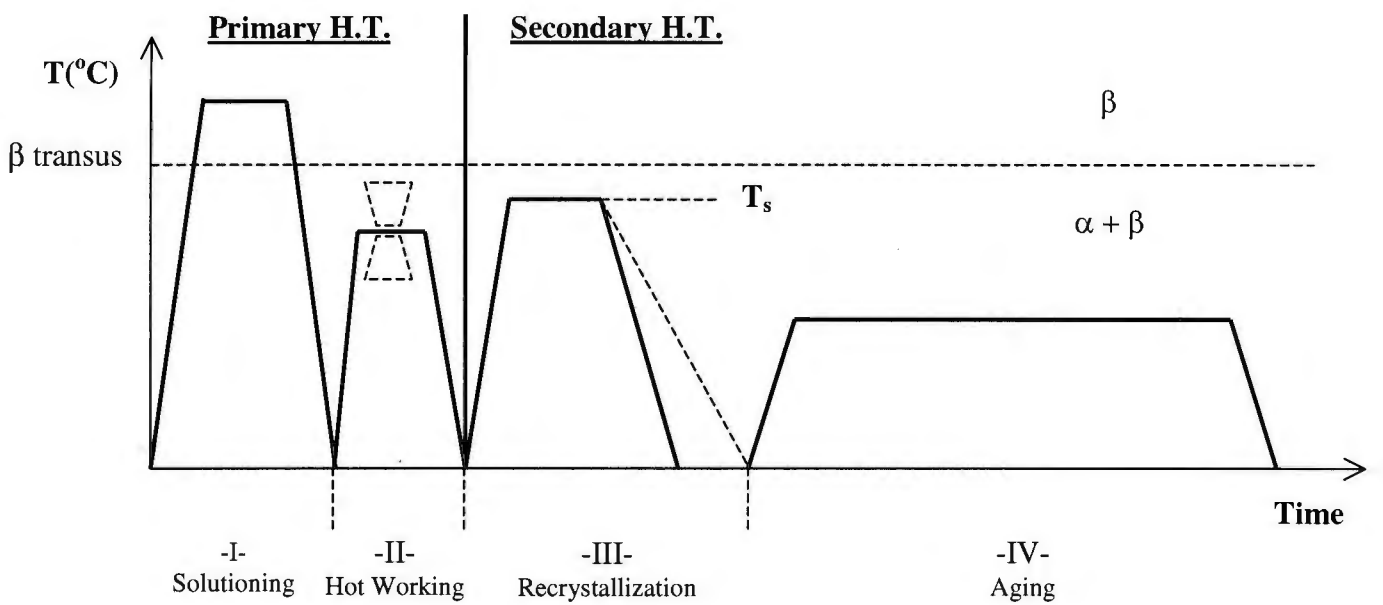

Figure 2-7: Thermal cycle applied in duplex microstructures (β transus in IMI 834 occurs at approximately 1060°C [21]).

Two models are generally proposed for the formation of primary alpha, or globularization, as shown schematically in figures 2-8 and 2-9. Initially, recrystalized alpha grains are formed within the alpha platelets, shown in figure 2-8.b [13, 51, 52]. However, due to surface tension, a driving force is provided for the movement of some β phase into the α/β boundaries and for the simultaneous rotation of the α/β boundaries towards each other, as seen in figure 2-8.c. The rotation enlarges the recrystalized α-grain to a size larger than the original platelet thickness, bringing it into contact with the adjacent unrecrystalized α-platelet, shown in figure 2-8.d. Similarly, at grain boundaries, the mechanism is based on recrystalization of α within the grain boundary layer and the surface-tension-driven redistribution of the β-phase, accompanied by pressure from the recrystalized α-grains and alpha side platelets, as seen in figure 2-9.

During the recrystalization phase, α and β stabilizers partition into the corresponding material phases. The alloy elements that are strong α-stabilizers, such as aluminum and oxygen, or strong β-stabilizers, such as molybdenum and vanadium, partition into the α and β phases, respectively. This alloy partitioning effect also causes the α-lamellae, or α', to have a lower concentration of α stabilizing elements compared to α_p [13]. This process is detailed later.

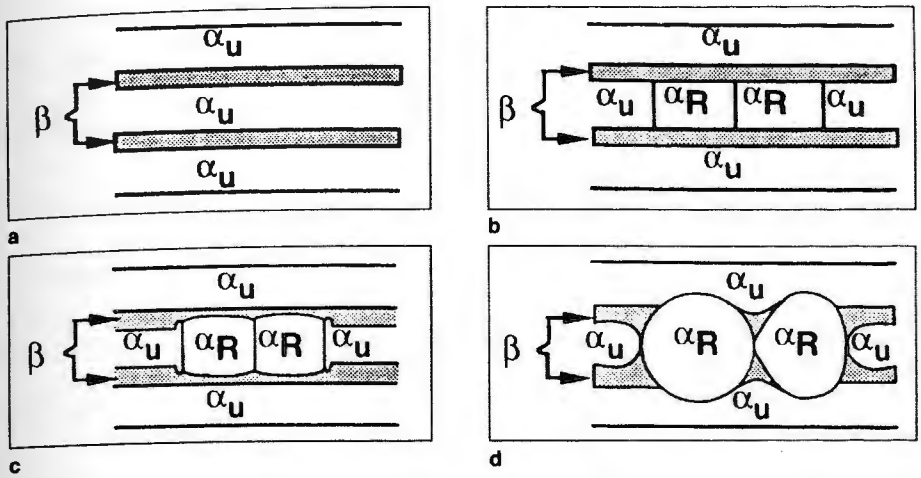

Figure 2-8: Schematic of the mechanism of globularization from lamellar microstructures: (a) unrecrystalized, (b) beginning of recrystalization, (c) α_R moving into a side plates, (d) α_R consuming into a side plates (from ref. [51]).

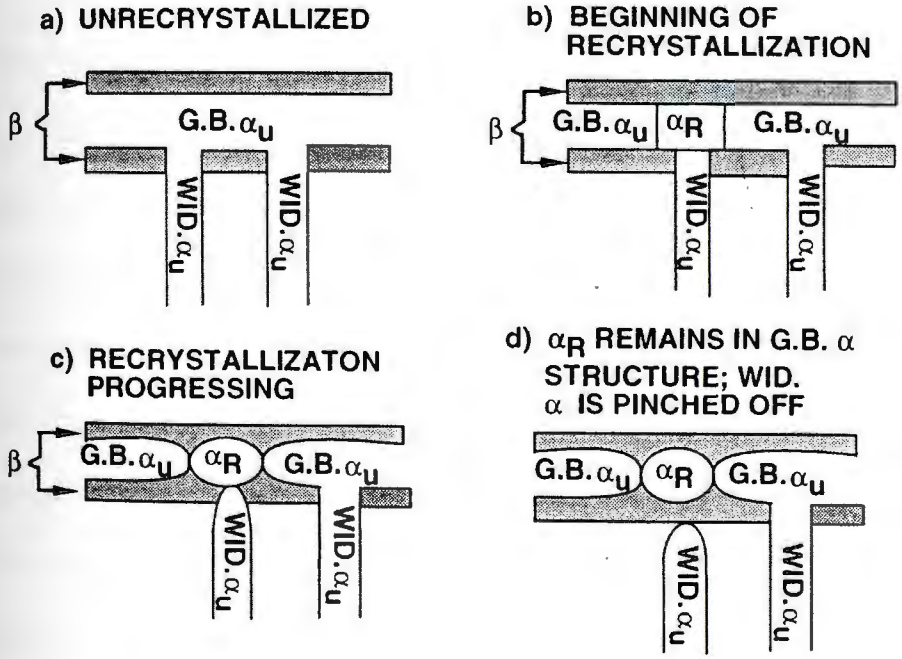

Figure 2-9: Schematic of the mechanism of globularization at grain boundary (from ref. [52]).

The final processing step is an aging treatment. Aging is used to precipitate Ti_3Al particles for strengthening and thermal stability of the alpha phase. Depending on the titanium alloy, different aging time and temperature are recommended. For example, IMI 834 is aged for 2-hours at 700°C. At temperatures above 750°C, Ti_3Al starts dissolving [9]. In addition to Ti_3Al, the aging phase also precipitates silicides. S_1 and S_2 type silicide precipitates usually form at temperatures below approximately 600°C, with small temperature variations depending on the chemical composition of the alloys. Aging above 600°C, such as aging of IMI 834, forms only S_2 type silicide precipitates [20].

2.1.4 Effects of Heat Treatment on Mechanical Properties

Important parameters in each of the aforementioned processing steps are related to material microstructural features and mechanical properties in figure 2-10 [13]. This figure shows that the cooling rate is the most important parameter in the solution heat treatment phase, step I. Microstructural features such as texture type and texture symmetry are attained during the hot working phase, or step II. Step III shows that changes in the recrystalization temperature, as well as recrystalization time and cooling rate cause significant changes in the material mechanical properties. Finally, figure 2-10 shows that in step IV the aging temperature influences the Ti_3Al content, as well as the formation of α' in the α/β colony. Based on this figure, manipulation of the processing in steps III and IV causes important changes in the mechanical properties of the material. For this reason, these steps are analyzed in detail throughout this thesis.

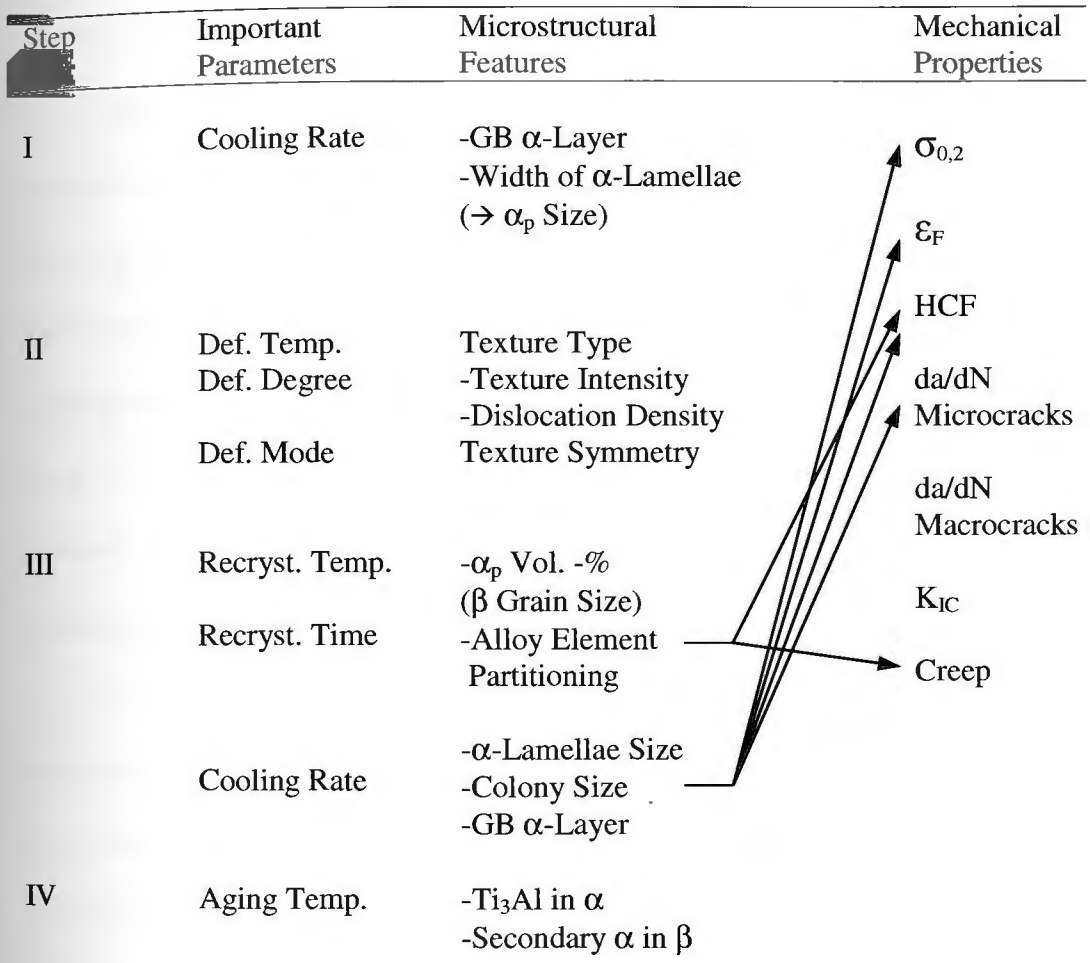

Figure 2-10: Important processing parameters, resulting microstructural features, and major influences on mechanical properties (arrows) for duplex microstructures (from ref. [13]).

In the study by Lütjering [13], it is suggested that one of the influential microstructural features on the mechanical properties of duplex microstructures is the effective slip length controlled by the size of the α/β colony. The colony size, on the other hand, is dependent on the recrystalization time and cooling rate, as shown in Fig. 2-10.

Figure 2-11 shows the effect of cooling on the plastic strain of the near-α titanium alloy IMI 834. The figure shows that cooling rate has similar effects on the creep resistance of the alloy, independently of the microstructures. Creep strain decreases as cooling rate increases from 10°C to 30°C per minute, and increases as cooling rates increase thereafter. Duplex microstructures show evidence of lower creep resistance compared to the fully lamellar microstructure. In addition, increase in α_p volume fraction shows decreased creep resistance in duplex microstructures.

Plastic deformation of HCP alpha-titanium occurs by both slip and twinning processes; however, slip appears to be the dominant deformation mode [3]. Figure 2-12 shows the influence of slip length on material mechanical properties such as yield stress, high cycle fatigue (HCF) strength, low cycle fatigue (LCF) strength, as well as micro and macro fatigue crack propagation. According to Lütjering [13], slip length is dependent on the α/β colony size rather than the individual α-lamellae or needle length. This dependence makes the smaller α/β colonies in near-α alloys better fatigue resistant materials, especially alloys that undergo higher cooling rates in the recrystalization step.

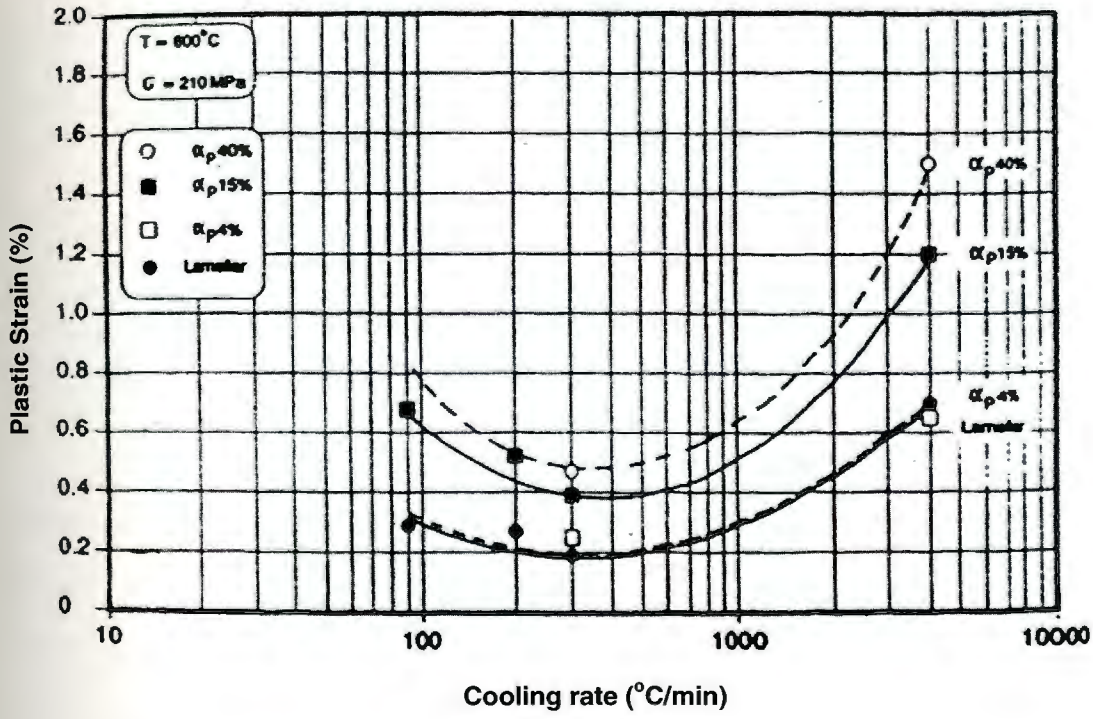

Figure 2-11: Effect of cooling rate on creep strain of near-α titanium alloy IMI 834 (from ref. [13])

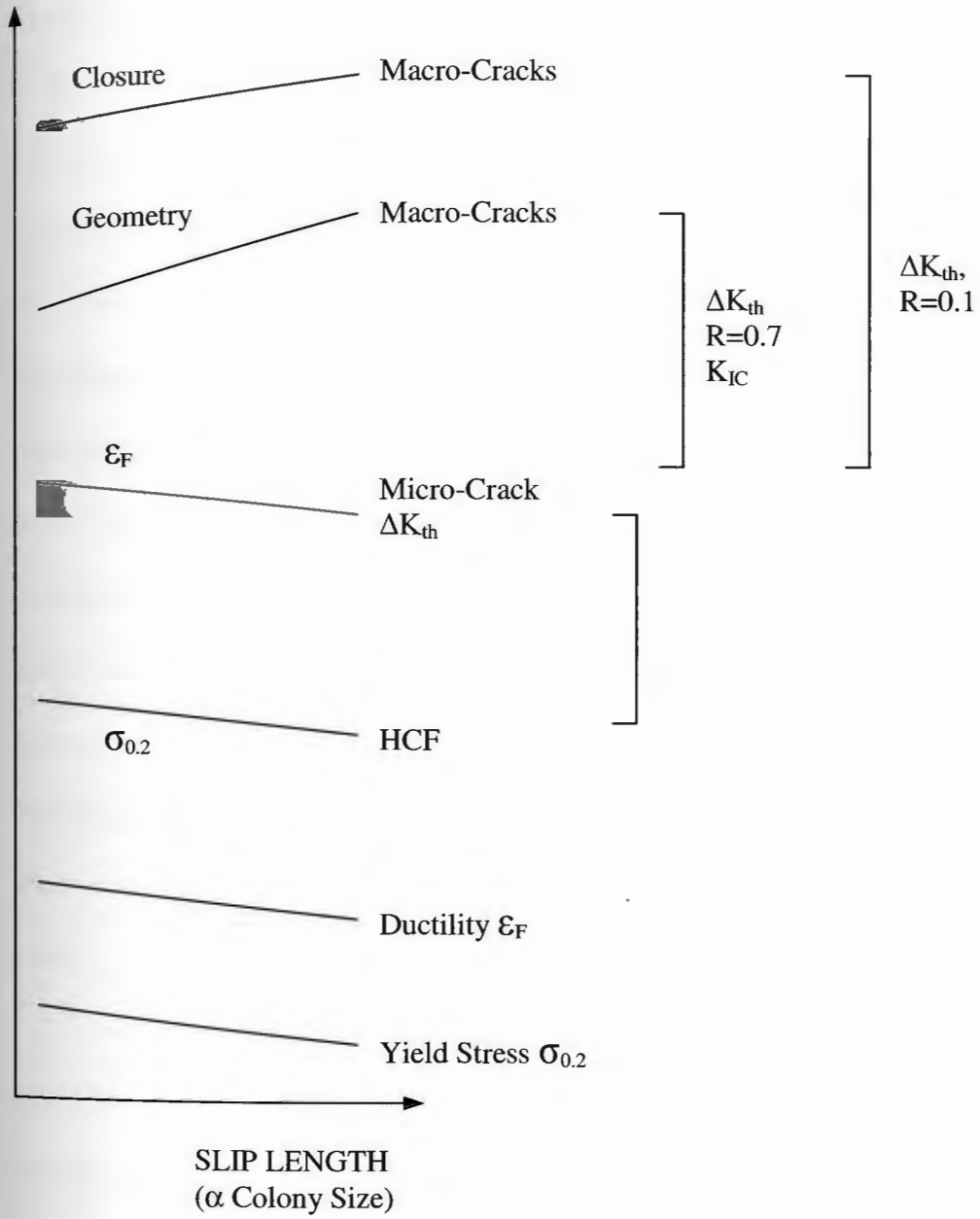

Figure 2-12: Influence of slip length (α colony size) on mechanical properties (schematically) (from ref. [13]).

Another microstructural feature that is influential in the mechanical properties of duplex titanium alloys is the alloy element partitioning effect [13]. Zhang et al have reported element partitioning in the Ti-6-22-22 alloy, particularly of the α-stabilizer Al and the β-stabilizer Mo [40]. In addition, the concentration of Al in α' is lower than that in the α_p but about twice as high as those in the β-phase, see table 2-4. Baxter et al [36] found that the aluminum equivalency in the primary and secondary alpha is influenced by the α-stabilizing interstitial elements, carbon and oxygen. Sn and Zr have extensive solid solubility in both α and β phases and partition to both phases occurs at similar degrees. Element partitioning in alpha favors slower cooling rates [38] and higher α_p volume fractions [13]. Increases in α_p volume fraction cause α-stabilizer elements in the α/β colony to lessen, which results in a much lower basic strength region as compared with α_p. This alloy partitioning effect has a negligible influence on ductility and on the growth of short and long term cracks, including the fracture toughness. However, the partitioning effect shows dependence between α_p volume fraction and yield stress as well as creep.

Table 2-5 shows how some mechanical properties of IMI 834 change with α_p volume fraction and microstructure. This data suggests that for small volume fractions of α_p, the α/β colony size effect dominates, whereas for large volume fractions of α_p, the alloy element partitioning effect dominates. Lütjering [13] states that the dependence of yield stress on α_p volume fraction shows usually a maximum between 10 and 20% α_p. For the duplex material, he adds, the small

decline in yield stress in the high α_p volume fraction tested at 600°C indicates that the alloy partitioning effect is less pronounced at high temperatures.

Phase	Al	Cr	Mo	Sn	Zr	Si
β	2.82	8.84.	14.51	3.33	2.27	0.26
α	8.45	0.40	0.56	2.39	2.08	0.15
α'	7.33	0.91	1.13	2.83	2.30	0.20

Table 2-4: Element partitioning on Ti-6-22-22 following solution treatment at 1000°C for 1-hour, heat treatment at 925°C for 1 hour, and aging at 540°C for 8-hours (from reference [40]).

Microstructure	Test Temp.	$\sigma_{0,2}$ (MPa)	UTS (MPa)	σ_F (MPa)	El (%)	RA (%)
Lamellar	RT	925	1015	1145	5.2	12
Duplex (20% αp)	RT	995	1100	1350	12.9	20
Duplex (30% αp)	RT	955	1060	1365	12.6	26
Lamellar	600°C	515	640	800	10.5	26
Duplex (20% αp)	600°C	570	695	885	9.9	30
Duplex (30% αp)	600°C	565	670	910	14.4	36

Table 2-5: Tensile properties at RT and 600°C in IMI 834 (from ref. [13]).

2.2 Material of the Study

The material selected for this study is the near-α titanium alloy IMI 834, with a nominal composition Ti-5.8Al-4.0Sn-3.5Zr-0.7Nb-0.5Mo-0.35Si-0.06C. The aluminum and molybdenum equivalences for this alloy are 7.49 and 0.56, respectively. Although near-α titanium alloys offer a wide range of microstructures through thermo-mechanical treatments, IMI 834 is usually processed in the α/β field, which results in a duplex microstructure. In this study, IMI 834 is heat-treated and aged following the steps III and IV previously discussed (see figure 2.7). A micrograph of the material with 23% α_p volume fraction after recrystalization and aging treatments was shown previously in figure 2-6. The experimental procedure used to determine the effect of heat treatment on the phase morphology of this alloy, as well as the heat treatment results and analysis will be presented.

2.2.1 Effect of Heat Treatment on Phases Morphology

The effect of heat treatment on the phase morphology of IMI 834 is addressed in this section. As shown before, primary alpha volume fraction and α/β colony size are major factors in changes of the mechanical properties of titanium alloys. Therefore, a series of experiments have been performed to determine the relationships between the heat treatment and the volume fraction of α_p as well as the size of α/β colonies in IMI 834. Analyses of these tests are detailed in the following sections.

2.2.1.1 Experimental Procedure

The material of study, Titanium alloy IMI 834, was supplied by TIMET in the form of 2.5-in.-diameter / 0.5-in.- thick forged pancakes; as shown in figure 2-13. As-received IMI 834 pancakes were cut into quarters using a water-jet machine and subsequently cut into ½ -inch cube specimens using a diamond precision saw. To obtain different α_p volume fractions in the desired duplex microstructure, the specimens were recrystalized at temperatures ranging from 920°C to 1055°C for two hours and aged at 700°C for 2-hours. All heat treatments were performed in an air-furnace. Four thermocouples were placed inside the furnace at different locations before and during heat treatments. Temperature changes showed less than a 3°C error. Prior to inserting the test specimens, stabilization of the furnace at the required treatment temperature was carried out for a minimum of one hour. Heat treatment time started following stabilization of temperature after placing specimens in furnace, usually not taking more than two minutes. Cooling was done by air or by water quenching. After the aging treatment, a surface layer of 1 mm was removed from all specimens using a diamond precision saw. Mechanical polishing using 400, 600, 800, and 1200 grid water sand paper followed by 5, 3 and 1 micron diamond solution was performed after surface layer removal. The test specimens were then etched by immersion in Kroll's reagent for periods ranging between 10 and 35 seconds. SEM and optical microscopy examinations were performed afterward. Alpha primary volume fraction was measured from SEM images with 370X resolution to better capture the overall content of the phase.

Sigma Scan Pro image analysis software was used to calculate the α_p percentage. The error in measuring the volume fraction using this method was less than 2%. Twenty-five colony size measurements were taken from each specimen using the linear-intercept method for two-phased microstructures described in reference [22]. Results of these observations are given in the following section.

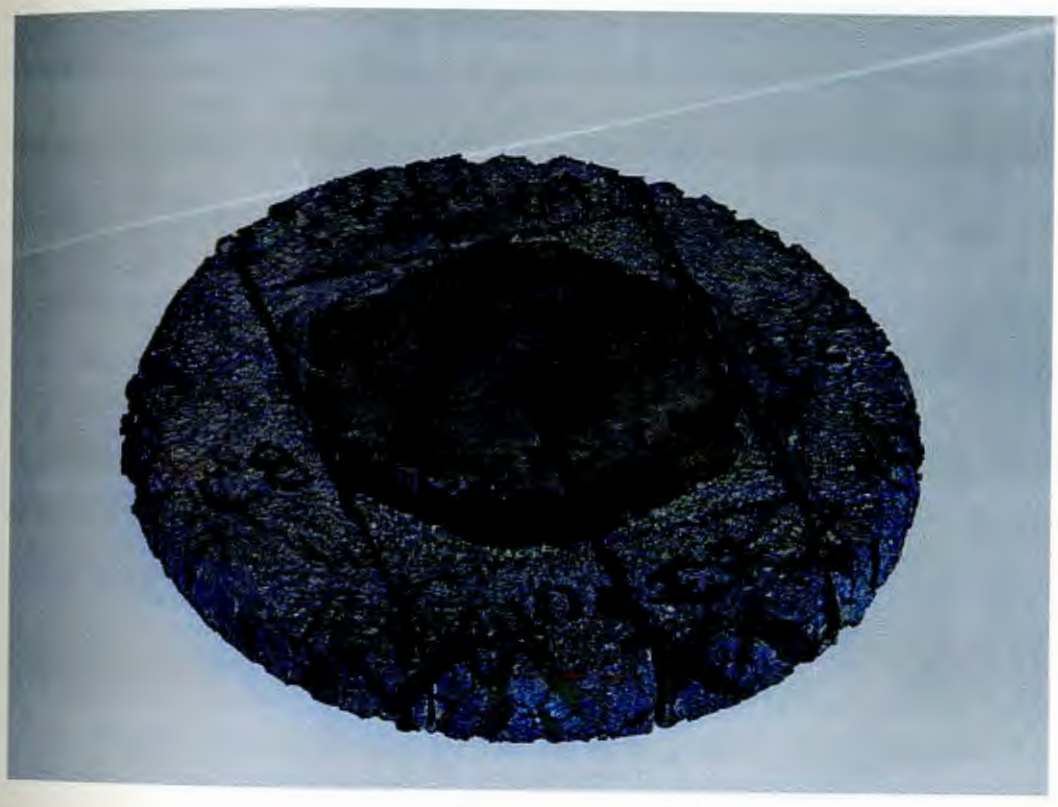

Figure 2-13: IMI 834 pancake with water jet cuts.

2.2.1.2 Results and Analysis

The microstructure of specimens that were water-quenched and air-cooled after the recrystalization step as well as aged at 700°C for 2-hours are shown in Fig. 2-14 and 2-15, respectively.

Figure 2-16 represents the effect of aging on α_p volume fraction for air-cooled specimens that have been subjected to recrystalization temperatures between 1000°C and 1045°C. This figure compares air-cooled specimens before and after the two-hour aging. It shows that the α_p volume fraction for the aged and unaged materials at 1000°C is approximately 45% and 28%, respectively. The figure also shows that for volume fractions above 15%, aging resulted in an additional increase in α_p volume fraction. Below 15% α_p, however, volume fractions are not affected by aging. This outcome may be the result of element partitioning effects. As the volume fraction of α_p increases, more aluminum is available in the particle to form the Ti_3Al precipitate. When the material is aged, the increase in volume fraction is a result of α_2 growth in the primary alpha sites.

Figure 2-17 represents the effect of cooling rate on α_p volume fraction. This figure shows that maximum α_p volume fraction is reached at higher recrystalization temperatures for the water-quenched microstructure compared to that of the air-cooled microstructure. Maximum water-quenched α_p volume fraction, 40%, is obtained at recrystalization temperatures lower than 1000°C, whereas the maximum air-cooled α_p volume fraction, 54%, is obtained at recrystalization temperatures lower than 970°C. Figure 2-17 also shows that below

a critical volume fraction, referred to as CVF, corresponding to 35%, the cooling rate has little effect on the growth of α_p. It can be assumed that α phase growth also occurs in the α/β colony, but no quantitative measurements have been performed in this thesis to corroborate this assumption. At α_p volume fractions below 15%, the curves of the two cooling rates are slightly different. One reason for this difference may be that in the higher cooling rate material, α phase in the primary alpha sites is not allowed to diffuse into the colonies. The fact that the two curves show a region, where, for the same temperatures, nearly identical α_p volume fractions are attained, indicates a region of stability. In this region, cooling rate does not show an effect on the final α_p volume fraction. By inspection, the β-transus of the material tested appears to be around 1055°C/1060°C, which agrees with reports by Singh et al [29], 1060°C, and Es-Souni [37], 1055°C.

Colony size measurements of water-quenched (WQ) specimens from this test as well as oil-quenched (OQ) and air-cooled (AC) from selected references are plotted in figure 2-18. Data from this study shows that a sharp decline in α/β colony size, from 0.17 mm to 0.03 mm, occurs between 3% and 23% α_p volume fractions, respectively. A study by Dowson et al [32] on oil-quenched (OQ) IMI 834 shows a similar decline on specimens with 5%, 15% and 25% α_p volume fractions. Colony size values given by Es-Souni [37] and by Kordisch et al [30] for the air-cooled (AC) IMI 834 with 17% and 20% α_p volume fraction, respectively, lay on the same curve as the WQ specimens. Between 23% and 39% α_p vf, results from the current study suggest that the α/β colony size remains stable at 0.03 mm.

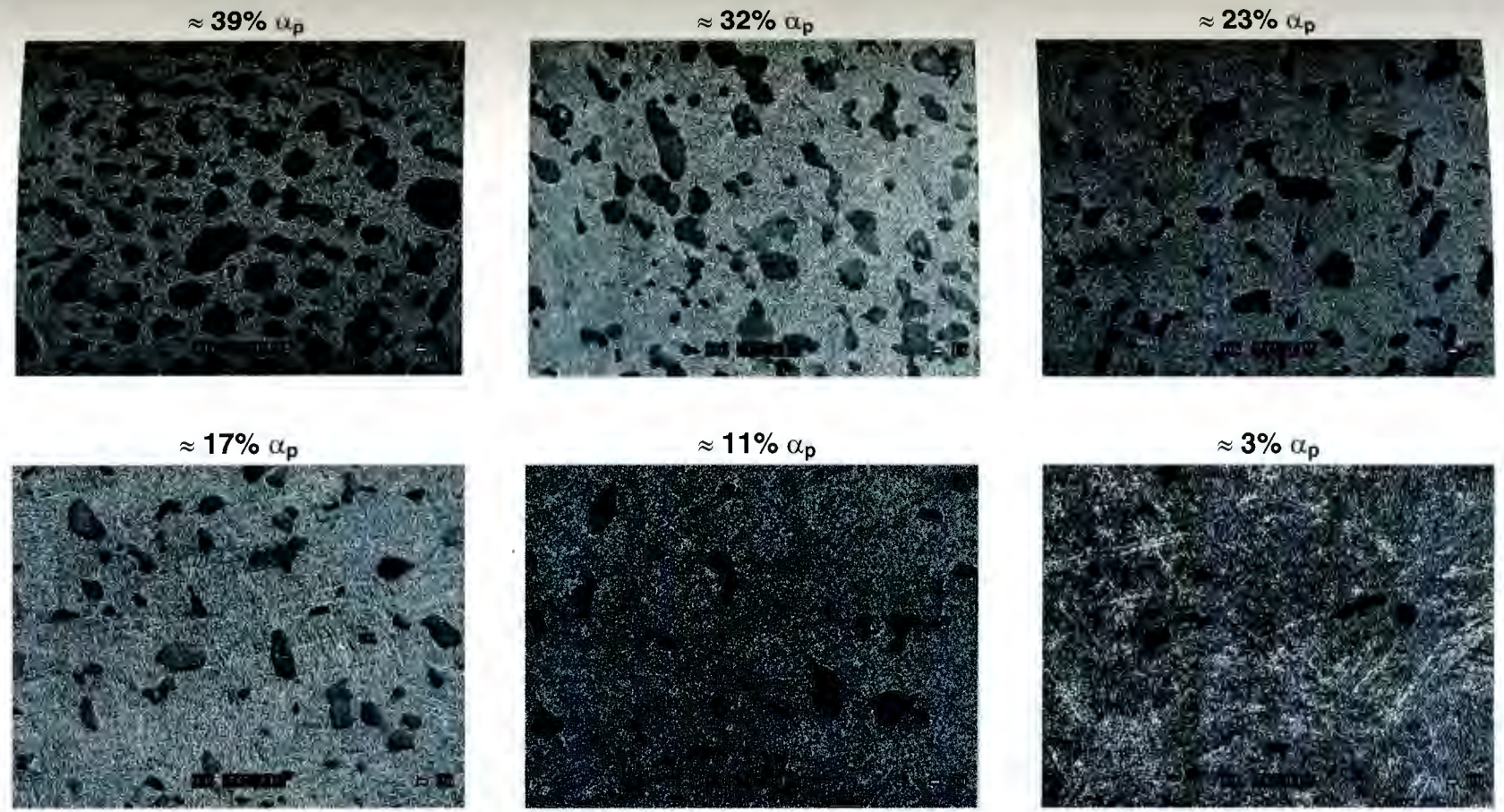

Figure 2-14: Water-quenched IMI 834 microstructures.

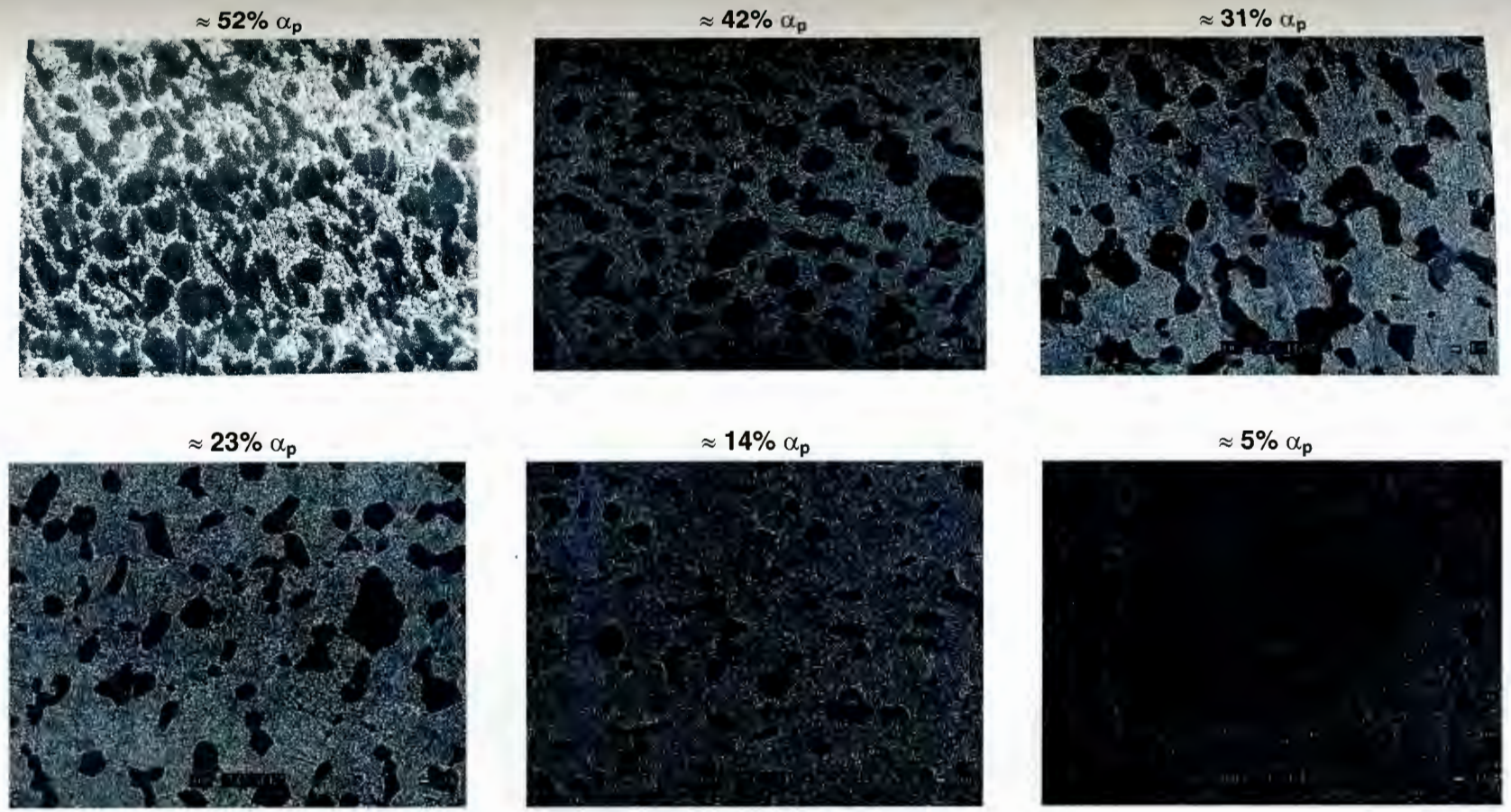

Figure 2-15: Air-cooled IMI 834 microstructures.

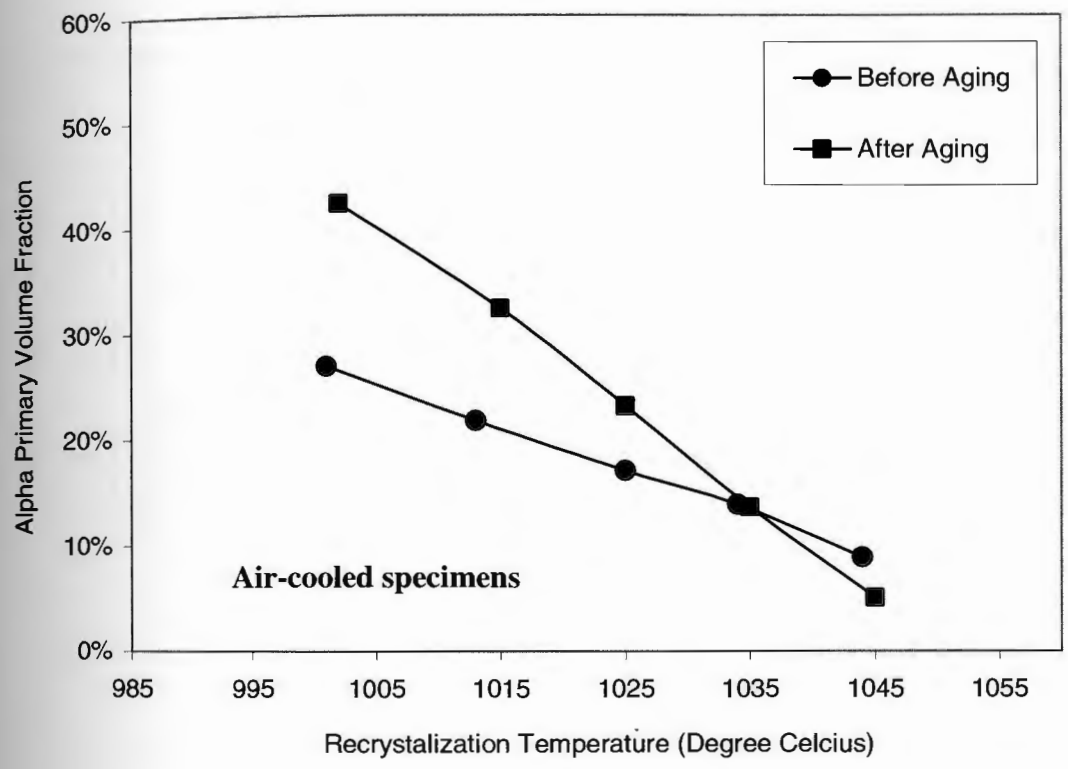

Figure 2-16: Effects of aging on the α_p volume fraction for air-cooled specimens of IMI 834.

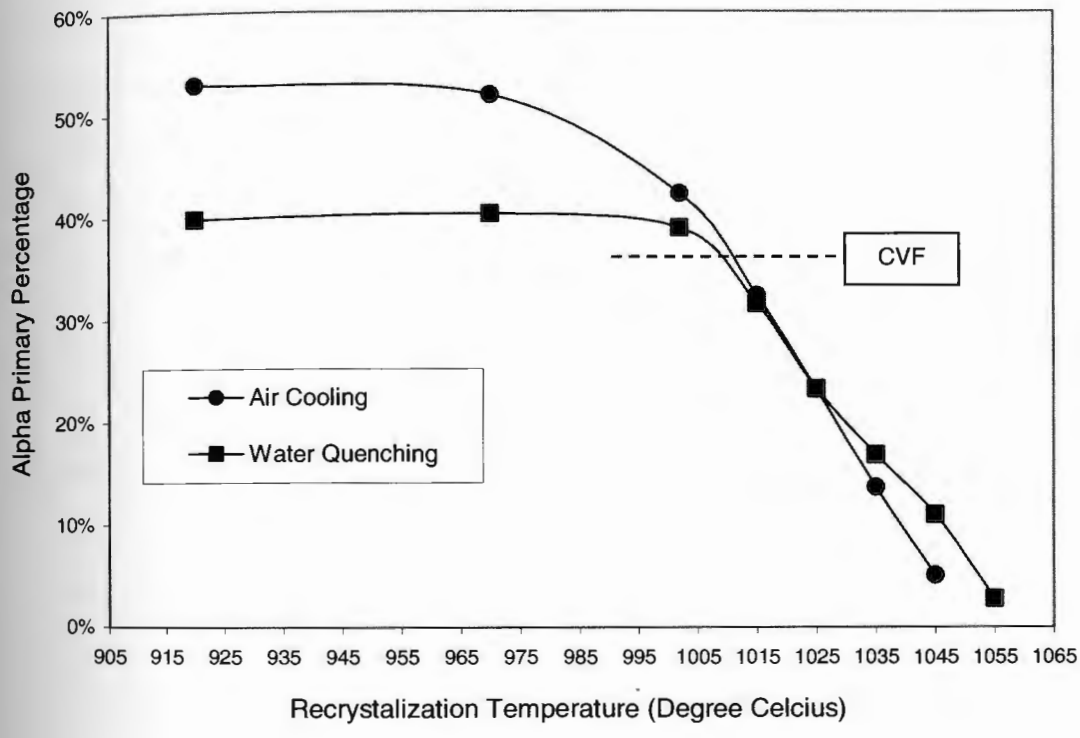

Figure 2-17: Effect of cooling rate on the α_p volume fraction of IMI 834.

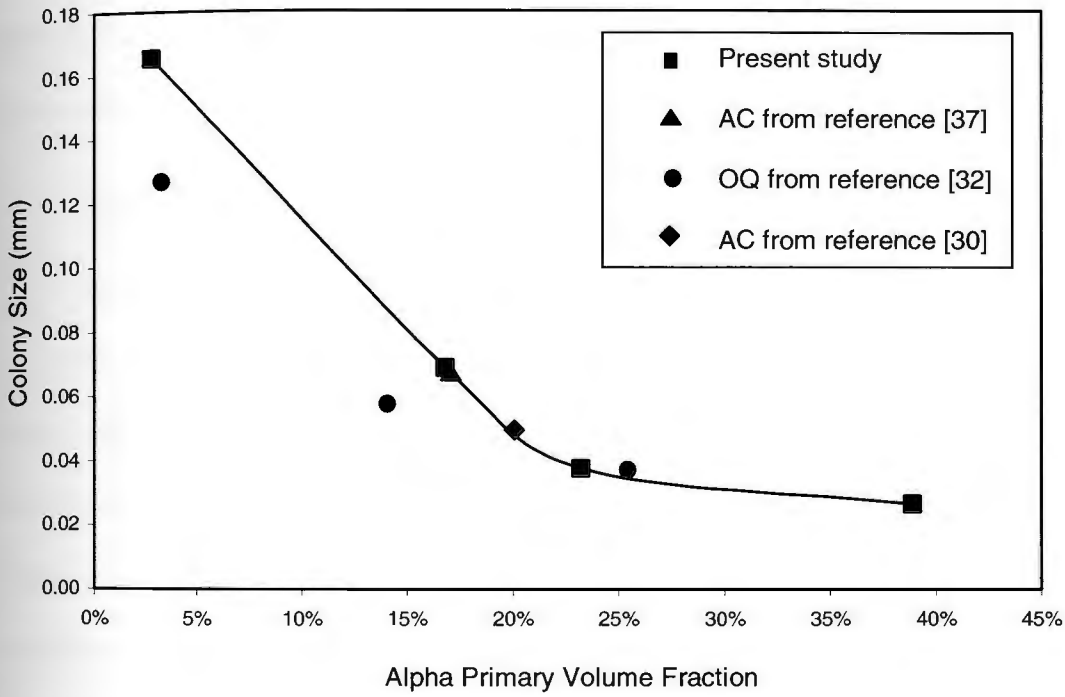

Figure 2-18: Colony size measurements from selected water-quenched specimens and from literature for IMI 834.

2.2.2 Influence of Heat Treatment on the Hardness Characteristics of IMI 834

The influence of heat treatment on the hardness characteristics of IMI 834 was studied by performing Rockwell "C" hardness (R_C) tests on selected specimens. Hardness value changes are generally correlated to changes in the yield stress (σ_y) behavior in a material. The following section describes the experimental procedure and discusses the results obtained when measuring the hardness of IMI 834 at room temperature.

2.2.2.1 Experimental Procedure

Macro-hardness measurements were performed at room temperature on the heat-treated and aged specimens of both water-quenched and air-cooled conditions. These tests were performed using a semi-automatic Rockwell "C" testing frame built by the Wilson Manufacturing Company. Prior to testing, calibration of the frame was done using "master" samples of 44.0 R_C, 62.8 R_C and 64.0 R_C. Maximum error of $\pm$ 0.7 R_C was found after twenty-five measurements. The size of the indent was approximately 1 mm. The results reported in this study are the average of twenty-five hardness measurements. In addition to testing the water-quenched and air-cooled materials, a third heat-treatment was added to the study. A specific heat treatment, designated as Post-Age Heat Treatment (PAHT) [53], was made on the water-quenched material to remove the existing Ti_3Al particles. Studies by Madsen and Ghonem [49] and by Zhang et al [40] show that α_2 is not present in titanium alloys when the material is heat treated above the solvus

temperature of the particle. The PAHT, illustrated in figure 2-19, corresponds to an additional annealing at 850°C for 2-hours of IMI 834 specimens followed by air-cooling.

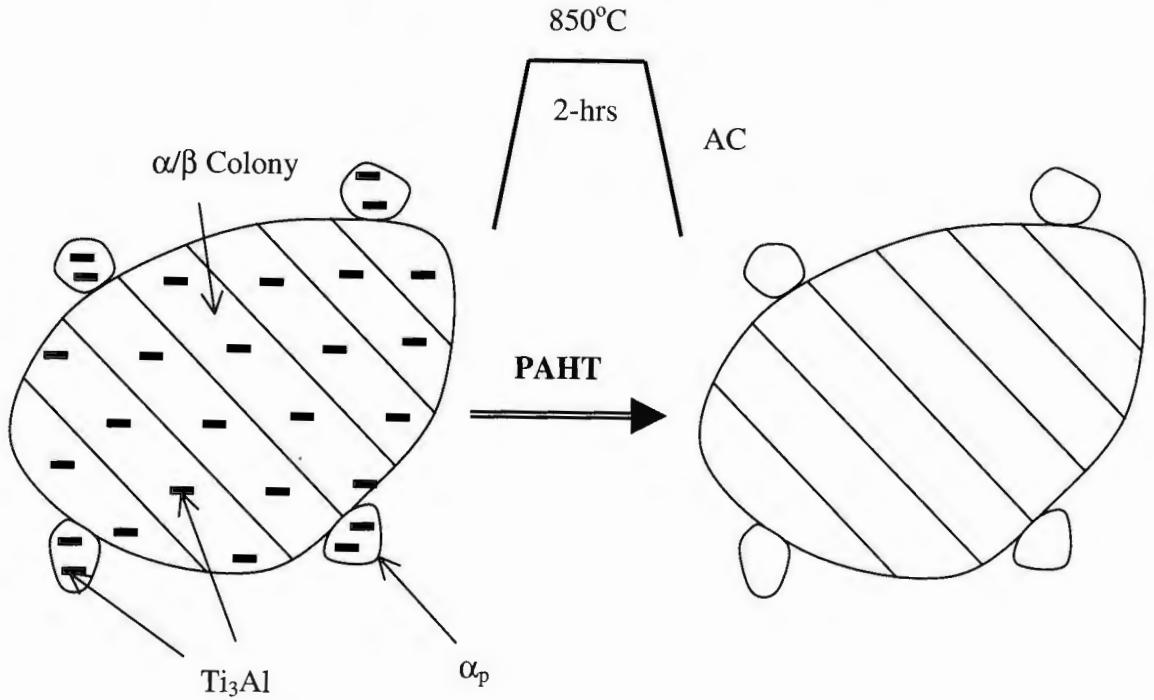

Figure 2-19: Schematic representation of Post Age Heat Treatment (PAHT) process in IMI 834.

2.2.2.2 Results and Analysis

Figure 2-20 represents the hardness test results for the water-quenched and air-cooled materials. For water-quenched IMI 834, a maximum of about 40 R_C is reached over the α_p volume fraction interval of 11%-32%. In the air-cooled material, a maximum of 31 R_C is reached and maintained over a comparable interval, 13% - 33% α_p volume fraction. This result is in agreement with the fact that water-quenched material has a lower maximum α_p vf, as shown in figure 2-17, and that the α-phase has a lower yield stress than the β-phase, as illustrated by the constitutive equation for each phase seen in figure 2-21 [54]. Despite the four Rockwell "C" separations between the two materials in the 15%-33% vf interval, their behavior is parallel. These observations are analogous to those reported in section 2.2.1.2, where, independently of the recrystalization cooling rate, water-quenched and air-cooled specimen α_p volume fractions appeared similar over the 15-35% interval. Further analysis of figure 2-20 shows that the minimum hardness of the two materials is equivalent at about 31 R_C, however, for the air-cooled material it is only reached at the significantly higher α_p volume fraction of 52% compared with the water-quenched at around 40%. Figure 2-20 also shows that hardness values decrease in both water-quenched and air-cooled specimens for α_p volume fraction values lower than 12% and higher than 32%. These results are in good agreement with work done by Lütjering [9] on near-alpha titanium alloys, where this phenomenon is attributed to the interaction between partitioning element effect and material colony size as previously discussed.

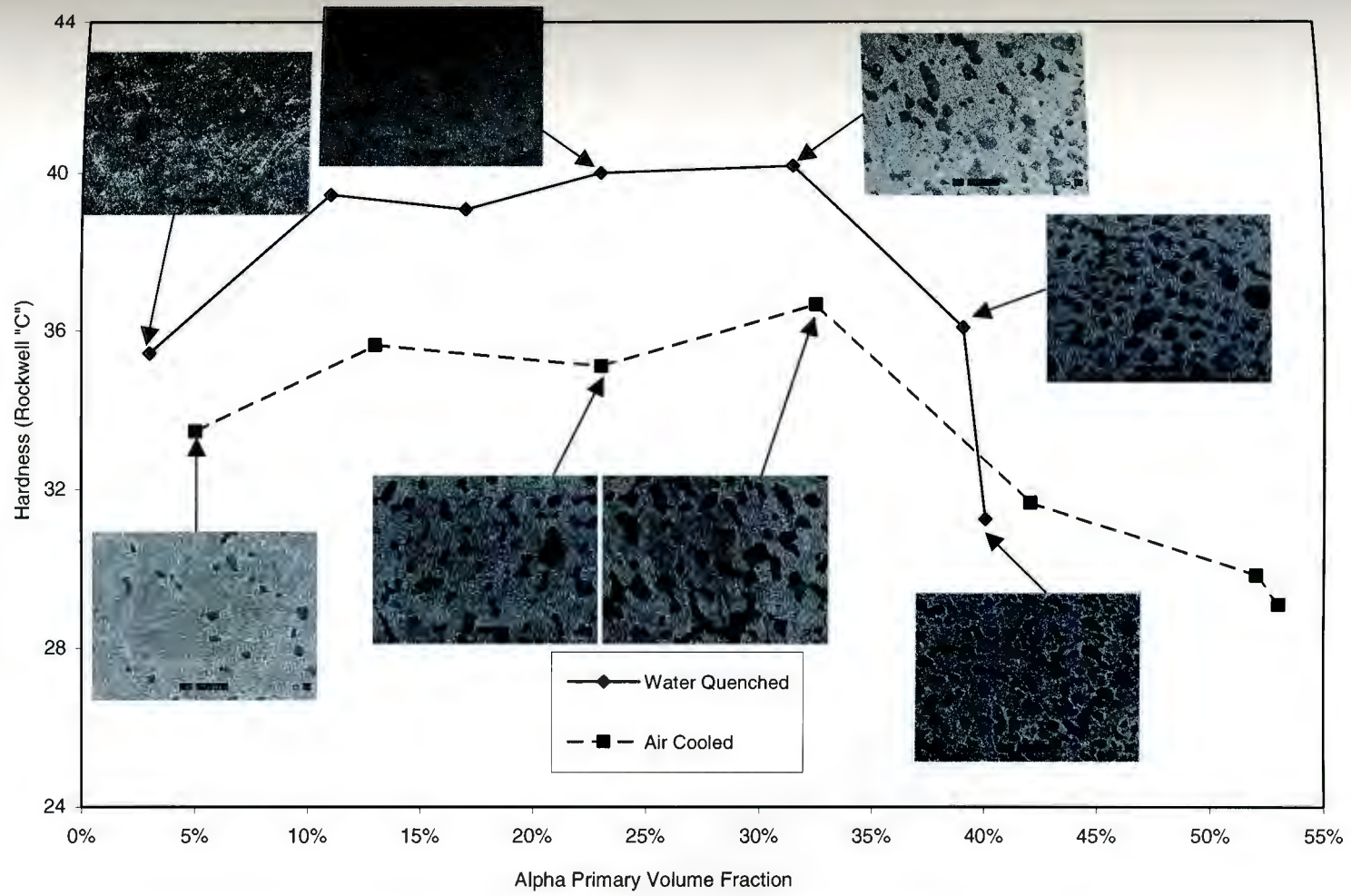

Figure 2-20: Rockwell "C" hardness results for water-quenched/aged and air-cooled/aged IMI 834.

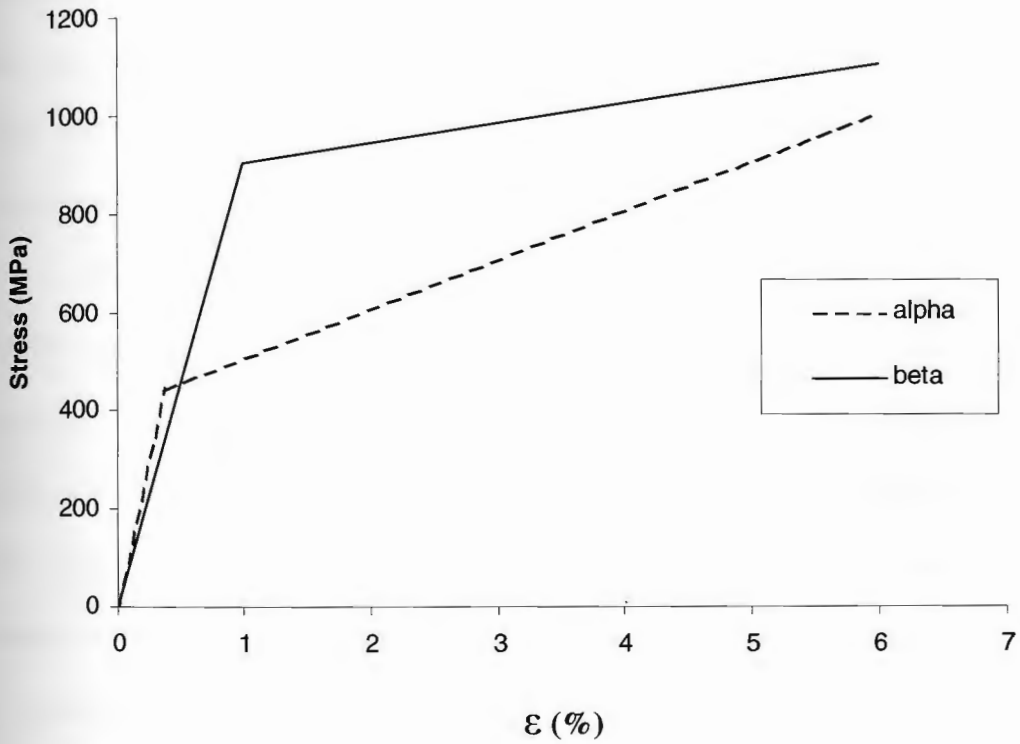

Figure 2-21: Stress-strain curves for α and β (from ref. [54]).

The effect of PAHT is shown in figure 2-22. This figure shows that the maximum and minimum hardness values for the PAHT material are about 38 R_C and 25 R_C at approximately 3% and 40% α_p volume fractions, respectively. Additionally, figure 2-22 shows that, in general, the removal of Ti_3Al from solution decreases the hardness of the material. This result agrees with the previously discussed studies that show that Ti_3Al particles harden the material. For α_p volume fractions lower than 15%, the PAHT material shows a rise in hardness compared to the water-quenched material. This result is likely to be caused by the colony size effect mentioned earlier and by the formation of silicides that will be discussed in the following chapter.

Figure 2-23 shows the difference in hardness between water-quenched and PAHT specimens. More importantly, however, this figure represents the partitioning element effect in the water-quenched alloy. Differences in hardness between the aged and post aged material are caused by changes in Ti_3Al content. The greater the hardness difference between the two materials, the greater the amount of Ti_3Al particles that are dissolved in the PAHT. Since Ti_3Al precipitation is limited by the amount of aluminum in solution at the alpha phase, it can be assumed that the higher the hardness difference between the aged and the PAHT material, the higher the aluminum content in the alpha phase. Therefore, it may be concluded that figure 2-23 is a representation of the aluminum partitioning effect of the water-quenched IMI 834. Analysis of the figure shows that the partitioning element effect is negligible at low volume fractions, and that it only starts to appear at volume fractions above about 10%. For volume fractions between 10% and

33%, the aluminum partitioning element effect remains relatively unchanged. The effect shows another increase, for α_p volume fractions above about 33%.

Figure 2-24 is a schematic of the effect of PAHT on hardness for low and high α_p volume fractions, as interpreted from figure 2-23. The figure shows that for low α_p volume fractions, the removal of Ti_3Al from solid solution results in little to no change on the material hardness. On the other hand, for high α_p volume fractions, hardness changes occur with Ti_3Al removal.

Figure 2-25 is a representation of the colony size and partitioning effects on the water-quenched IMI 834 specimen. This figure shows the partitioning element effect dominating in the region of large α_p, decreasing the hardness of the material as shown in figure 2-24. Similarly, the hardness of the material decreases as the colony size effect becomes dominant, as shown in figure 2-18. For microstructures between about 10% and 33% α_p volume fraction, the combination of the two effects appear to have little impact in the material hardness. When comparing the cooling rate effect, see figure 2-20, it appears that the air-cooled alloy experiences a similar trend. However, colony size effect shows a greater rate of change in the water-quenched than the air-cooled material. This observation is in agreement with Lütjering [13] as seen in figure 2-10, where the α_p volume fraction is a function of the recrystalization temperature, whereas the colony size is a function of the recrystalization cooling rate. Additionally, the partitioning element effect appears to be more severe in the air-cooled material, which agrees with studies that show that element partitioning increases with decreasing cooling rates.

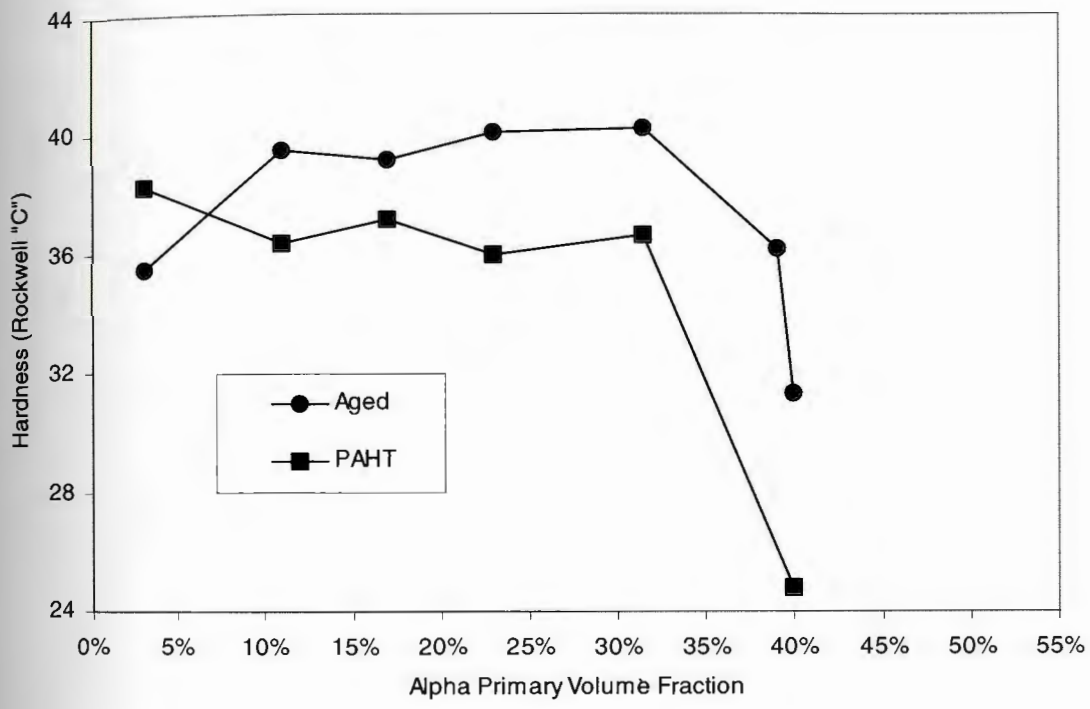

Figure 2-22: Effect of α_2 removal on hardness R_C in IMI 834.

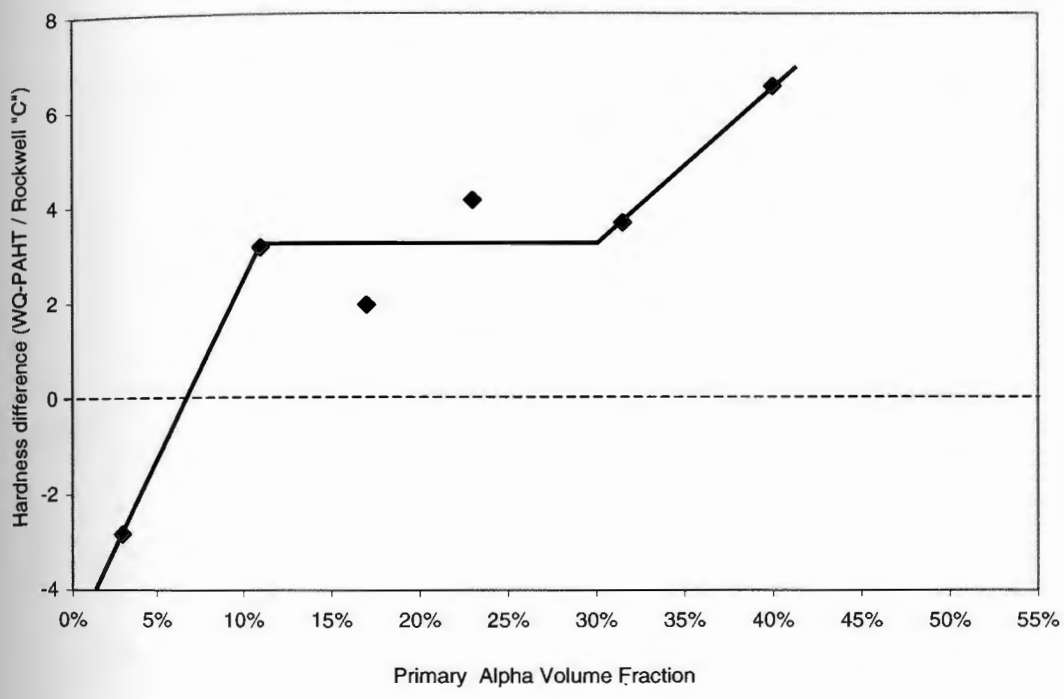

Figure 2-23: Difference of Rockwell "C" hardness results for water-quenched/aged and water-quenched/aged/PAHT IMI 834.

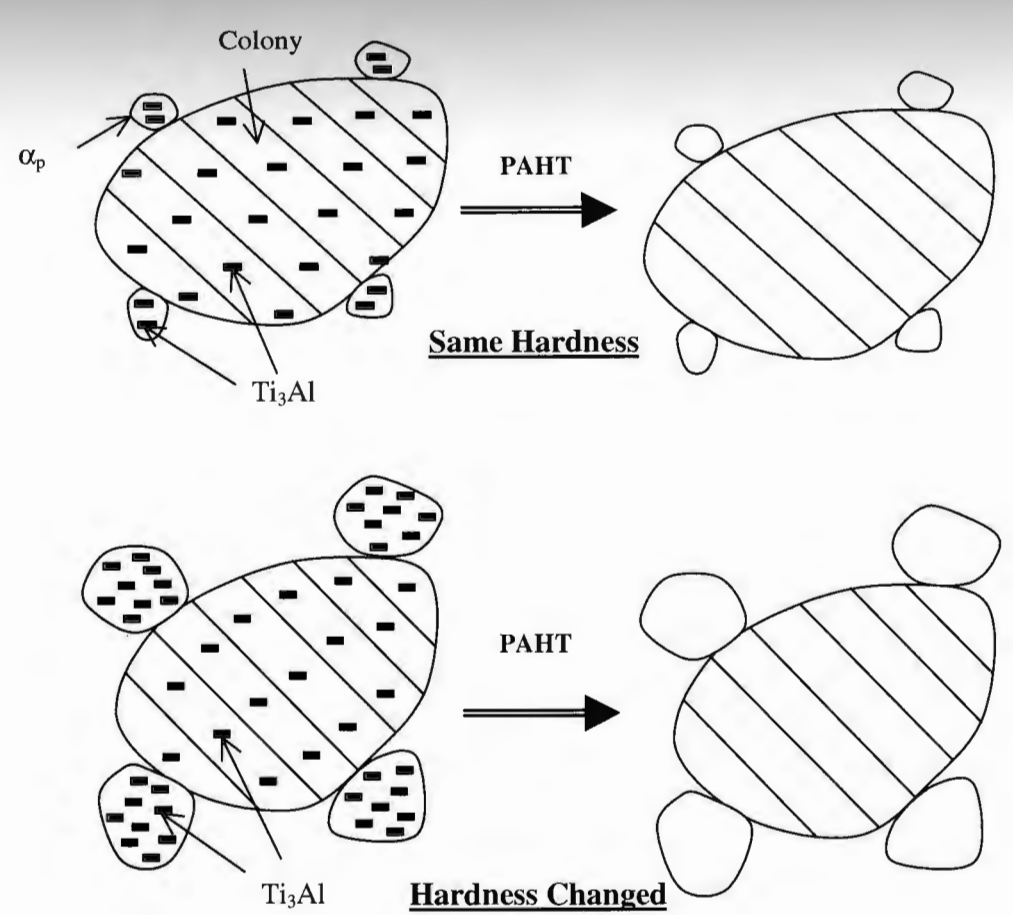

Figure 2-24: Effect of PAHT on hardness of low and high α_p volume fraction of IMI 834.

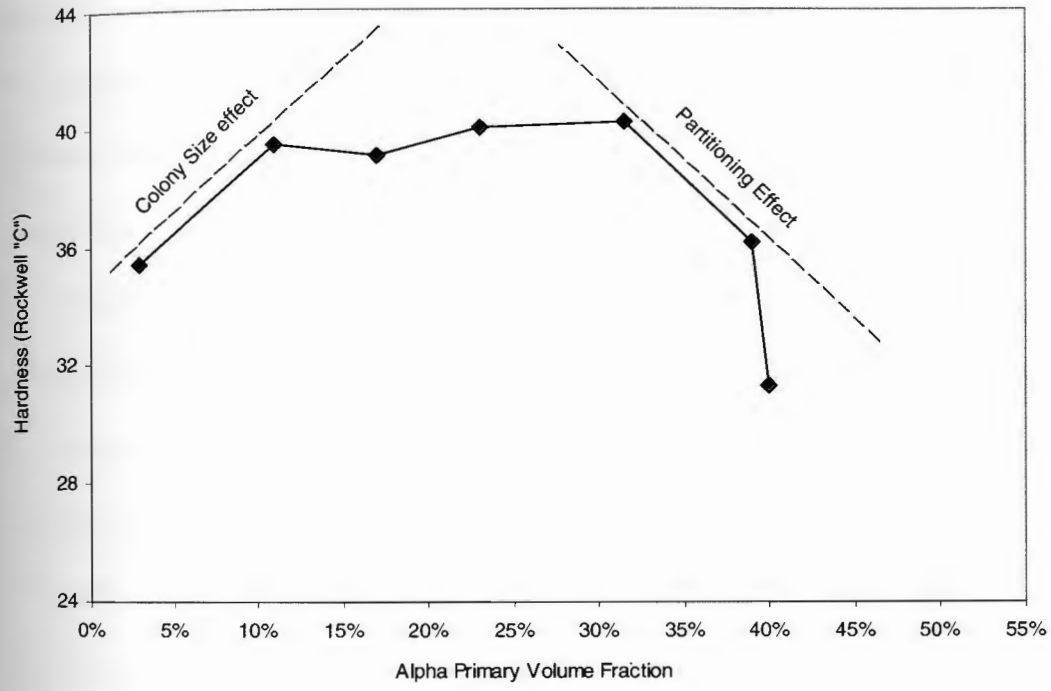

Figure 2-25: Colony size and partitioning element effects for-water-quenched IMI 834 specimens.

2.3 Summary and Conclusions of Chapter 2

The physical metallurgy of titanium alloys has been discussed in this chapter, with emphasis on near-alpha materials. A description of the different alloy elements used with titanium and their influence on the material mechanical properties was presented and commented. Details on the phase morphology of the material of study, IMI 834, as well as the heat treatment process and its effect on the mechanical properties were also given. Heat treatments of IMI 834 using different recrystalization temperatures and cooling rates led to the following conclusions:

1. Maximum α_p volume fraction values for air-cooled specimens were higher than that of the water-quenched by approximately 12%.
2. Regardless of the cooling rate following the recrystalization process, aged IMI 834 shows the same α_p volume fraction when recrystalized between 1010°C and 1035°C.
3. In general, material recrystalized and aged has higher α_p volume fraction than material only recrystalized.
4. Colony size decreases as α_p volume fraction increases. Above 20% α_p volume fraction, the colony size remains constant.

Hardness measurements showed the following features:

1. For the same α_p volume fraction, air-cooled specimens have lower hardness than water-quenched specimens.

2. All heat treated material shows constant hardness between 15% and 33% α_p volume fraction.

3. Hardness values increase between 3% and 12% α_p volume fraction. Hardness values decrease for α_p volume fractions higher than 32%. Between 12% and 32% α_p volume fractions hardness values show little change.

4. PAHT shows that Ti_3Al particles play a role on the material hardness only when they are concentrated within the α_p. For small α_p volume fractions, hardness changes due to PAHT are small, whereas, for large α_p volume fractions, hardness changes are large. Comparison between aged and PAHT material hardness gives a good representation of the aluminum partitioning effect.

Chapter 3: Long Term Exposure Effects at 650°C on the Structural Stability of Near-α Alloys

Introduction:

This chapter describes the role of over-aging on the structural stability of near-α Ti alloys. For the purpose of this study, over-aging indicates that the material is submitted to long-term exposure at 650°C following various heat treatments and aging at 700°C for 2-hours. The first section is a review on the effects of over-aging on aluminide and silicide precipitation and their implication on room temperature yield stress. In the second and last section, experiments are performed that show the significance of over-aging at 650°C on IMI 834. Results and analysis are also provided.

3.1 Role of Long Term Exposure at Elevated Temperature on the Structural Stability of Titanium Alloys

Near-alpha titanium alloys are not usually in a state of equilibrium after initial processing due to the relatively fast cooling rates from the forging and annealing treatments. Among the elements added to titanium alloys, aluminum and silicon are the most influential in material mechanical properties at elevated temperatures. Low concentrations of aluminum are used in these alloys as strengtheners and alpha-phase stabilizers [13], whereas silicon is added to technical titanium alloys to improve material creep resistance [23]. The formation of coherent ordered Ti_3Al particles (see figure 3-1) and incoherent $(Ti,Zr)_5Si_3$ /

$(Ti,Zr)_6Si_3$ during the aging and overaging phases accounts for the biggest changes in the near-alpha titanium alloy mechanical properties, such as hardness, UTS, and creep-fatigue behavior [13, 20, 23, 47, 49]. However, changes in the material microstructure as a function of the thermo-mechanical exposure during high temperature (550°C-650°C) applications can lead to material failure. Liu et al [55] described the structure evolution of Ti-Al-Si systems in three stages: the first stage is the crystallization amorphous phase producing silicides; the second stage is crystallization of the remaining amorphous phase producing aluminides; and the last stage is the grain growth of all phases. To better understand the overall mechanical behavior of near-α titanium alloys at elevated temperature, a detailed look at the growth phase or over-aging phase of aluminides and silicides will follow.

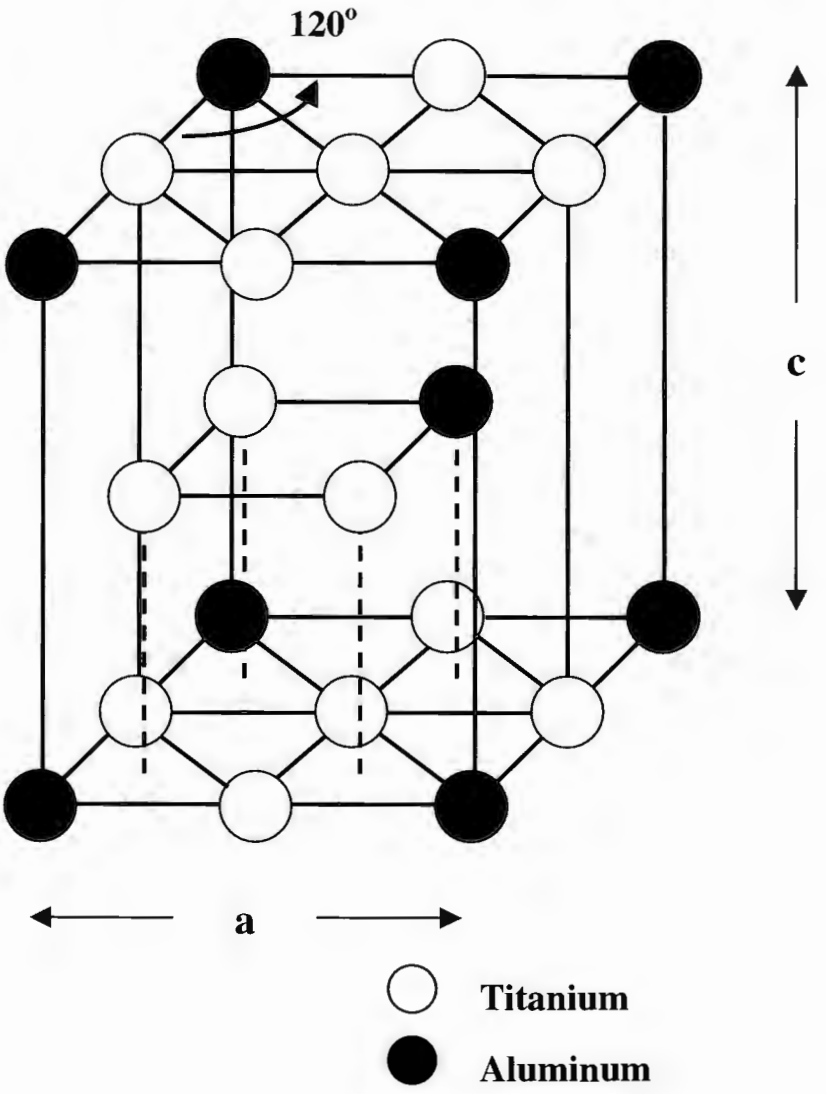

Figure 3-1: Lattice Structure of α_2 (Ti_3Al) intermetallic.

3.1.1 Effects of Over-Aging on Aluminides

Following the recrystalization process on near-alpha titanium alloys, aluminum remains in solid solution in the alpha-phase regions. The equilibrium phase Ti_3Al, also known as aluminides (α_2), is dependent on a number of factors including aluminum and oxygen concentrations, heat treatment, aging temperature and aging time of the alloy [40, 56]. These factors and their influence on the formation of α_2 precipitates during long term exposure at elevated temperatures is discussed in this section.

Based on the binary Ti-Al phase diagram, it is predicted that the α_2-phase will form in titanium alloys containing over 8.0 wt% Al [57]. However, the interstitial oxygen impurity level may have a significant effect on the α_2 precipitation behavior since this element is a strong α_2-stabilizer. Increases in oxygen content have been shown to shift the $\alpha \rightarrow \alpha + \alpha_2$ boundary in Ti alloys with lower aluminum content by raising the α_2 solvus temperature [58, 59]. In fact, studies performed on the near-alpha Ti-1100, with 6.0 wt% Al and 0.078 wt% O, show that α_2 was present when aging at 593°C [49]. Furthermore, Partha et al found when studying the near-α titanium alloy IMI 834, with only 5.86 wt% Al but 0.1 wt% O, that α_2 particles are present when the material is aged at 600°C [44]. Alloying elements such as V, Sn, and Zr have been determined to have a detrimental influence on the oxidation behavior of titanium alloys. In contrast, additions of Mo, Nb, Si and Al reduce the oxidation rate [60]; however, the addition of these elements to high temperature near-alpha titanium alloys is

relatively low since the aluminum equivalent has to be kept below about 9% to avoid embrittlement [60].

Studies have shown that α_2 precipitation behavior is sensitive to the heat treatments and aging temperatures applied to the alloy [44]. Zhang et al [40] showed that when the microstructural morphology of the titanium alloy Ti-6-22-22 consisted of martensite plates (when cooled at rates $\geq$ 5.5°C/s), neither α_2 nor retained β-phase were observed. On the contrary, when cooling rates are lowered to form a relatively fine Widmanstätten/aciculate structure, α_2 started to precipitate. Qualitatively, the same authors observed that the relative intensity of the α_2 superlattice reflections with respect to the fundamental α reflections, increased with decreasing cooling rates.

Aging temperatures have also been shown to have an effect on the precipitation of α_2. Studies on IMI 834 with approximately 5%, 15% and 25% α_P [44] show that when aging at 600°C Ti_3Al precipitates within the primary alpha only, whereas aging at 700°C causes ordering in both primary and the α/β colony. In these studies, it is also shown that aging at 700°C for 2-hours was sufficient to reach stability of the α_2 precipitates. The later result suggests, therefore, that the aging treatment conducted in the current study, as mentioned in chapter 2, is sufficient to precipitate all α_2 phase in the material. Furthermore, studies on IMI 834 at 650°C and 750°C indicate that oxygen becomes more soluble and mobile at high temperatures, which further stabilizes the α_2 phase [25, 42].

Finally, when in the precipitation temperature range, α_2 particles show changes in size with aging [40]. The ratio of lattice parameters $a_\alpha/a_{\alpha 2}$ in both Ti-6-22-22 and IMI 834 alloys have a value of approximately 0.5 and have been considered to cause negligible misfits between the two phases [36, 40]. The lattice parameters for α found in Ti-6-22-22 were **a** = 29.7 nm, **c** = 46.9 nm and for α_2 they were **a** = 59.3 nm, **c** = 46.9 nm. However, aging of the Ti-6-22-22 alloy for 1,000-hours at 650°C showed the lattice parameters of α and α_2 to be **a** = 28.9 nm, **c** = 46.9 nm and **a** = 58.7 nm, **c** = 46.9 nm, respectively. This suggests that the **c**-lattice parameter is not affected by long time aging treatment, whereas the **a**-lattice parameters decreases by about 2.6% for the α-matrix and about 1% for the α_2 precipitates [40], thus maintaining the $a_\alpha/a_{\alpha 2} \approx 0.5$ seen before long term aging. It has also been shown that aging causes significant changes in aluminide size [40]. When exposed to 600°C for 30-hours, α_2 precipitates in Ti-6-22-22 grew from a spherical shape, with sizes of about 1-2 nm, to much more stable α_2 precipitates, with sizes up to 5-10 nm in diameter and 20-50 nm in length. Zhang et al [40] explain this change based on the lattice mismatch between α_2 precipitates and the α matrix (about 1.5% in this case) and the resulting strain fields generated at their interface.

3.1.2 Effects of Over-Aging on Silicides

Like aluminum, silicon also stays in solid solution after rapid cooling following the initial heat treatment of the alloy. Madsen and Ghonem [47] showed that when aging Ti-1100 at 593°C, silicides start forming before aluminides,

however, they add, silicide stability is reached after that of the aluminide. Incoherent silicides are found predominantly on the α' platelet boundaries in the α/β colonies of lamellar microstructures alloys [25]. However, in duplex microstructures, silicides are found at the interfaces of α' and at the martensite boundaries of the primary α and the colonies [20, 29, 44]. Silicides change in size and shape depending on a number of factors including: the concentration of β-stabilizers, heat treatment, aging temperature and aging time of the alloy [40, 56]. These factors and their influence on the formation of silicide precipitates during long term exposure at elevated temperatures will now be discussed.

Two types of hexagonal silicides, S_1 with lattice parameters **a** = 0.78 nm, **c** = 0.54 nm, and S_2 with lattice parameters **a** = 0.70 nm, **c** = 0.36, have been identified by Ramachandra and Singh [61] to form in silicon bearing titanium alloys. They were found to coexist in the water quenched, 650°C to 800°C aged conditions in the alloy Ti-5Zr-1Si using X-ray and electron diffraction techniques [45]. In the water quenched near-α titanium alloy 685, which contains smalls amount of β-stabilizers, S_1 and S_2 silicides were found when the material was aged below 650°C [61]. However, aging of IMI 829, where β-stabilizing elements are higher than in IMI 685, showed the presence of both silicides at temperatures lower than 625°C [19]. Between 625°C and 950°C only S_2 type silicides were found. In the alloy IMI 834, only silicides S_2 precipitated following aging in the temperature range of 600°C to 700°C [20]. Comparison of the aforementioned results shows that S_2 type silicides tend to precipitate at lower temperatures as β-stabilizing

elements are added to titanium alloys. For the purpose of this study, where aging is performed at 700°C for 2-hours and overaging performed at 650°C, it will be assumed that S_2 are the only silicides present.

Additional considerations on silicon bearing alloys are given by Ghosal et al [44] on the study of the near-α IMI 834 alloy in the α+β phase field. In this study, oil-quenched materials are used, heat-treated at 1015°C, 1030°C, and 1045°C. No silicides were observed on the three materials after solution treatment, but after aging at 700°C for 2-hours they observed different average size of silicides type S_2 were observed; see table 3-1 for details. The results shown in this table indicate that the higher the solutioning temperature, the finer the silicide precipitates. These authors believe that a possible reason for this difference is the relative increase in the amounts of the β-stabilizing elements in the reduced volume fractions of α/β colonies with the lowering of the α + β solution treatment temperature, resulting in accelerated precipitation. A Schematic representation of table 3-1 results is shown in figure 3-2.

In addition to size changes, Shridar and Sarma [19] also found significant shape changes on S_2 type silicides when aging the IMI 829 alloy at different temperatures for 24-hours. At aging temperatures of 625°C and 700°C, the particles had approximately the same size and were lenticular in shape with an aspect ratio as high as 10 (e.g., a = 200 and b = 20 nm) (see table 3.2). As the aging temperatures increased to 800°C and above, the particles became ellipsoidal with a maximum aspect ratio of only 1.5. They reached the maximum size of 700nm, the width of the α' platelets, after aging at 950°C. Figure 3-3 is a

schematic representation of the results from table 3-2. Figures 3-4, 3-5 and 3-6 represent schematically the evolution of the formation of silicide precipitates at the α' boundaries observed on IMI 829 alloy using Transmission Electron Microscopy (TEM) after aging at 625°C, 700°C, and 800°C, respectively [19].

Solution Treatment	Average Size* of S_2 type silicides (nm)
1045°C	31 Φ
1030°C	a = 81, b = 40
1015°C	a = 300, b = 180

*Table 3-1: Average size of silicides after oil quenching different solution treatments for 2-hours followed by aging at 700°C for 2-hours on IMI 834 (from reference [44]). *(Size determination from projected images a and b refers to major and minor axes of the projected ellipsoid).*

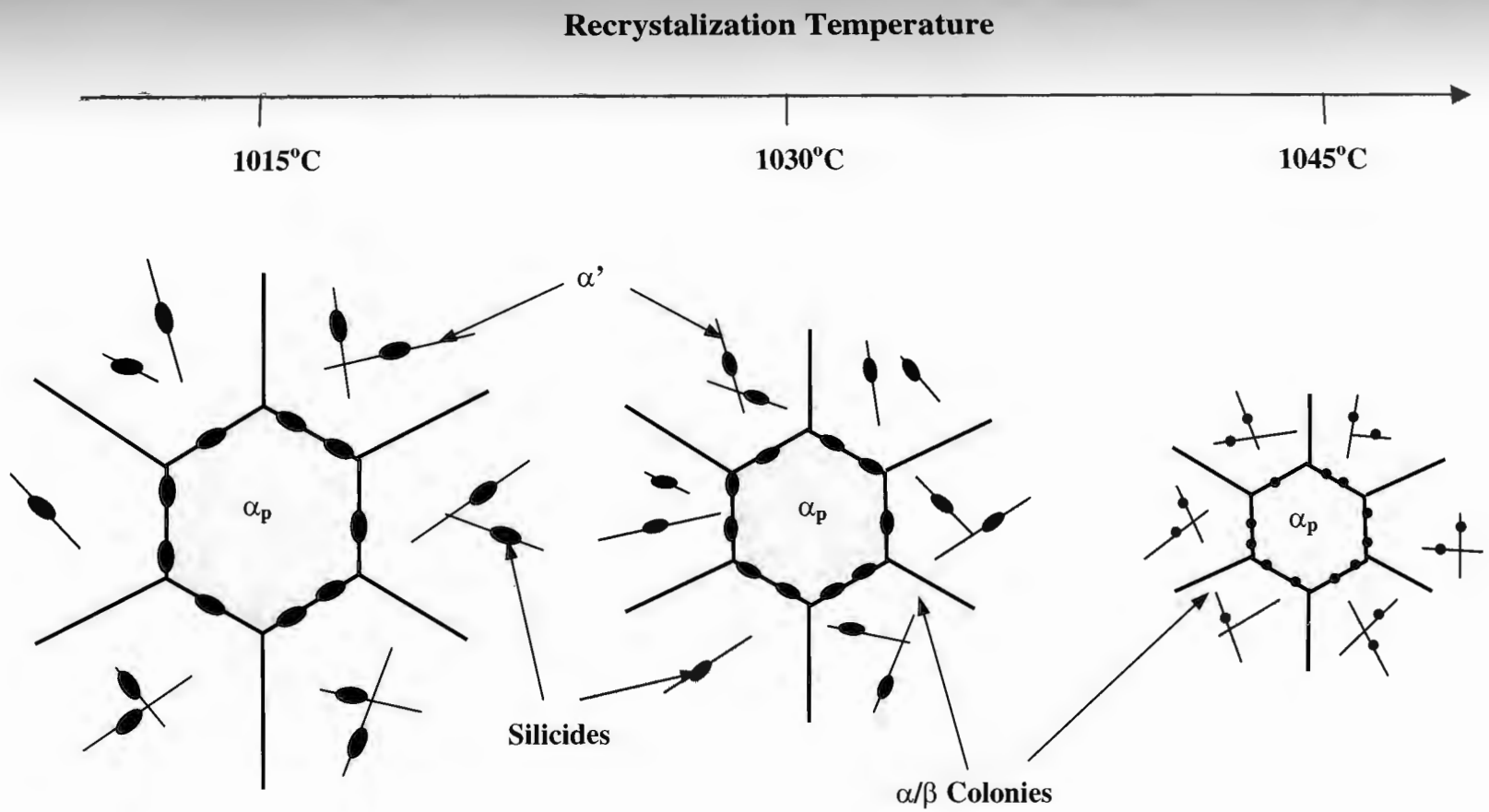

Figure 3-2: Schematic representation of silicide average size and shape change with recrystalization temperature (from table 3-1).

Aging Treatment for 24-hours AC	Average Size* of S_2 type silicides (nm)
none	none
625°C	a = 200, b = 20
700°C	a = 200, b = 20
800°C	300 Φ
950°C	700 Φ

*Table 3-2: Average size of silicides after water quenching solution treatments at 1050°C and aging for 24-hours followed by air-cooling at various temperatures on IMI 829 (from reference [19]). *(Size determination from projected images a and b refers to major and minor axes of the projected ellipsoid.).*

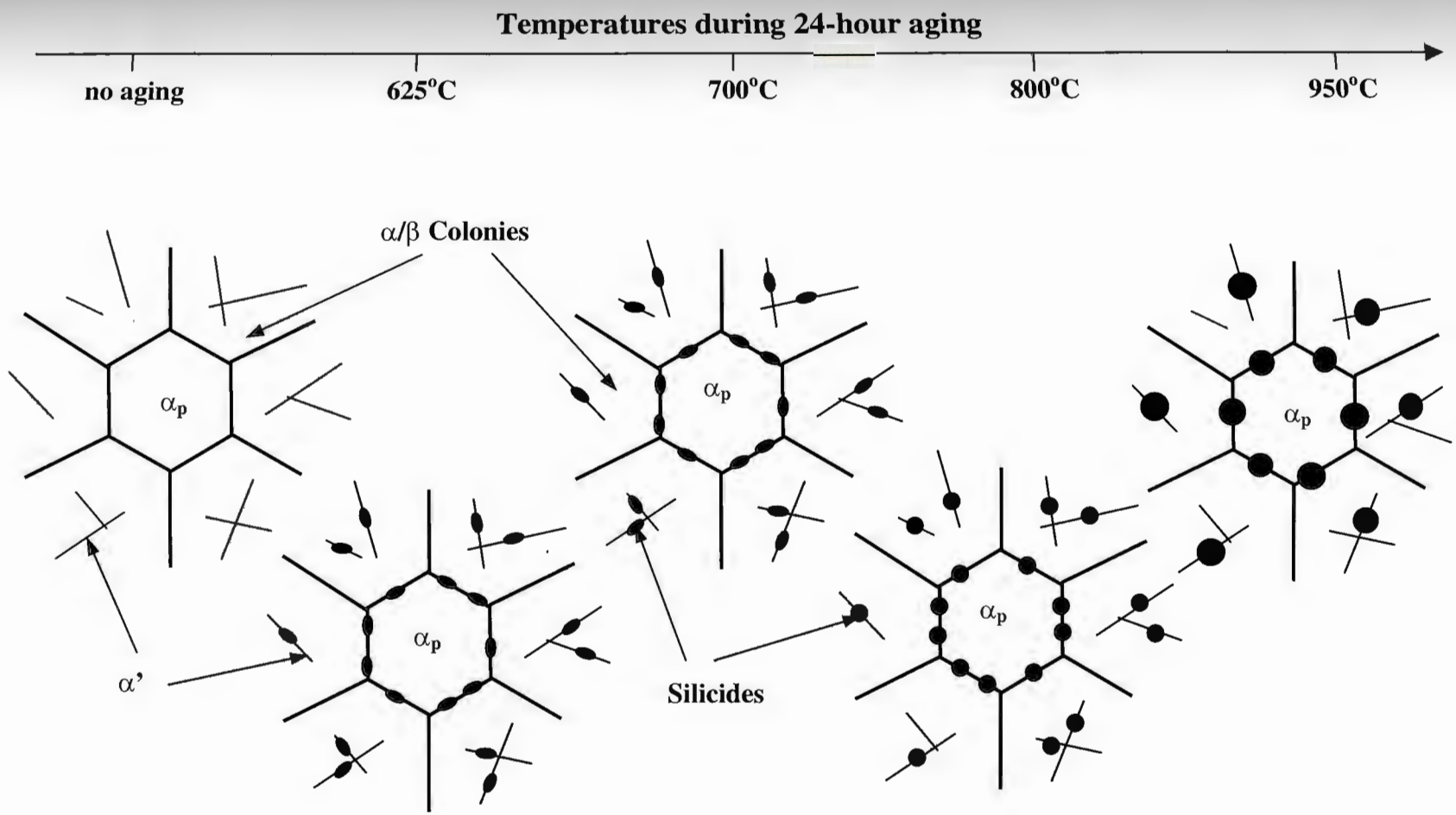

Figure 3-3: Schematic representation of silicide growth and shape change with aging temperature over 24-hours (from table 3-2)

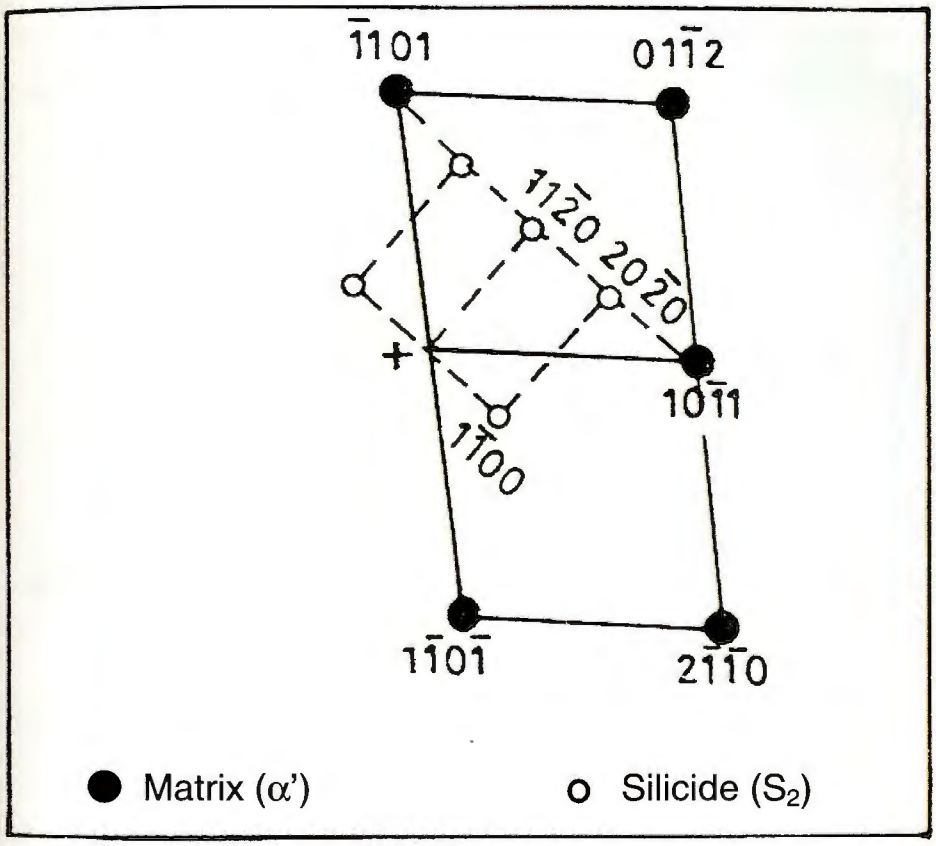

Figure 3-4: Schematic representation of TEM observations of IMI 829 aged for 24-hours at 625°C (from ref. [19]).

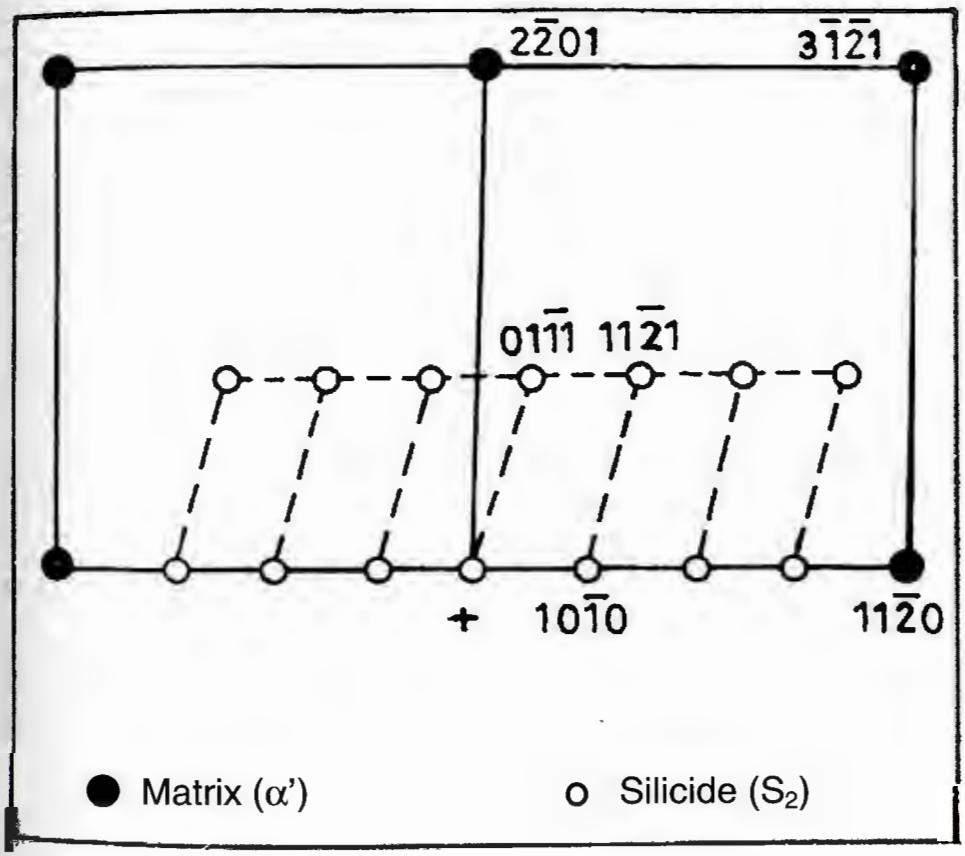

Figure 3-5: Schematic representation of TEM observations of IMI 829 aged for 24-hours at 700°C (from ref. [19]).

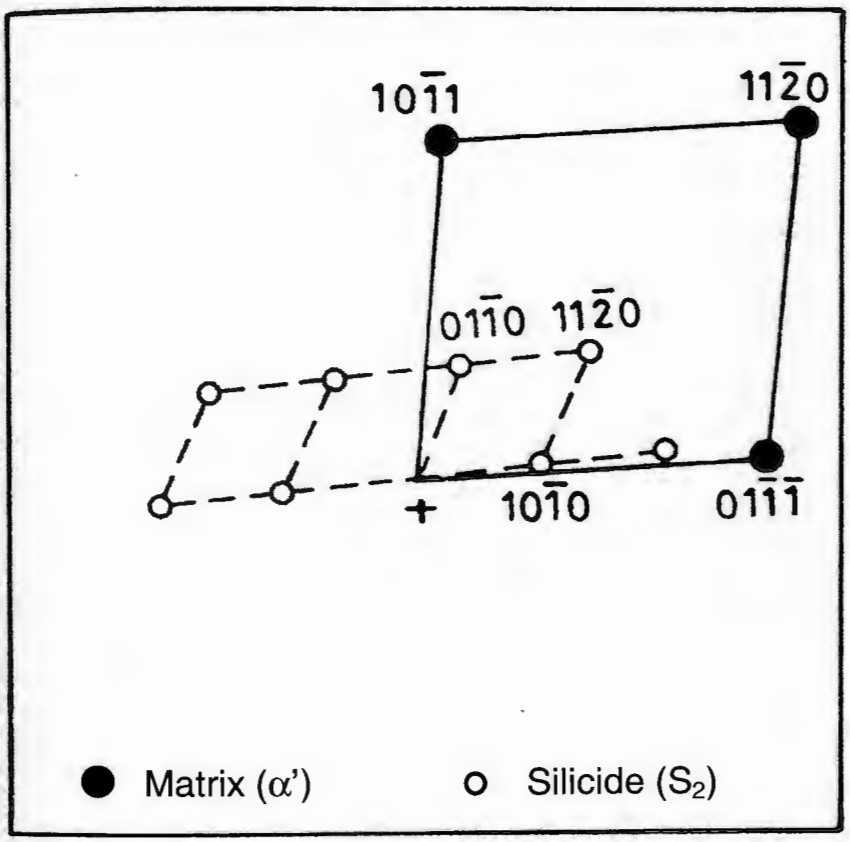

Figure 3-6: Schematic representation of TEM observations of IMI 829 aged for 24-hours at 800°C (from ref. [19]).

3.1.3 Role of Over-Aging on Room Temperature Hardness

As discussed in the previous section, changes in the size and shape of aluminides and silicides occur as the alloy chemical compositions change as well as when the alloy is exposed to elevated temperatures for extended periods. One way to examine how these changes occur in an alloy is by performing hardness measurements. By changing the chemical composition while keeping all other variables fixed, hardness tests may help to separate the individual effects of elements. Likewise, by maintaining the same chemical composition and changing the temperature that the alloy is exposed to, conclusions may be drawn pertaining to the effects of temperature on the material hardness. In the following sections, studies performed on different alloys over a range of temperatures are shown and detailed analysis are performed to relate the changes in hardness to the changes in the size and shape of aluminides and silicides. When analyzing age-hardening results, attention is given in particular to the relative shape changes in the hardness curves, to maximum hardness points (peaks), and to decreases in hardness. Shape changes are normally considered to be caused by changes in the types of precipitate formed. Hardness peaks are associated with attaining a critical particle size. Finally, precipitate growth beyond the critical particle size causes a decrease in hardness.

Figure 3-7 shows changes in hardness when a Ti-5%Zr-1%Si alloy is aged over an extended period at 500°C, 550°C, and 650°C [45]. Applying the method of analyses previously described, it appears that between 500°C and 550°C, as well as between 550°C and 650°C, there are changes in the type of precipitate formed as

the two curves differ in shape from each other. Furthermore, aging at 650°C shows two hardness peaks, indicating the presence of two precipitates. In fact, both of these observations appear to be substantiated. As discussed in the previous section of this report, studies show that when aging titanium alloys with zirconium and silicone above about 500°C (depending on the chemical composition of the alloy), two types of silicides are formed, S_1 and S_2 [20, 23, 44]. Furthermore, the two silicides were found to coexist below a close range of temperatures, depending on the chemical composition of the alloy, but at higher temperatures, only S_2 type silicides were found. Some examples include the studies on IMI 829, IMI 685, IMI 834, and Ti-1100, where aging at temperatures below 575°C, 650°C, 550°C, and 593°C, respectively, resulted in the formation of both S_1 and S_2 precipitates. The same studies show that above those temperatures, only S_2 type precipitates were evident.

Figures 3-8 and 3-9, respectively, show the effect of silicon content and aging temperature on the binary Ti-1%Si alloy. In figure 3-8, aging a Ti-Si alloy at 550°C, where the silicon concentration varies between 1.0% and 2.39%, shows the same general hardness curve shape with one hardness peak. In this figure, it is worth noting, however, the change on the rate of precipitate growth beyond critical size. For the Ti-2.39%Si alloy, the growth occurs at a much higher rate compared to the 1% silicon alloy. This effect is supported by studies that show that changes in the volume fraction of $\alpha+\beta$ titanium alloys, where concentrations of silicon vary between phases, cause changes in the size of the silicides precipitated for a given heat treatment [44]. One explanation could be that the higher concentration of

silicon promotes faster precipitation of silicides, causing the critical precipitate size and grain growth to occur sooner. In figure 3-9, aging of the Ti-1%Si at 500°C, 550°C and 650°C shows that with removal of zirconium from the alloy, the silicide variants S_1 and S_2 are unable to form. Instead, the phase Ti_5Si_3 is formed. Hence, the second peak found at 650°C in figure 3-7 does not appear in figure 3-9. One variation in figure 3-9 relative to figure 3-7 is that at 500°C, the figure shows a hardness peak after aging for approximately 60,000 minutes, which may be indicative of the formation of a different precipitate. As the alloy in figure 3-9 is aged at higher temperatures, the precipitate growth becomes more pronounced. These results are in agreement with studies performed on silicon bearing titanium alloys aged over a wide range of temperatures that showed rapid increases in silicides precipitation with increasing temperatures [19].

The effects of aluminum content on the aging characteristics of Ti -5%Zr-1%Si- Al alloy at 550°C are shown in figure 3-10. The most striking effect seen when aluminum is added to the alloy is the sharp decline in the precipitate growth rate. Whereas the Ti-5%Zr-1%Si alloy shows a relative decrease in hardness of more than $50H_V$, or 15%, after over-aging for approximately 3,000 minutes, the Ti-5.0%Al-5%Zr-1%Si shows no drop after 100,000 minutes. This result is supported by studies that show that aluminum addition in titanium alloys containing silicon delays the precipitation of silicides, which is also apparent in figure 3-10 as the hardness curves slightly shifts to the right between the 0% and 5.0% aluminum content. The alloys containing 1.0% and 2.9% aluminum also show strong evidence that the addition of aluminum retards the formation of silicides, however,

the change in shape of the curves appears to be indicative of the formation of precipitates other than the ones previously discussed. One possible answer could be the formation of the aluminides, however, the author states that the alloys shows no evidence of Ti_3Al formation and the aluminum concentration in the alloys are also too low to form Ti_3Al, as discussed in the previous section.

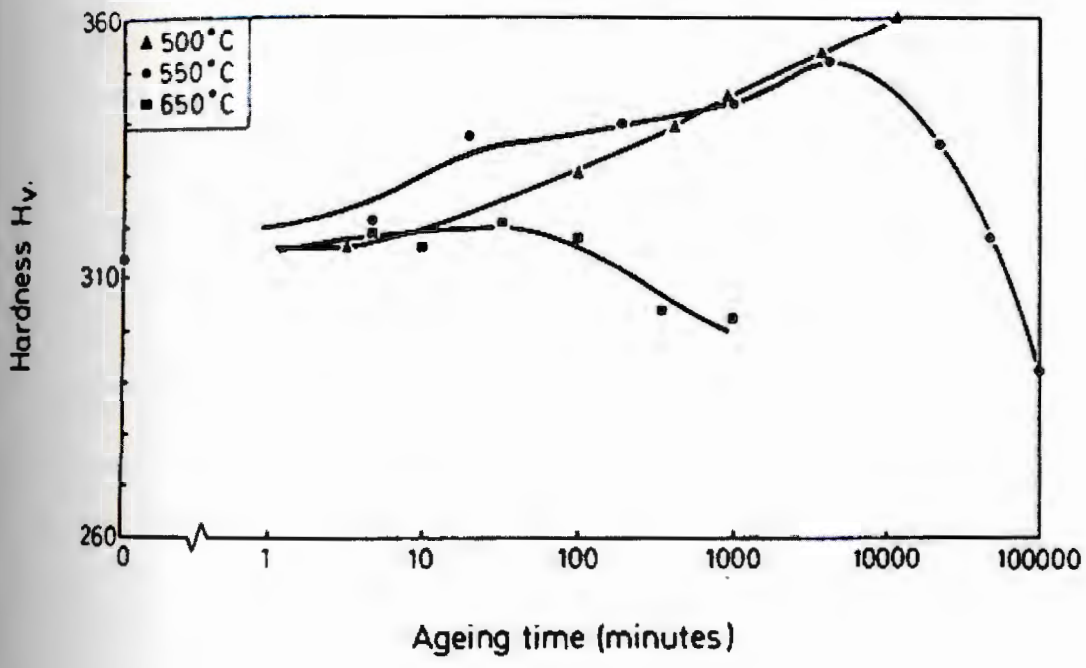

Figure 3-7: Effects of temperature on the aging characteristics of Ti-5%Zr-1%Si (from reference [45]).

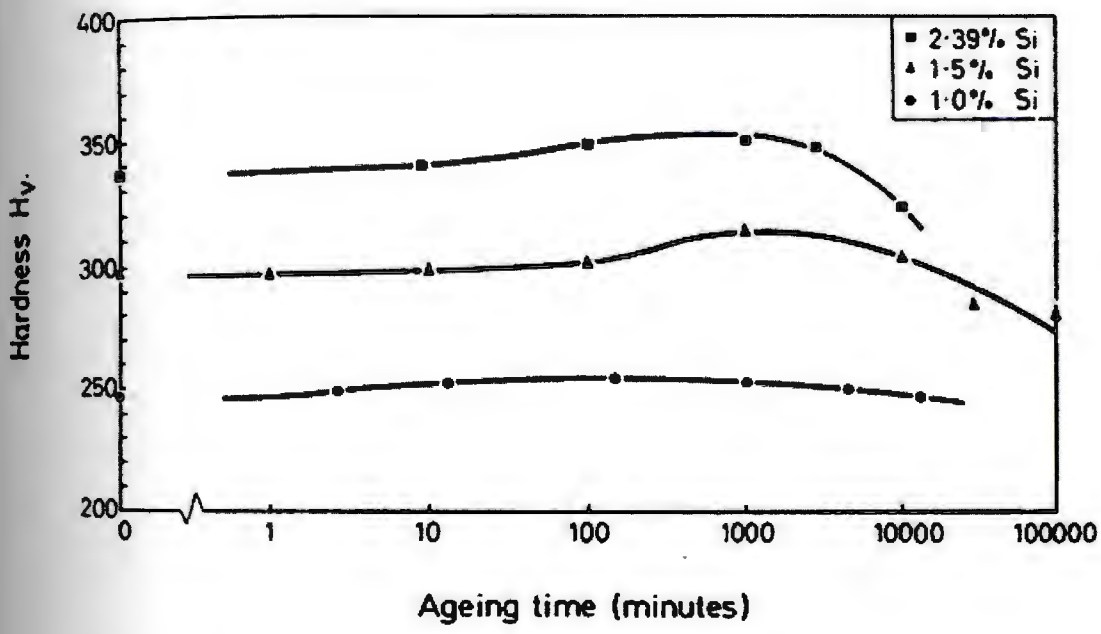

Figure 3-8: Effects of silicon content on the aging characteristics of binary Ti-Si alloys at 550°C (from reference [45]).

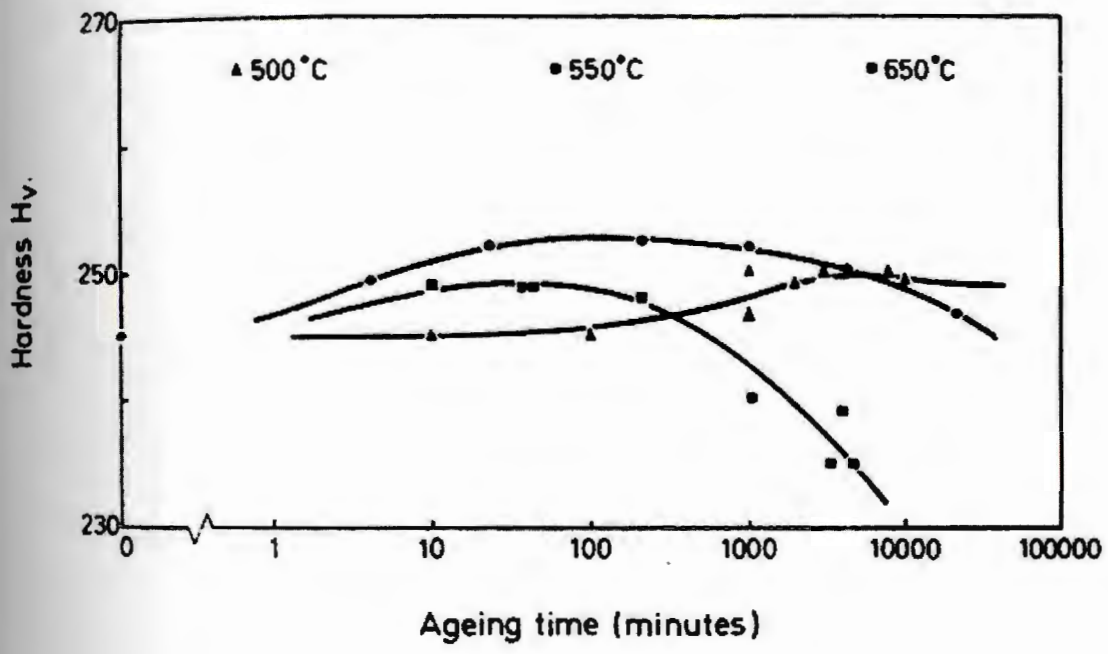

Figure 3-9: Effects of temperature on the aging characteristics of Ti-1%Si (from reference [45]).

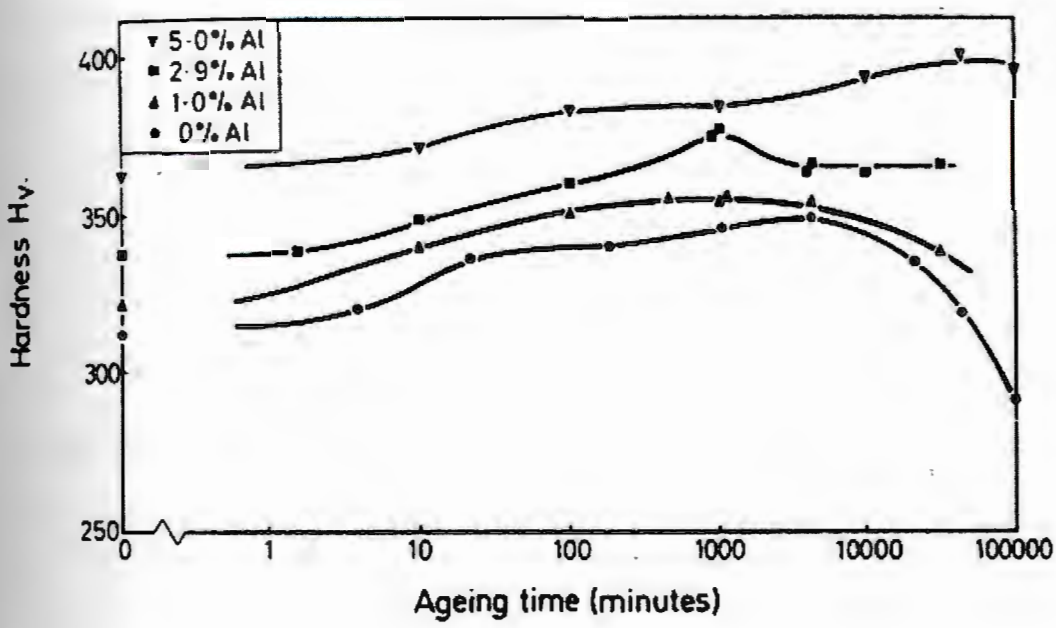

Figure 3-10: Effects of aluminum content on the aging characteristics of the quaternary Ti-5%Zr-1%Si-Al alloy at 550°C (from reference [45]).

Other studies on the effects of aging on the mechanical behavior of the near-alpha alloy Ti-1100 carried out by Madsen and Ghonem [47, 49] show the effect of aging at 593°C on the hardness of Ti-1100, see Fig. 3-11. The unaged condition shown in this figure corresponds to Ti-1100 heat treated above the β-transus and air-cooled, followed by an 8-hour aging at 593°C (stabilization). Although the chemical composition of Ti-1100 is more complex than the previously analyzed Ti-5%Al-5%Zr-1%Si (figure 3-10), the two plots show prominent similarities. Both tests show two hardness peaks, with the second peak at a higher hardness value than the first. Although the aging times differ from each other, the aluminum, zirconium and silicon concentrations can easily cause changes in the precipitation time and temperature. In addition, at the aging temperature range employed by the above mentioned authors, it is shown that both S_1 and S_2 type silicides are coexistent (see formation of silicides by over-aging section in chapter 3) as indicated in figure 3-10. Because the authors show the effects of aging on Ti-1100 after an initial stabilization treatment, precipitation of Ti_3Al may have already reached its critical size and a hardness peak associated to it may not be seen. Studies by Zhang et al [40] show the presence of aluminides after heat-treating Ti-6-22-22 in the β-phase field followed by aging at 540°C, as discussed in the aluminides section of this chapter. Therefore, it appears that in the results given by Madsen and Ghonem, aging of Ti-1100 results in the precipitation of S_1 and S_2 type silicides after 800 and 10,000 minutes, respectively.

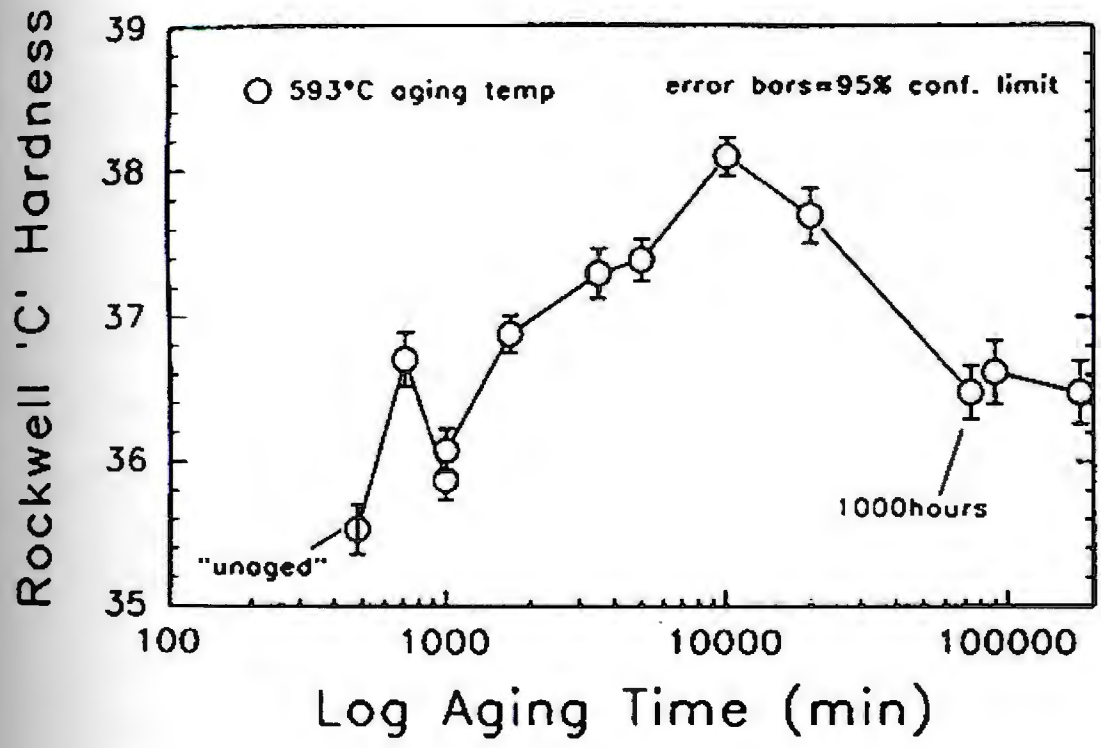

Figure 3-11: Effects of aging on air-cooled Ti-1100 heat treated at 1093°C and "stabilized" at 593°C for 8-hours (from ref. [49]).

3.1.4 Summary on the Role of Aluminide and Silicide Formation in Titanium Alloys

Aluminum, zirconium and silicon bearing titanium alloys show defined aging responses to changes in alloy element concentration, temperature and time of exposure. It was shown that in the binary Ti-Si system, only Ti_5Si_3 silicides were formed when aging at 500°C, 550°C and 650°C. However, additions of zirconium to the Ti-1%Si alloy precipitate S_1 and S_2 type silicides when aging at 550°C and S2 type silicides only at 650°C. Furthermore, retardation of silicide precipitation by aluminum occurred with increasing aluminum content when aging Ti-5%Zr-1%Si-Al alloy at 650°C. In the near-alpha titanium alloy Ti-1100, aging results following heat treatment in the β-phase field and stabilization at 593°C for 8-hours, show two hardness peaks that appear to be caused by reaching the critical particle size of S_1 and S_2 type silicides.

3.2 Significance of Over-Aging on IMI 834 at 650°C

A major concern when studying the mechanical properties of near-α alloys is the effect of long-term exposure at high temperatures. As discussed in the previous section, in this class of alloys, over-aging at high temperature promotes the precipitation of additional phases due to the high content of aluminum and silicon. In the present study, this effect is investigated in water-quenched IMI 834 with 5%, 23% and 39% volume fractions of α_p for long-term exposure at 650°C. This material was selected because, as discussed in chapter 2, its microstructure consists of primary alpha grains and fine platelets of martensite [23, 38]. By

forming a martensite phase instead of α/β lamellar colonies, silicide precipitation is expected to occur primarily at the boundaries between primary alpha and martensite [23, 38]. Consequently, any effects due to silicide precipitation on the fatigue crack-growth mechanisms that will be studied in chapter 4 can be identified. Alpha primary volume fractions of 5%, 23% and 39% were selected because they represent the highest changes in global hardness seen in chapter 2. The over-aging temperature was chosen based on studies by Maier et al [28] that show that the themomechanical fatigue behavior of IMI 834 changes at 600°C. By over-aging at a higher temperature, the structural stability of IMI 834 can be accessed in the region where one themomechanical fatigue behavior is predominant. Following, experimental procedures and results are discussed.

3.2.1 Experimental Procedure

Water-quenched IMI 834 specimens with 5%, 23% and 39% volume fractions of α_p, following heat treatment and aging at 700°C for 2-hours as described in chapter 2, were used in this test. These specimens (hereafter "aged" material) were then measured for α_p volume fraction and colony size using the same method described in chapter 2 and the results were compared to ensure a good agreement with previously tested data. Prior to over-aging, hardness measurements were made on the three different aged microstructures. As in chapter 2, all hardness results reported are the average of a minimum of twenty-five tests. Over-aging was done at 650°C, see figure 3-12. Hardness measurements of specimens over-aged and corresponding over-aging times are also plotted.

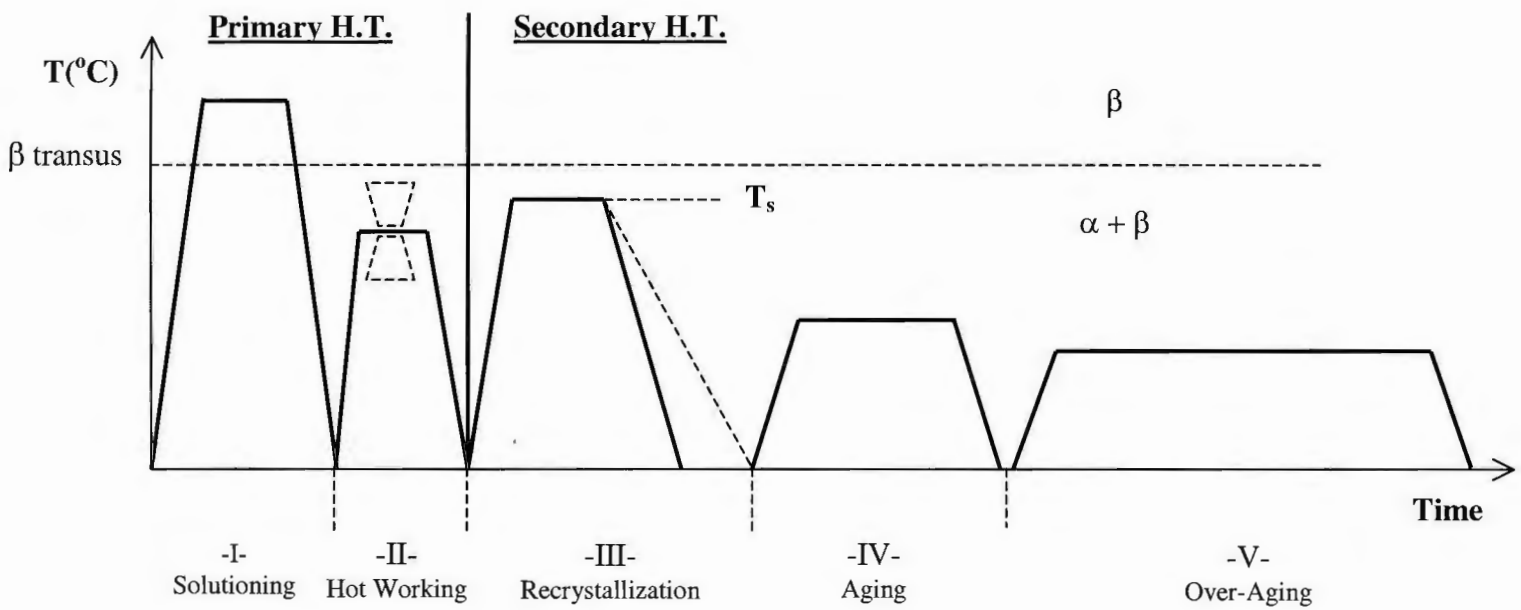

Figure 3-12: Thermal cycle applied in duplex microstructures showing over-aging process.

3.2.2 Results and Analysis

Heat treatment and aging described in the experimental procedure resulted in specimens with α_p volume fractions of 5%, 23% and 39%. Hardness measurements of aged and over-aged specimens were plotted as a function of time as seen in figure 3-13. This figure shows one hardness peak for each microstructure. Peaks of the 23% and 39% α_p volume fraction occur after similar over-aging periods, around 2,000 minutes. For the 5% α_p volume fraction a peak shows at about 80 minutes of over-aging. Hardness between the aged condition and the peak for the 5%, 23% and 39% α_p volume fractions increase by 3 R_C, 2 R_C, and 1.5 R_C, respectively.

The results shown in figure 3-13, particularly the presence of a single hardness peak, are in agreement with those reported in the studies discussed in the previous sections of this chapter. Over-aging at 650°C precipitates S_2 type silicides only. This is due to the fact that 650°C is a much higher temperature than that at which S_1 and S_2 type silicides have been reported to coexist in IMI 834. Additionally, Ti_3Al particles in IMI 834 reach stability after aging for 2-hours at 700°C, as previously discussed. This means that no hardness peak was expected in the over-aging plot resultant from critical aluminide precipitation. Based on these facts, it can be concluded that the peaks shown in Fig. 3-13 are due to S_2 type silicide precipitates reaching critical size.

Differences in the time it took to reach silicide critical size and changes in hardness of the three microstructures during over-aging, shown in Fig. 3-13, may

be explained as follows. Recalling the results obtained in chapter 2, it was shown that element partitioning increases primarily with α_p volume fractions greater than 30%, figure 2-24. In addition, the colony size decreases with α_p for volume fractions lower than 20%, figure 2-18. Silicide precipitation, discussed earlier in this chapter, generally occurs at the martensite boundaries between the α/β colonies and the primary alpha grains. The size of these precipitates changes with aging temperature (see figure 3-3), α_p volume fraction (figure 3-2), as well as with aluminum concentration (figure 3-10). In this analysis, temperature will not be a factor since all three microstructures were over-aged at 650°C. Additionally, as shown in figure 3-3, over-aging between 625°C and 700°C does not change the size of the silicide precipitates. However, an increase in the concentration of aluminum in the primary alpha grains due to element partitioning may lead to a retardation effect on the precipitation of silicides. The increase in volume fraction of α_p also causes a size increase on the silicide precipitates, as shown in figure 3-2. In comparing the results for the over-aged 5%, 23% and 39% α_p volume fractions, three observations can be made:

1. In the materials with 23% and 39% α_p volume fractions, colony sizes are similar; measuring about 30 μm. For the 5% α_p vf, colony size is approximately five times larger, measuring 150 μm. (see Fig. 2-18).
2. Due to element partitioning, in the 23% and 39% vf, α_p is expected to contain greater amounts of aluminum compared to the 5% (see figure 2-24).

3. Silicide precipitates are considerably smaller for the 5% vf microstructure compared to the other two microstructures. For the material with 23% vf, the silicide precipitates are also smaller than the 39%.

Based on these observations, the time it took silicides to reach critical size for the three microstructures can be explained in terms of a combination of the α_p aluminum content and colony size. Due to the higher α_p aluminum content in the higher volume fraction microstructures, it is possible that the retardation effects described in Fig. 3-10 can explain the differences in the critical silicide precipitation over-aging time. Indeed, for the 23% and 39% α_p microstructures, silicide critical size occurred at approximately the same over-aging time of 2,000 minutes, whereas critical silicide particle size for the 5% α_p is achieved after only 80 minutes. The fact that critical silicide size is achieved at nearly the same time for the 23% and 39% α_p vf is not very clear in terms of the aluminum concentration, but it can be explained in terms of colony size. As previously discussed, silicides precipitate at the colony and α_p boundaries. In addition, this study showed in chapter 2 (Fig. 2-18) that colony size for volume fractions greater than about 23% α_p remains relatively constant. Based on these results, it may be concluded that silicide precipitation rate in the two microstructures would be similar. In addition, colony size can also explain the shorter over-aging time to reach silicide critical size for the 5% α_p vf. The much smaller colonies as well as the smaller size of precipitates that form in this microstructure are strong reasons to

believe that silicide critical size is achieved earlier compared to the other two microstructures.

Changes in the hardness from the aged condition to the maximum over-aged peak can be explained in terms of silicide size. As shown in figure 3-2, silicides increase with increased α_p vf. Material global hardness should decrease with increasing silicide size due to the incoherency of the particles on the boundaries between colonies and α_p particles. Consequently, differences between the aged and maximum over-aged material hardness should increase with decreasing α_p volume fraction, as silicides decrease in size. In fact, increases in hardness of 1.5 R_C, 2 R_C and 3 R_C can be seen for the 39%, 23%, and 5% α_p volume fractions (Fig. 3-13).

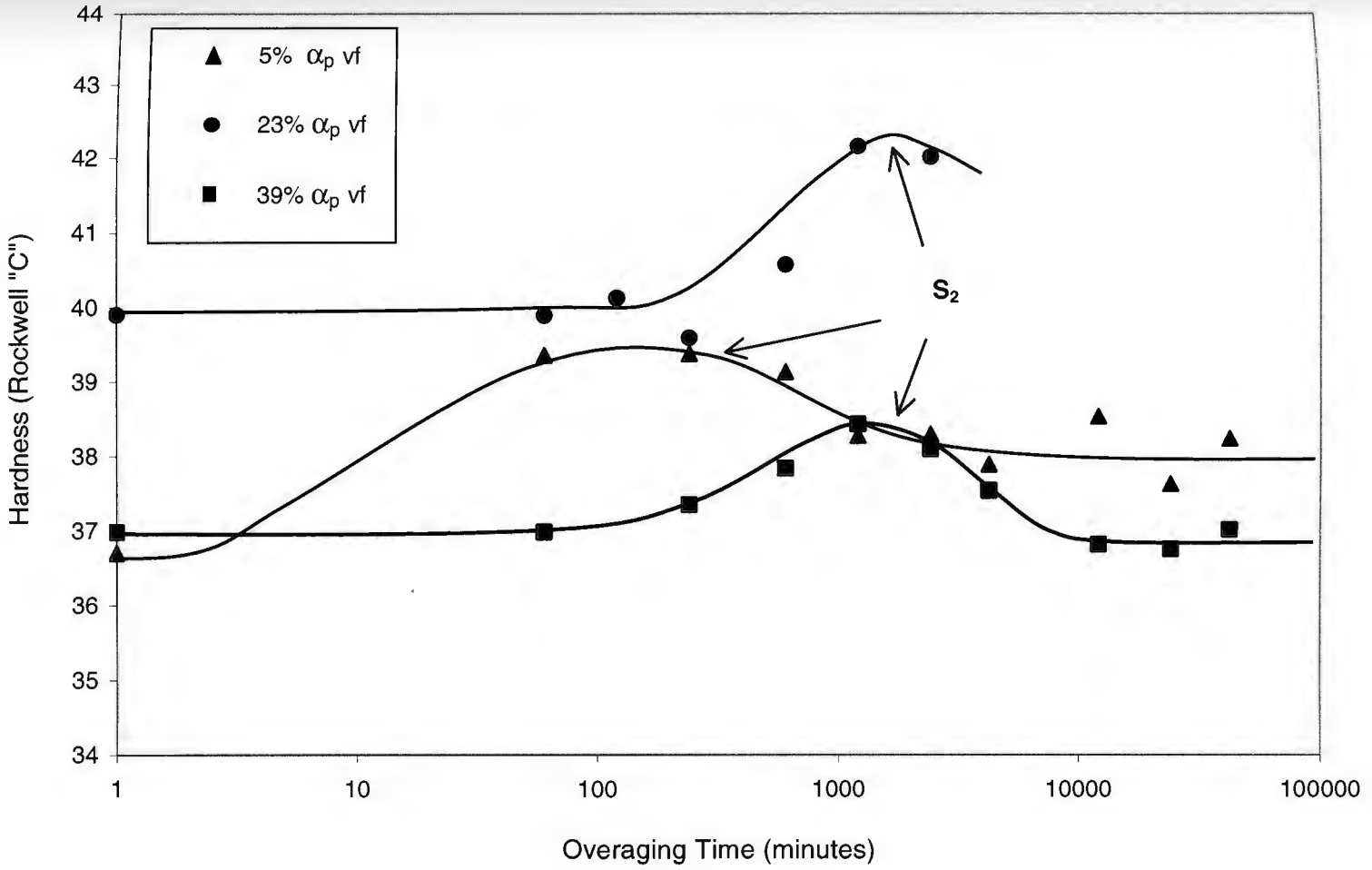

Figure 3-13: Effect of over-aging on hardness R_C for water-quenched and aged 5%, 23%, and 39% α_p vf IMI 834.

3.3 Summary and Conclusions for Chapter 3

The effects of long-term exposure at elevated temperature on the structural stability of titanium alloys have been discussed in this chapter. Also, a detailed description was given on the formation of aluminides and silicides when titanium alloys are over-aged. Furthermore, significant material mechanical property changes when over-aging due to aluminide and silicide precipitation was discussed. Finally, over-aging at 650°C was performed on the titanium alloy IMI 834 with three different microstructures and the results were analyzed in terms of hardness changes with over-aging time. The following conclusions can be derived from this chapter:

1. α_2-phase precipitates in the α-phase.
2. Addition of α-stabilizers, especially oxygen, increases α_2 precipitation and shifts the $\alpha \rightarrow \alpha + \alpha_2$ transition temperature in titanium alloys with lower aluminum content.
3. When aging IMI 834 at 700°C, α_2 particles reach critical size within 2-hour.
4. In IMI 834, aging below 600°C precipitates α_2 in the α_p regions only. At 700°C, α_2 precipitates in both the α_p and α' phases.
5. In Ti-Si-Zr alloys, S_1 and S_2 type incoherent silicides coexist at the lower precipitation temperatures. In the upper temperature range, 600°C-1050°C, (depending on the alloy chemical composition) only S_2 type silicides are found.

6. In lamellar microstructures, silicides form on α' platelet boundaries, whereas in duplex microstructures, silicides form on α' platelet boundaries and martensite boundaries of α_p and α/β colonies.

7. Silicides increase in size with decreasing recrystalization temperature (increase α_p volume fraction).

8. When aged, silicides increase in size with increase in temperature. They also change from ellipsoid to circular with increasing aging temperature.

9. Over-aging of IMI 834 at 650°C precipitates S_2 type silicides only.

10. In IMI 834, critical silicide particle size for both 23% and 39% α_p volume fractions occurs after approximately 2,000 minutes of over-aging at 650°C. Under the same conditions, for the 5% α_p vf, silicide critical size is achieved in only 80 minutes.

11. For IMI 834, hardness values between the aged and over-aged peak for the 5%, 23% and 39% α_p microstructures is 3 R_C, 2 R_C and 1.5 R_C, respectively.

Chapter 4: Fatigue Crack Growth of IMI 834 at 650°C

Introduction:

This chapter explores the role of microstructure and loading frequency on the fatigue crack growth behavior IMI 834 at 650°C. Chapter 2 of this thesis investigated the effects of the recrystalization and aging processes on the phase morphology of IMI 834 as well as the influence of heat treatment on the hardness characteristics of the material. Results showed that at recrystalization temperatures above 1010°C, the resulting α_p volume fraction is independent of the cooling rate. Additionally, it was shown that colony size decreased with increasing volume fraction up to 20%. For higher α_p volume fractions, the colony size remains relatively constant. The hardness results showed that between approximately 10% and 30% α_p volume fractions, the material hardness has a constant value in each cooling condition. On the other hand, the hardness decreased significantly for volume fractions lower than 10% and for volume fractions higher than 30%. It was also found that element partitioning effects are most dominant in volume fractions above 30%.

Based on these results, microstructures with 5%, 23% and 39% α_p volume fraction were prepared to study the role of over-aging at 650°C in IMI 834. Each of the volume fractions corresponds to regions where colony size effect, no effect, and partitioning element effect, respectively, were predominant. Analysis aluminide and silicide precipitation in titanium alloys indicated that during over-aging, only S_2 type silicides precipitated. Furthermore, results showed that critical silicide size

was achieved at the same over-aging period, 2,000 minutes, for α_p volume fraction greater than 23%. On the other hand, over-aging the material with 5% α_p volume fraction resulted in precipitation of S_2 type silicides in a shorter time, 80 minutes, and in a significant increase of hardness as compared to the other two volume fractions.

In the present chapter, the role of microstructure and loading frequency on the fatigue crack growth of the near-α titanium alloy IMI 834 is studied at 650°C for α_p volume fractions of 20% and 30% α_p. Based on the results from chapters 2 and 3, microstructures with 20% and 30% α_p volume fraction support the following particulars:

1. For the same recrystalization temperature, the morphology of the two microstructures can be achieved independently of the cooling rate; in the present study, only water quenching will be imposed.
2. Colony sizes for the two microstructures are expected to be similar.
3. Little difference in the partitioning effect is expected.
4. When over-aged at 650°C, silicide critical size occurs at a similar time.
5. Silicide precipitates are expected to be smaller in the 20% α_p volume fraction than in the 30%.

Studies have shown that, in near-α Ti-1100, the high temperature fatigue crack growth rate is influenced by the interaction between creep and fatigue [47].

Furthermore, it has been shown that creep in near-α alloys is very sensitive to the precipitation of silicides [49]. Considering these results, it was important in the present study to have volume fractions that show similar aging effects. Since creep between the two selected microstructures is not dependent on the time of aging, the present investigation on the fatigue crack growth behavior of IMI 834 will only focus on the role of microstructure features.

This chapter is divided into four sections. The first section describes the heat treatment process used to obtain the two selected microstructures as well as the specimen preparation and geometry. Procedures for fatigue crack growth tests will also be presented. The second section deals with the experimental results. The effects of loading frequency and hold time on the fatigue crack growth rate will be investigated and discussed with the support of SEM examinations in the third section. The chapter concludes with a summary of the test results.

4.1 Experimental Procedure

The material used in this study is the same as that presented in the previous chapters. The chemical composition and morphology of as-received are given in chapter 2. Using figure 2-17, recrystalization temperatures of 1015°C and 1030°C were selected to obtain α_p volume fractions of 20% and 30% respectively. Solutioning treatment of 3-inch long by 1¼-inch wide blocks of IMI 834 was done in the same manner detailed in the experimental procedure section of chapter 2. Specimens were water-quenched after solution treatment and air-cooled after aging

for 2-hours at 700°C. Surface layer removal of 1mm was performed on the IMI 834 blocks following heat treatment. Each block was cut into two compact tension (CT) test specimens with dimensions according to ASTM standard E 647-88 and designated as CT-12.5 (see figure 4-1). Mechanical polishing was performed using the same method described in the experimental procedure of chapter 2 to give the test specimens a flank surface finish of 1 μm. The specimens were etched in Kroll's reagent. All examinations were performed by SEM and optical microscopy. Alpha primary volume fraction measurements were performed with the same analysis described in chapter 2.

Fatigue crack growth (FCG) experiments were conducted on polished and etched Compact Tension (CT) specimens, CT 12.5 (B=0.25-inch and W=1-inch). The design of this specimen is given in Fig. 4-1. Room-temperature pre-cracking was performed at a loading frequency of 20 Hz to obtain an initial crack length of 0.3 W. The crack growth was monitored using optical measurements taken from the two sides of the test specimen. In addition, the crack growth was monitored using the Potential Drop (PD) method, as described in the ASTM Standard book. In this technique, a 3-Ampere current was imposed in the specimen through wires welded on the load train. The potential drop at the notch, V_1, was measured and compared to the reference V_2, as shown schematically in figure 4-1. The potential drop curve that relates V_1/V_2 to the crack length "a" was calibrated based on optical measurements. All FCG tests were conducted on a servo-hydraulic material testing system controlled by the Test Star IIS computer environment shown in figure 4-2. Heating of the specimens was achieved using a clamshell furnace in which the

specimen temperature is controlled by two thermocouples spot-welded on the top and bottom sides of the specimen as shown in figure 4-3. Temperature variations in all tests were maintained within less than 5°C along the specimen height. The testing temperature was 650°C. The crack mouth opening displacements (CMOD) were measured using a high temperature clip gauge, see Fig. 4-3. These data were used to determine the crack opening level during the test by means of the compliance method. Tests were performed with a constant load ratio R equal to 0.1. Two loading frequencies; 10 Hz and 0.05 Hz, were applied to the test specimens. In addition, a third load cycle, consisting of 0.05 Hz with a 300-second hold time imposed at peak stress level of the loading cycle was also applied. Scanning Electron Microscopy was used to examine the fracture surface and crack path of selected specimens. Fracture surface and crack path images were collected and observed for analysis.

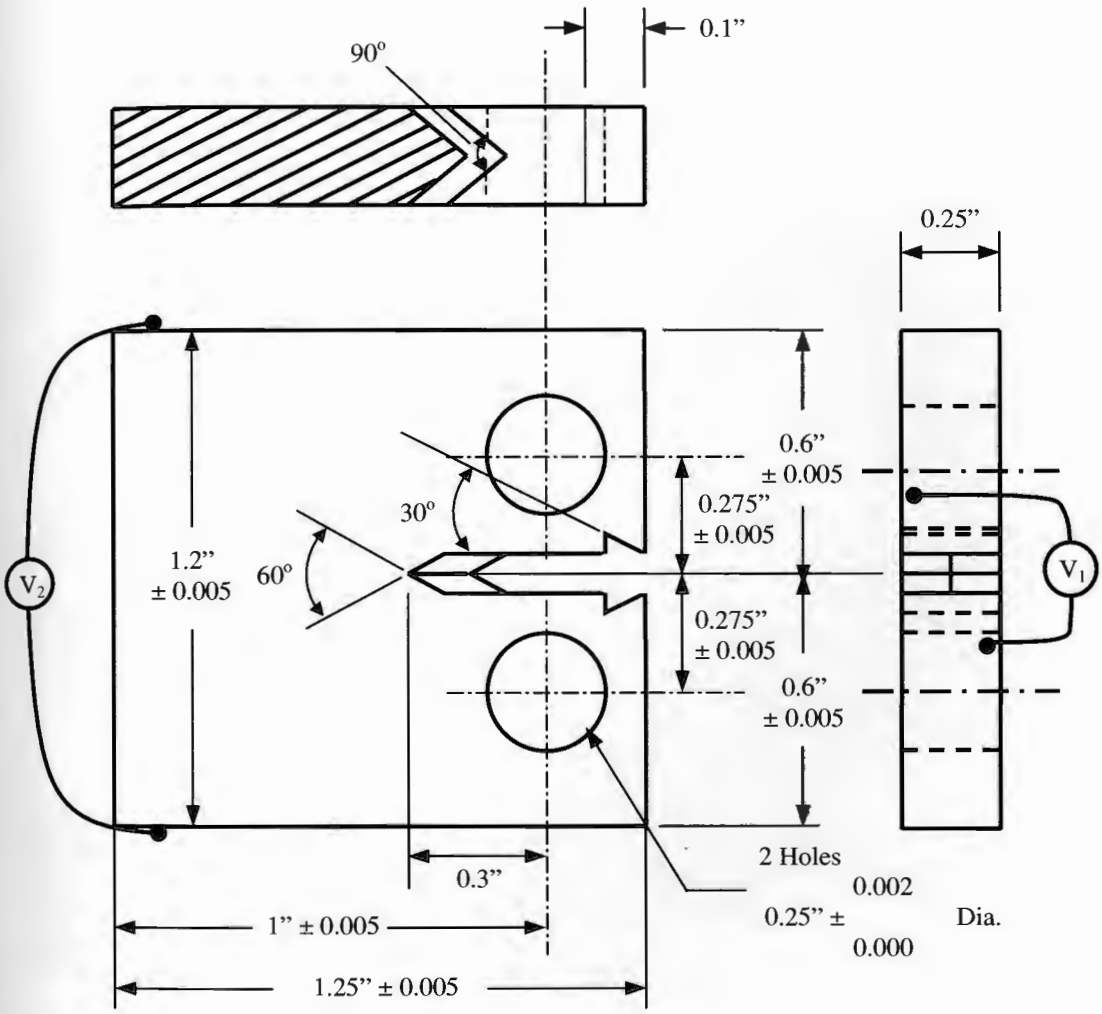

Figure 4-1: Specimen geometry for fatigue crack growth testing (CT 12.5) and location of potential drop wires. V1 represents the potential drop across the crack mouth and V2 is the potential drop reference away from the crack. A pulsed 3 Amp current traverses this specimen. through the load train, as shown in Fig. 4-3.

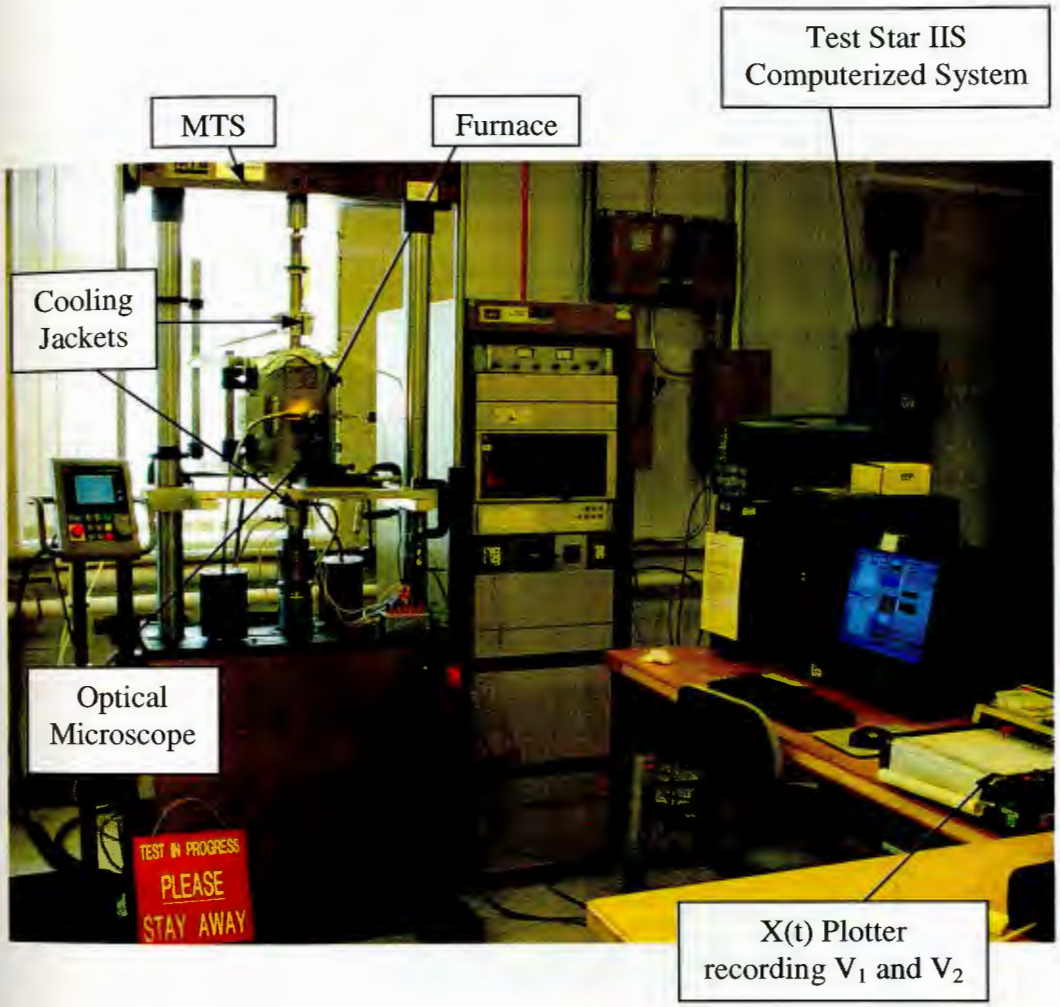

Figure 4-2: MTS servo-hydraulic material testing system with clamshell furnace controlled by the Test Star IIS computer environment.

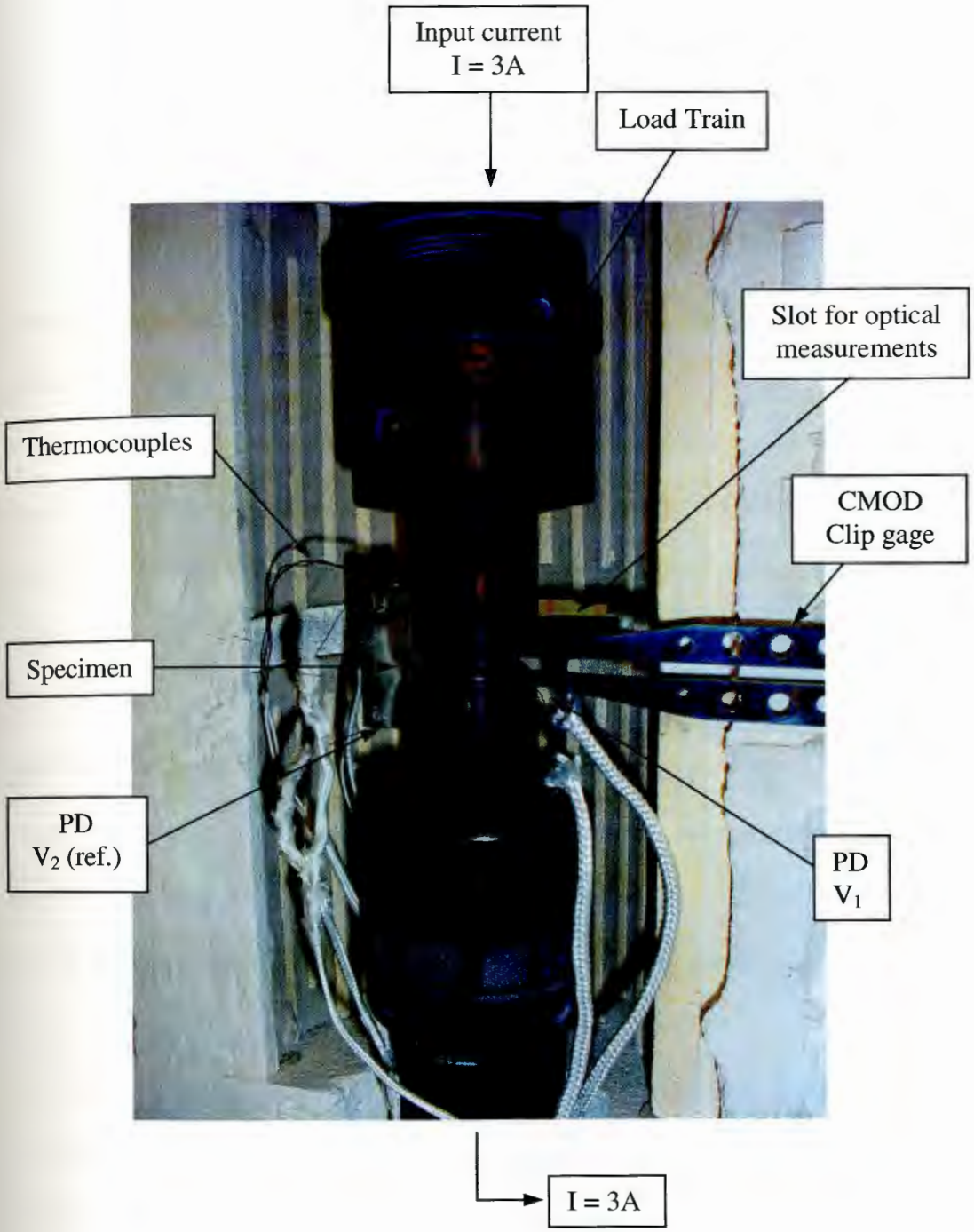

Figure 4-3: Clamshell furnace and loaded specimen with spot-welded thermocouples and Potential Drop (PD) wires.

4.2 Experimental Results

The microstructures resulting from the heat treatment procedure are shown in the micrographs represented in figures 4-4 and 4-5. The volume fractions on these microstructures were determined to be equal to 20% and 30%. Note also that the colony size between the two microstructures is not similar, contrary to expected based on chapter 2 results (Fig. 2-18). The slight difference could be explained by the fact that different IMI 834 pancakes were used in the FCGR tests. Table 4-1 lists the resulting microstructures and the corresponding loading frequencies applied to the specimens.

Figures 4-6 illustrates the fatigue crack growth rates for IMI 834 with 20% and 30% α_p volume fractions tested at 10 Hz and 10s-10s loading frequencies. Specimens tested at 10 Hz show lower FCGR than those tested at 10s-10s. Furthermore, changes in microstructure appear to have no significant effect on the FCGR at these loading frequencies. Figure 4-6 also shows the result of a 300s hold time on the 10s-10s loading frequency, designated as 10s-300s-10s. In addition to a crack growth rate increase in the specimens tested with a hold time, the two microstructures demonstrate a prominent crack growth rate difference, with the 30% α_p microstructure having the highest crack growth rate. Detailed analysis of these figures is done in the next section.

The fracture surfaces of tested specimens were also subjected to both optical and scanning electron microscopy. Figures 4-7 and 4-8 show the fracture

morphology corresponding to test conditions 10 Hz and 0.003 Hz for the 20% and 30% α_p microstructures, respectively. Figures 4-7(a) and 4-8(a) show a relatively flat morphology compared to that of figures 4-7(b) and 4-8(b).

The fracture path of specimens tested at 0.05 Hz for the 20% and 30% α_p volume fractions are shown in figure 4-9. Transgranular fracture in both colony and primary alpha particles is apparent in the both microstructures.

Figure 4-10 is the fracture surface of a specimen with 20% α_p vf showing the transition between test conditions 10s-10s and 10s-300s-10s as well as 10s-300s-10s and failure.

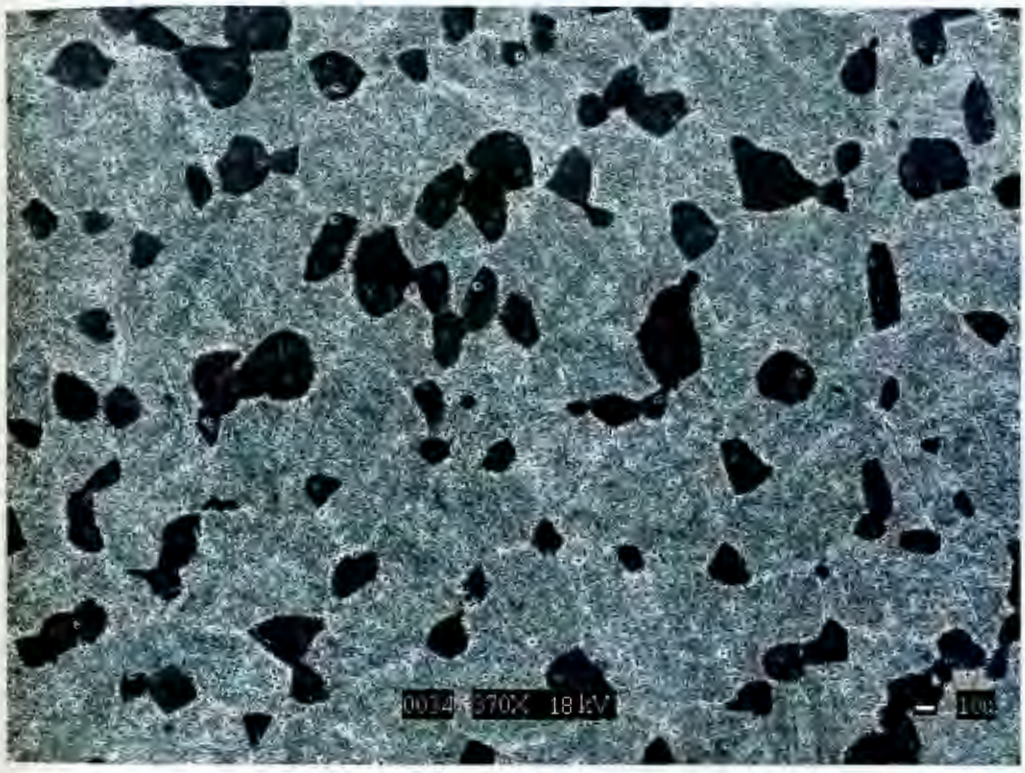

Figure 4-4: IMI 834 solution treated at 1035°C for 2-hours and water-quenched followed by aging at 700°C for 2-hours (20% α_p vf).

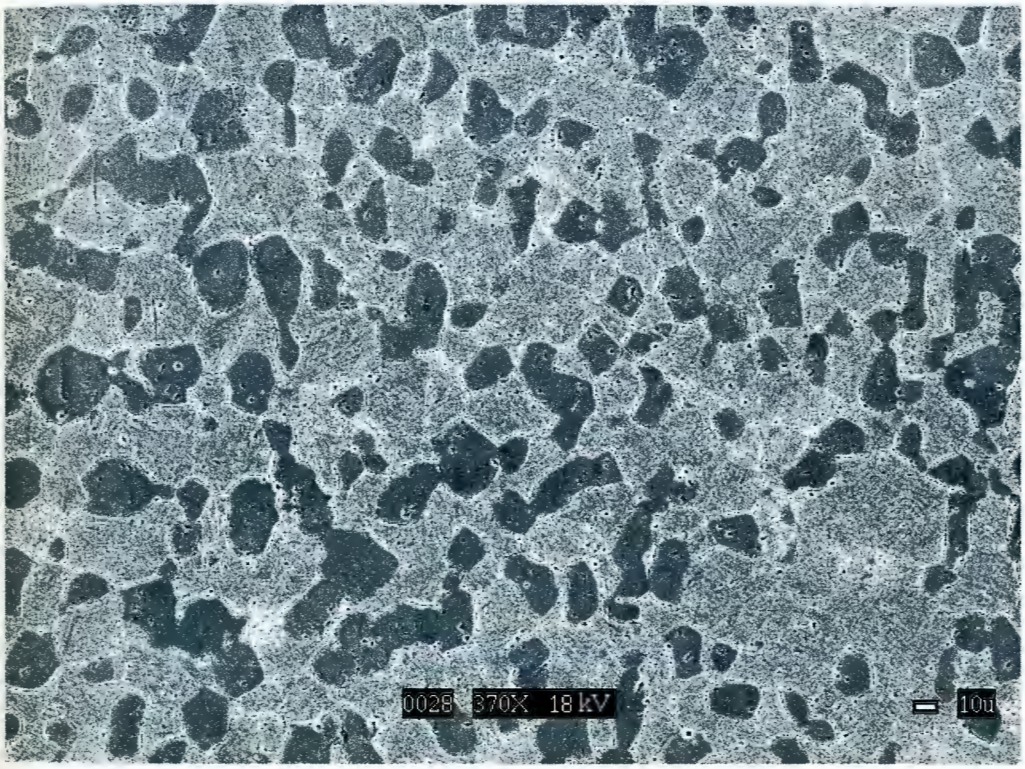

Figure 4-5: IMI 834 solution treated at 1010°C for 2-hours and water-quenched followed by aging at 700°C for 2-hours (30% α_p vf).

No.	Specimen	Microstructure ($\alpha_{p\%}$)	Applied Cycle
1	B2	20%	10s-10s
2	A1	30%	10s-10s
3	A2	30%	10 Hz
4	B3	20%	10 Hz
5	A2	30%	10s-300s-10s
6	B3	20%	10s-300s-10s

Table 4-1: List of microstructures and corresponding loading frequencies for fatigue crack propagation testing of IMI 834 at 650°C.

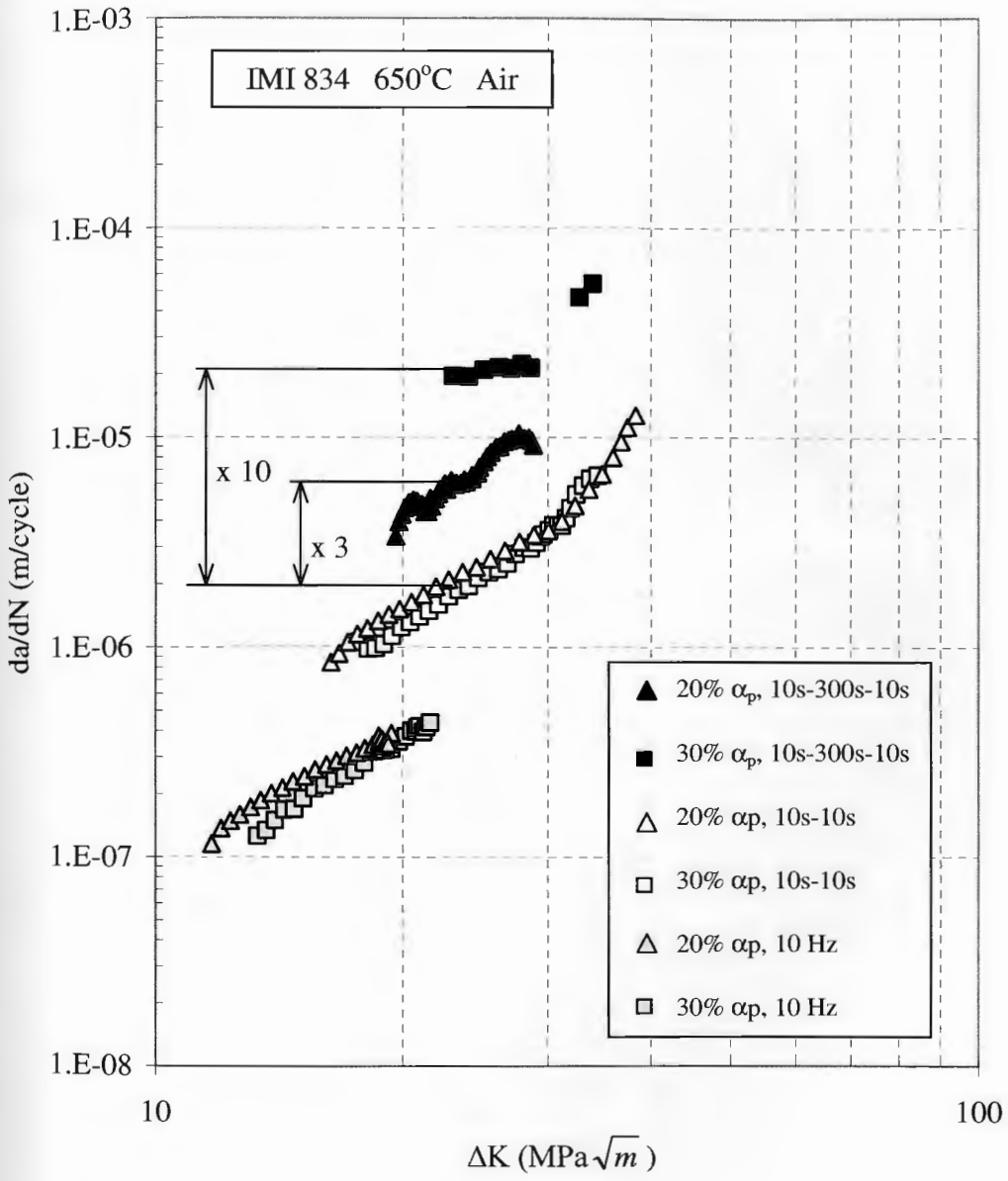

Figure 4-6: Effect of loading frequency and 5 minute hold time at peak stress on Fatigue Crack Growth Rate of IMI 834 at 650°C.

(a)

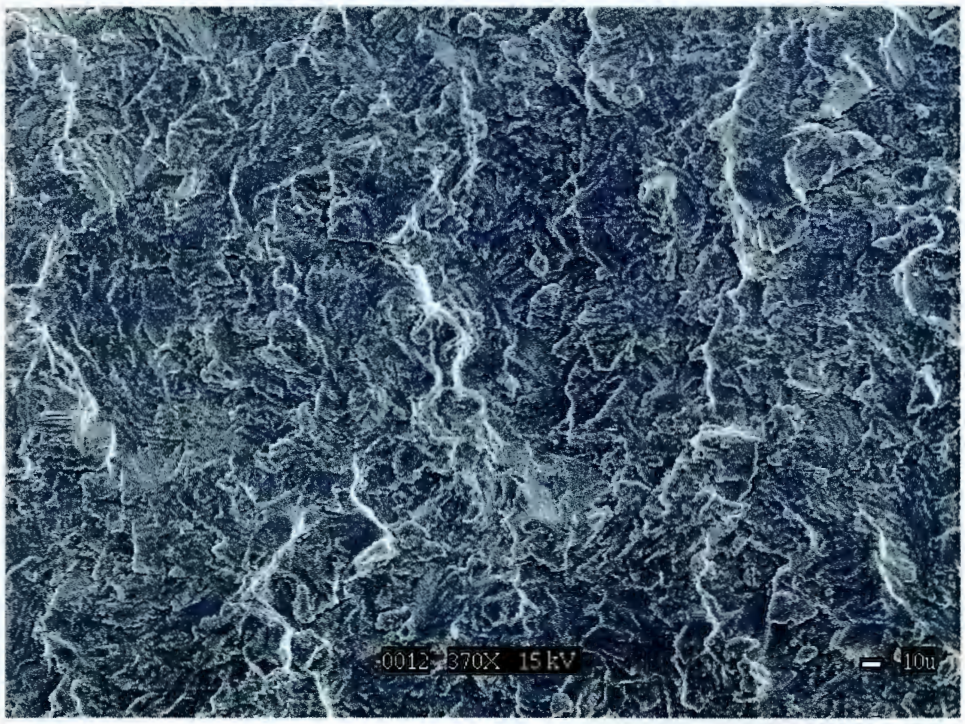

(b)

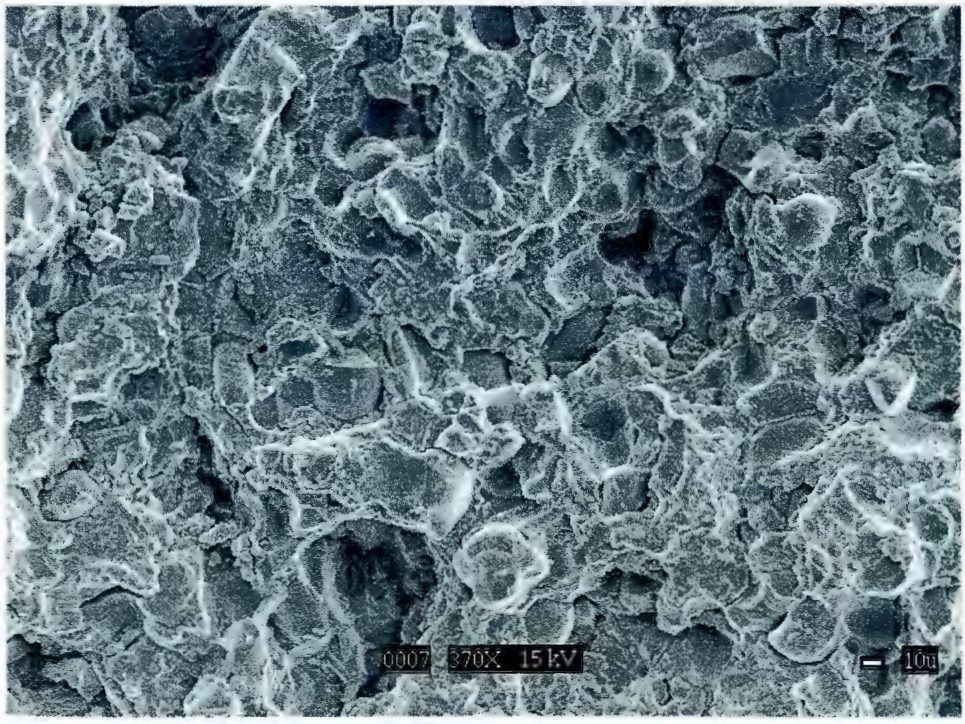

Figure 4-7: Fracture surface on the 20% α_p vf specimen for test conditions (a) 10 Hz (b) 0.003 Hz.

(a)

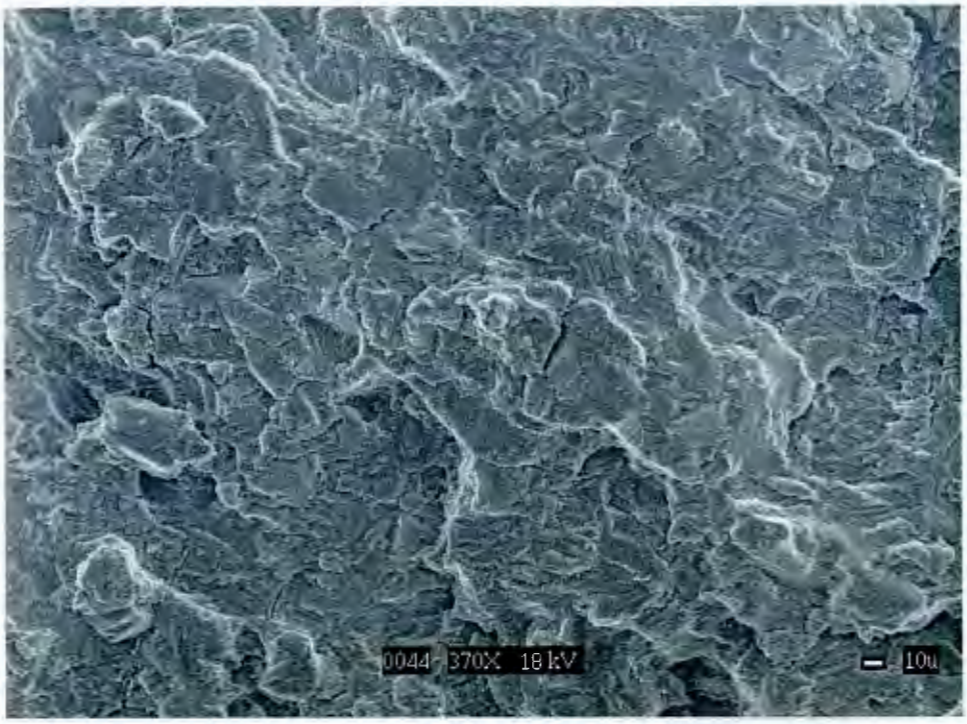

(b)

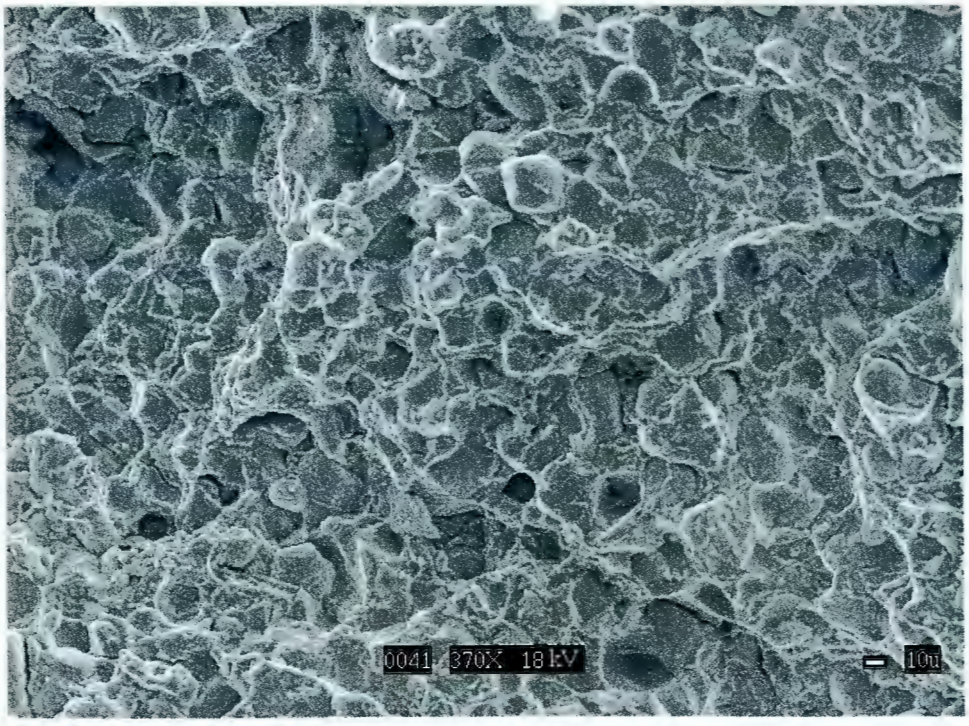

Figure 4-8: Fracture surface on the 30% α_p vf specimen for test conditions (a) 10 Hz (b) 0.003 Hz.

(a)

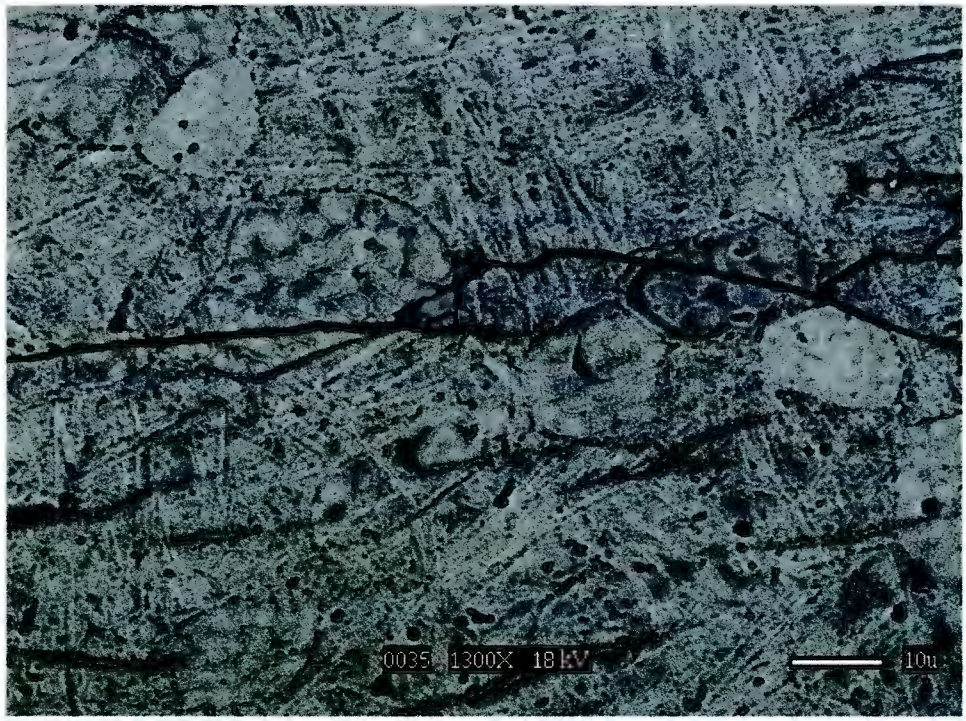

(b)

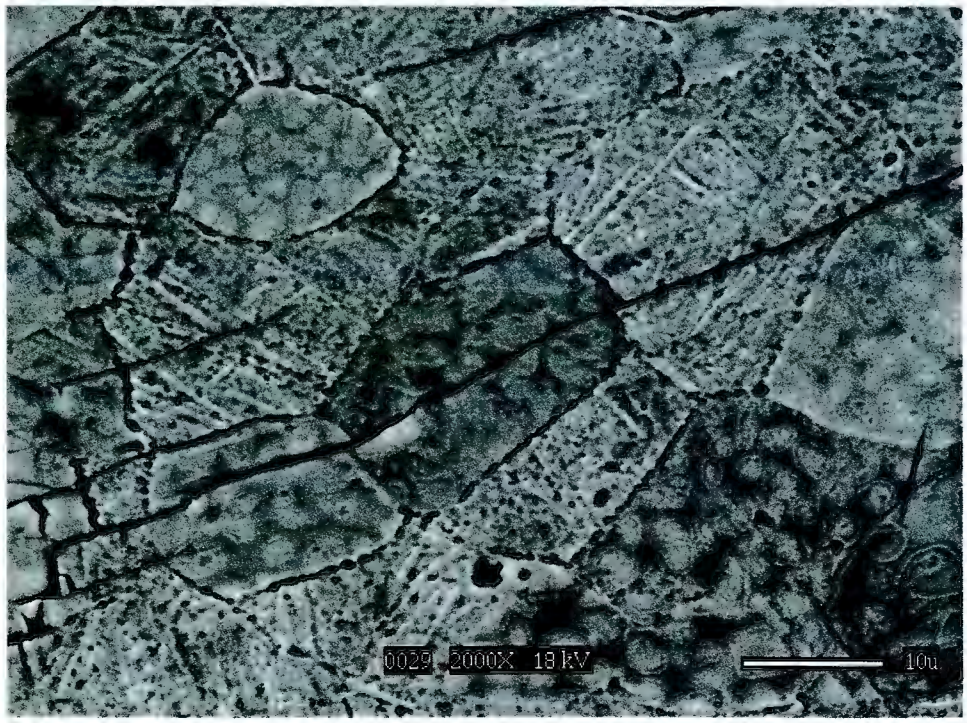

Figure 4-9: Fracture path for test conditions 0.05 Hz on the (a) 20% α_p vf specimen (b) 30% α_p vf specimen.

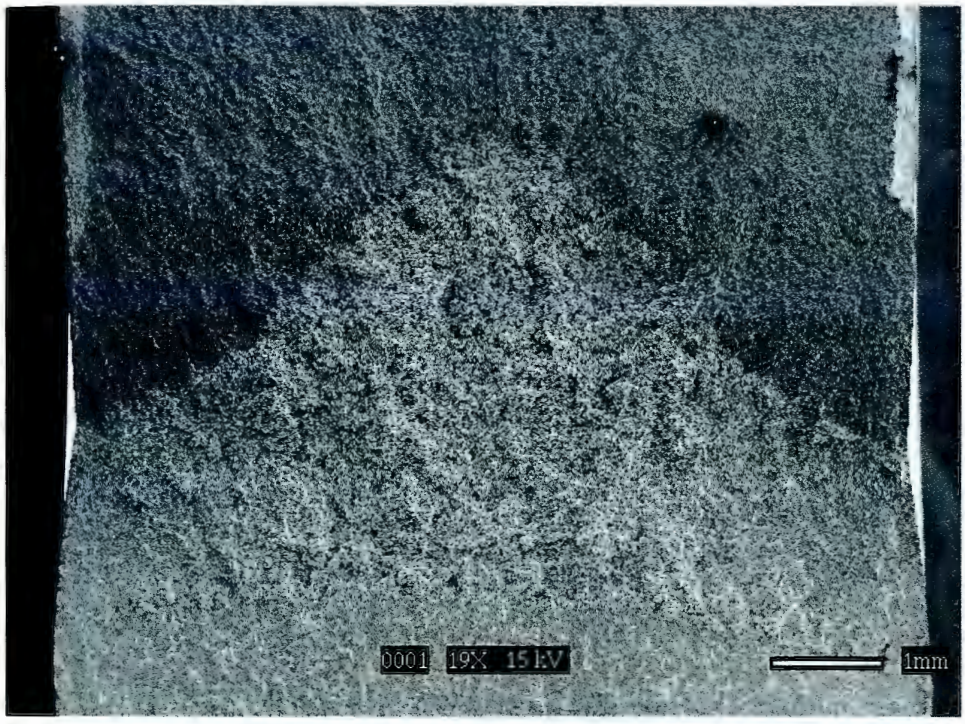

Figure 4-10: Fracture surface showing the transition between test conditions 0.05 Hz and 0.003 Hz as well as between 0.003 Hz and failure on the 20% α_p vf specimen.

4.3 Discussion

It is apparent in Fig. 4-6 that the FCGR in both 20% and 30% α_p vf are similar for the test conditions of 10 Hz and 0.05 Hz. The FCGR is shown higher for both microstructures as the loading frequency decreases. This increase could be due to effects of both environment and creep, since these effects are known to influence the crack growth rate in titanium alloys [62-64]. An increase in temperature, for example, eventually leads to faster intergranular crack growth rates as creep-fatigue interaction effects become evidence. At a given temperature, the creep contribution increases as mean stress increases (increase in R ratio) and as loading frequency decreases (i.e. more time at temperature). It is assumed that the increase in threshold ΔK with temperature is due to blunting of the crack tip via plastic and creep mechanisms. The material grain size is also greatly influenced by temperature, as well as hold time under load and material creep properties. For coarse-grained microstructures at lower temperatures, material tends to exhibit fatigue crack growth rates in the threshold region. Furthermore, this grain size effect tends to diminish with increasing temperature. For microstructures with finer grain size, the grain boundary area is larger, which usually promotes faster crack growth at elevated temperatures. The effect of environmental assisted (oxygen) damage on fatigue crack propagation in air at elevated temperatures tends to be intergranular and progress rapidly. In contrast, fatigue crack growth in vacuum tends to be transgranular and slower.

Analysis of Fig. 4-6 shows no direct evidence to support creep or environmental damage mechanisms based solely on the increase in crack growth rate with decrease in loading frequency results. Furthermore, the change in α_p vf appears to have little effect for test condition 10 Hz and 0.05 Hz, as the crack growth rates for the two microstructures are nearly superimposed. When the 300-second hold-time is added to the 0.05 Hz loading condition the FCGR difference is drastic. In addition to the increase in crack growth rate with decreasing loading frequency, the CGR for the two microstructures is remarkably distinct. For example, for the threshold of about 25 MPa$\sqrt{m}$, the crack growth for both microstructures tested at 0.05 Hz increased from CGR $2x10^{-6}$ m/cycle to $6x10^{-6}$ and $2x10^{-5}$ m/cycle for the 20% and 30% α_p vf, respectively. These results are in agreement with studies shown in figure 2-11 where, for the water-quenched IMI 834, an increase in α_p vf corresponds to an increase in plastic strain. These results indicate that in addition to the aforementioned creep effects, microstructure also plays a role in the fatigue crack growth of IMI 834 at 650°C.

SEM observations shown in figure 4-9 reveal that for the test condition 0.05 Hz, the crack path in both microstructures appears to be transgranular. In addition, examination of Fig. 4-7 (a) and 4-8 (a) for the 20% and 30% αp microstructures, respectively, shows that the fracture surface in both specimens exhibits a flat morphology, further pointing to a transgranular fracture mechanism in the higher lower frequencies. On the other hand, crack path observations of the specimens tested at 0.003 Hz showed predominantly intergranular mechanisms in the α_p

boundaries and transgranular in the α/β colonies. Furthermore, SEM imagery showed large craters on the fracture surface of both microstructures, where un-fractured α_p particles could be distinctively seen embedded, see Fig. 4-7 (b) and 4-8 (b). From these interpretations, two schematic representations that show possible crack paths in both α/β colony and primary alpha are presented in figures 4-11(a) and (b).

Based on the aforementioned observations, it can be assumed that for high frequency loading, pure fatigue dominates the FCGR behavior. The different strengths between the colonies and the α_p phase, seen in Fig. 2-21, can further account for the changes in fracture growth rates. At the higher loading frequencies, fatigue crack growth mechanism is transgranular in α_p particles due to the lower strength of this phase compared to that of the martensite boundaries. For the higher α_p volume fraction, the slightly lower crack growth rates in the transgranular fracture region indicate that higher volume fractions are more crack resistant compared to the lower ones. This effect can be the result of a higher α_p density and/or size.

Contrary to the fracture mode seen in the higher loading frequencies, creep dominates the FCGR response for low frequency loading. For these lower loading frequencies, the tougher material, α_p, allows for higher plastic strain without failing, as the particles have the ability to absorb energy. In this case, failure ought to occur, possibly by fast fracture due to stress built up, at the martensite boundaries of α_p particles. In addition, the presence of incoherent hard silicide

precipitates further supports the mechanism of boundary fast fracture, also know as zipping effect. As previously discussed, silicide precipitates grow larger with increasing α_p volume fraction. As a result, α_p boundaries weaken due to increasing silicide size and incoherency. Results in Fig. 4-6 reflect this behavior, as the FCGR for the 30% αp vf is much higher than that of the 20% for the 0.003 Hz loading frequency.

Similar results to those obtained from the FCGR tests in this thesis were obtained when the loading frequency was maintained constant and the operating temperature increased [26].

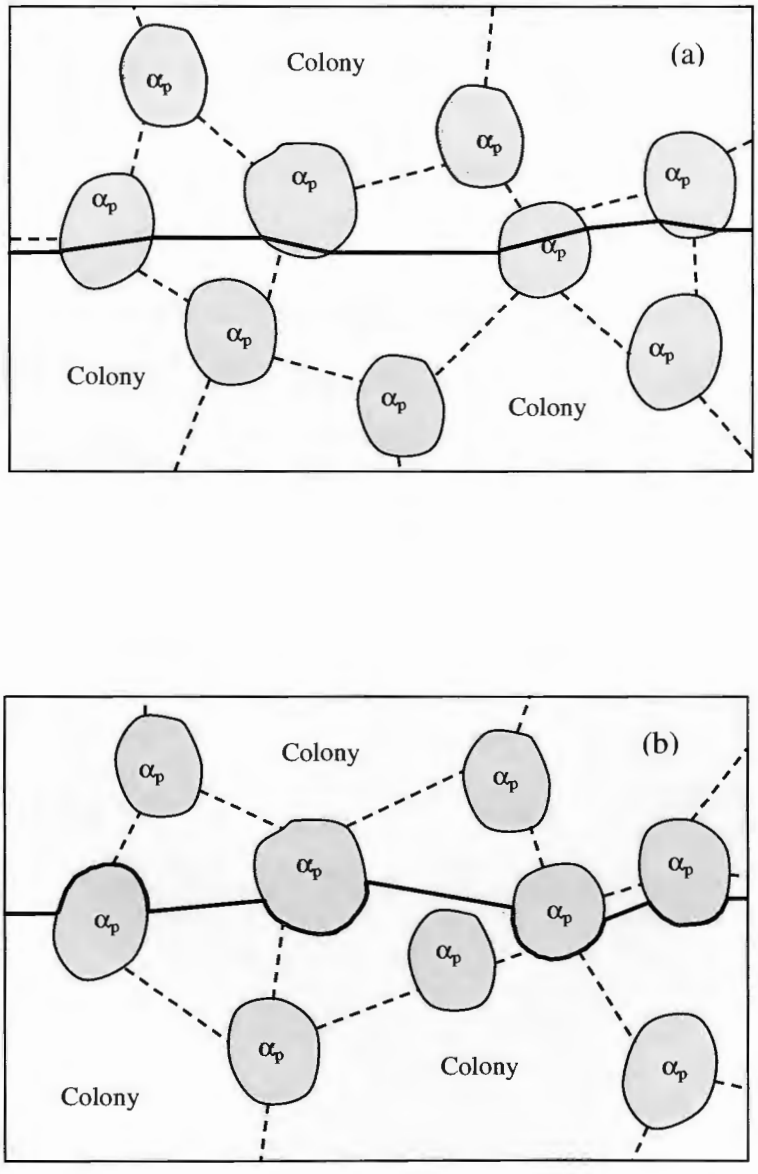

Figure 4-11: Schematic of possible crack path in both α/β colony and primary alpha: (a) trans-colony / trans-alpha particle; (b) trans-colony / inter-alpha boundary.

3.2 Summary of Chapter 4 Results

The following conclusions may be drawn from the obtained results:

1. FCGR increases with decreasing loading frequency independent of the microstructure.
2. At loading rates 10 Hz and 0.05 Hz, microstructure differences cause small changes in the FCGR
3. Pure fatigue dominates the fracture mode for test condition 10 Hz and 0.05 Hz at 650°C; fracture mechanisms for these conditions are trans-colony and trans-alpha particle.
4. Creep dominates the fracture mode for test condition 0.003 Hz at 650°C; fracture mechanisms for these conditions are trans-colony and inter-alpha boundary.

Appendix A

Basic Mechanisms of Creep and Fatigue Fracture

Creep and fatigue failure are critical degradation mechanisms that occur in turbine engine components. Cyclic fluctuating loading conditions at elevated temperature can ultimately cause failure at stresses considerable lower than those required under monotonic loading. Fatigue and creep crack growth occurs in three stages: (1) localized damage leading to crack initiation, known as primary creep; (2) crack growth, also called steady-state creep; (3) and final tensile rupture or tertiary creep. Figures A-1 and A-2 show the typical shapes of creep and fatigue crack growth curves, respectively. Factors that influence crack initiation include the material microstructure, the applied mean stress and the surrounding environment. During the second stage, microstructure and the thickness of the material may play a role, however, the major contributors in crack propagation involve combinations of environment, temperature, mean stress and loading frequency. Failure in the final stage can be caused by the material microstructure and/or thickness as well as by the applied mean stress.

To better understand the causes of failure, creep and fatigue must be looked at an atomic level. There are two mechanisms of creep: that gives the power-law behavior and diffusional creep that gives linear viscous creep. In dislocation creep, dislocation movement is opposed by the intrinsic lattice resistance or the obstructing effect of obstacles such as solute atoms, precipitates, and/or other dislocations. At elevated temperatures, diffusion of atoms can release dislocations

from its obstacles, designated as dislocation climb, which in turn glide on the next slip. This process is called dislocation creep. Figure A-3 is a schematic representation showing dislocation climb followed by dislocation glide.

Linear-viscous or diffusion creep occurs when dislocations are not involved. Instead, atoms diffuse from grain face to grain face due to grain elongation in response to the applied stresses. Figure A-4 is a schematic representation of diffusion creep. At elevated temperatures, this diffusion takes place through the crystal. Furthermore, when large grains are present, grain boundary sliding is required as an accessory to this process.

Fatigue failure, as in creep failure, can occur in several ways. For the purpose of this study, failure is focused on low-cycle fatigue, which is the main cause of fatigue failure in core components of nuclear reactors, airframes, turbine components, as well as any other component subjected to occasional overloads. When subjected to low-cycle fatigue loading, crack growth can occur by ductile tearing or by cleavage. Figures A-5 and A-6 are schematic representations of crack propagation by ductile tearing and cleavage, respectively. Ductile tearing takes place when plastic flow around small inclusions causes elongated cavities. As plastic flow progresses, these cavities link up, and the crack advances causing ductile tearing. During this process the crack tip changes from sharp to blunt. When little plastic deformation occurs local stresses built up at the crack tip that break apart the interatomic bonds. As the crack spreads between pair of atom planes, it gives raise to an atomically flat surface by cleavage. This fracture mechanism occurs primarily in brittle materials and at low temperatures. However,

metals with FCC structures, such as copper, lead and aluminum, usually fail by cleavage independently of the service temperature. In metals not having an FCC structure, the motion of dislocations is assisted by thermal agitation of the atoms giving origin to creep. A couple of mechanisms caused by creep and fatigue include intergranular and transgranular fracture, seen in figure A-7.

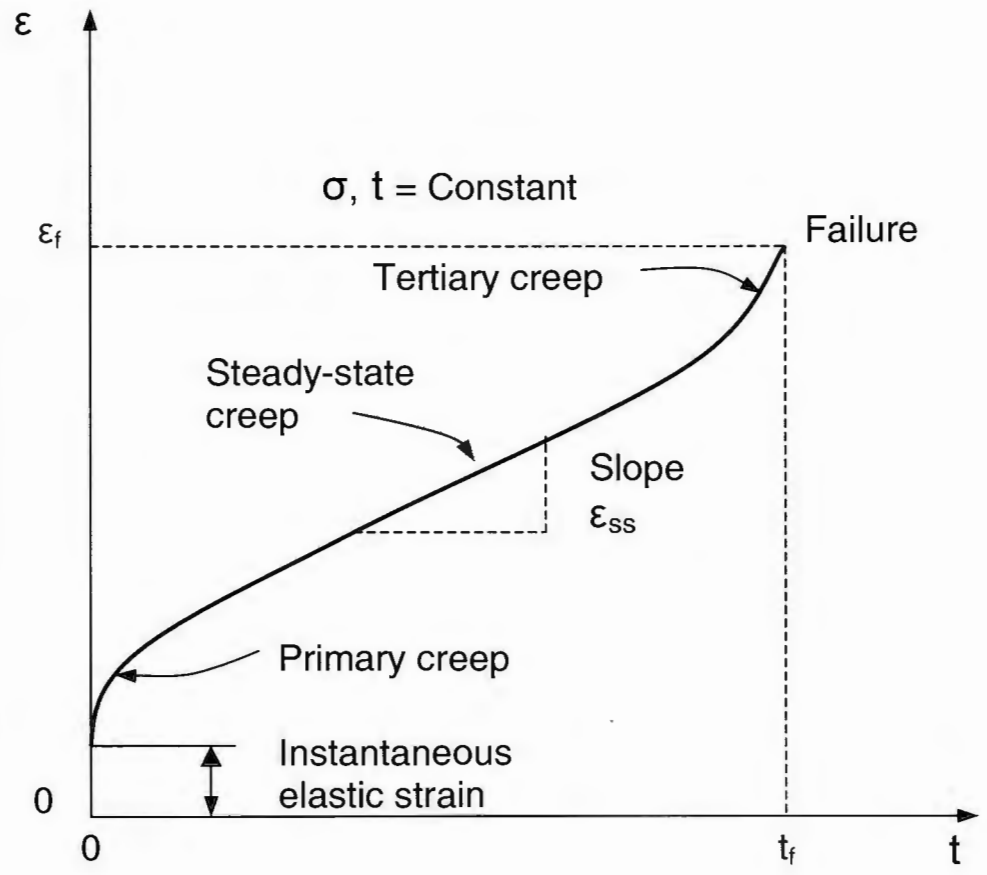

Figure A-1: Typical shape of a creep curve

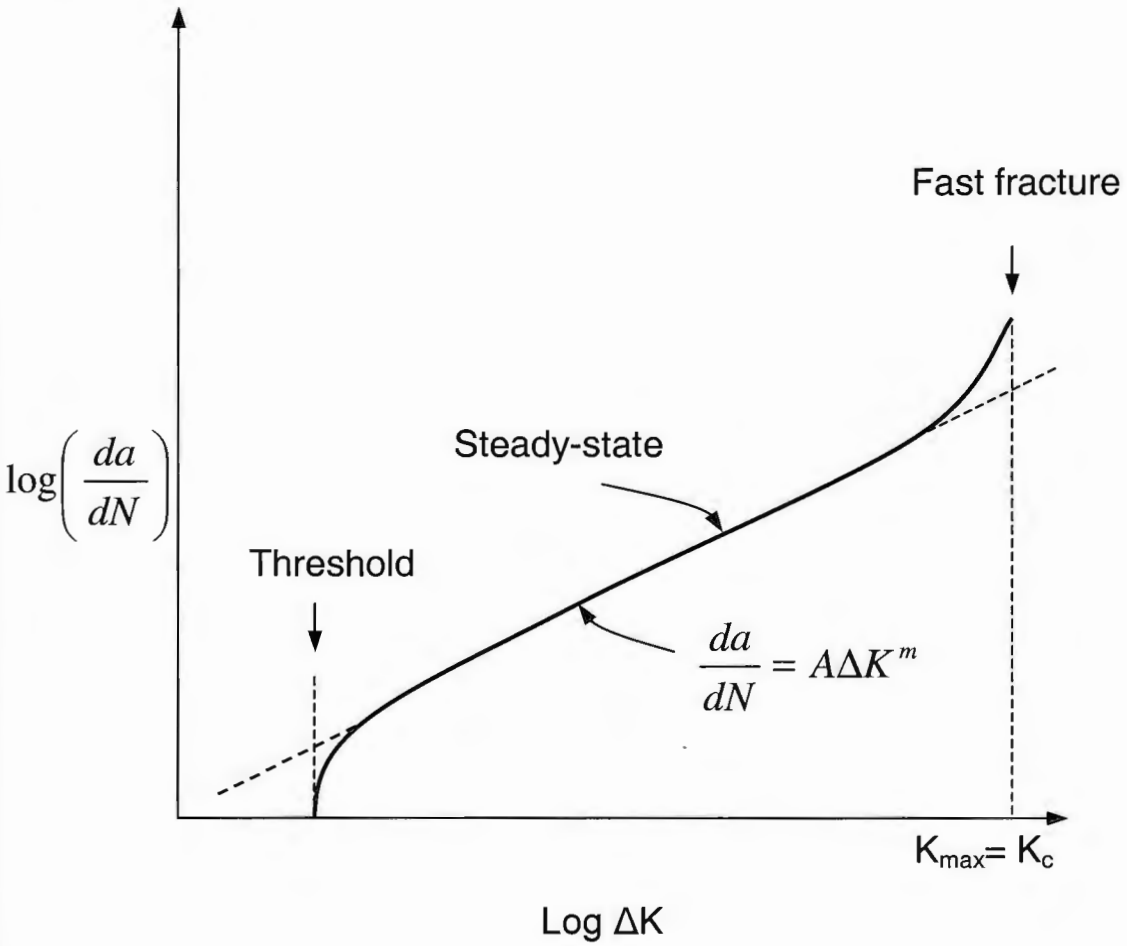

Figure A-2: Typical shape of a fatigue curve

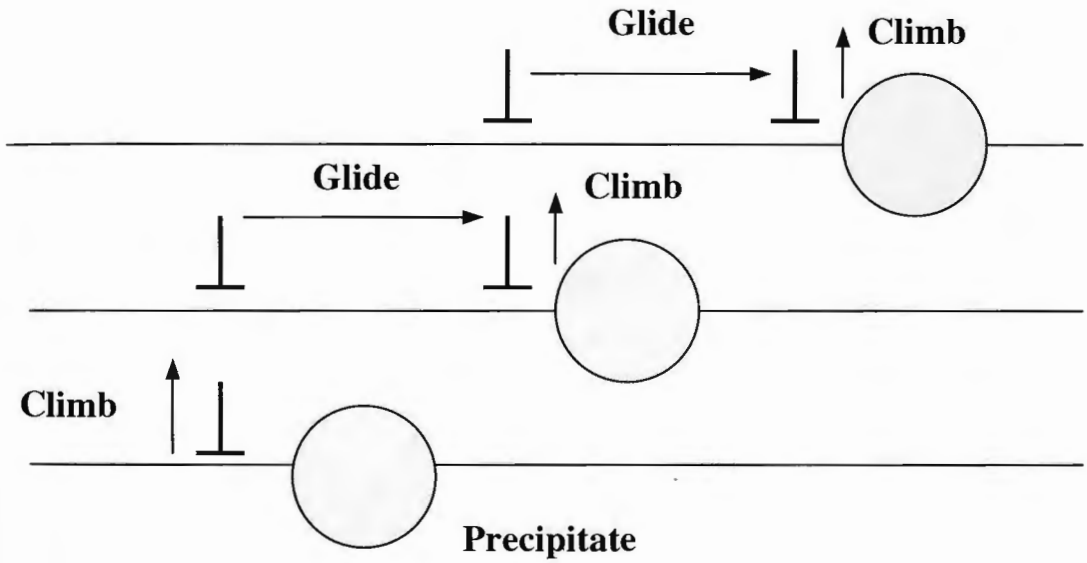

Figure A-3: Schematic representation of creep cause by climb-glide sequence.

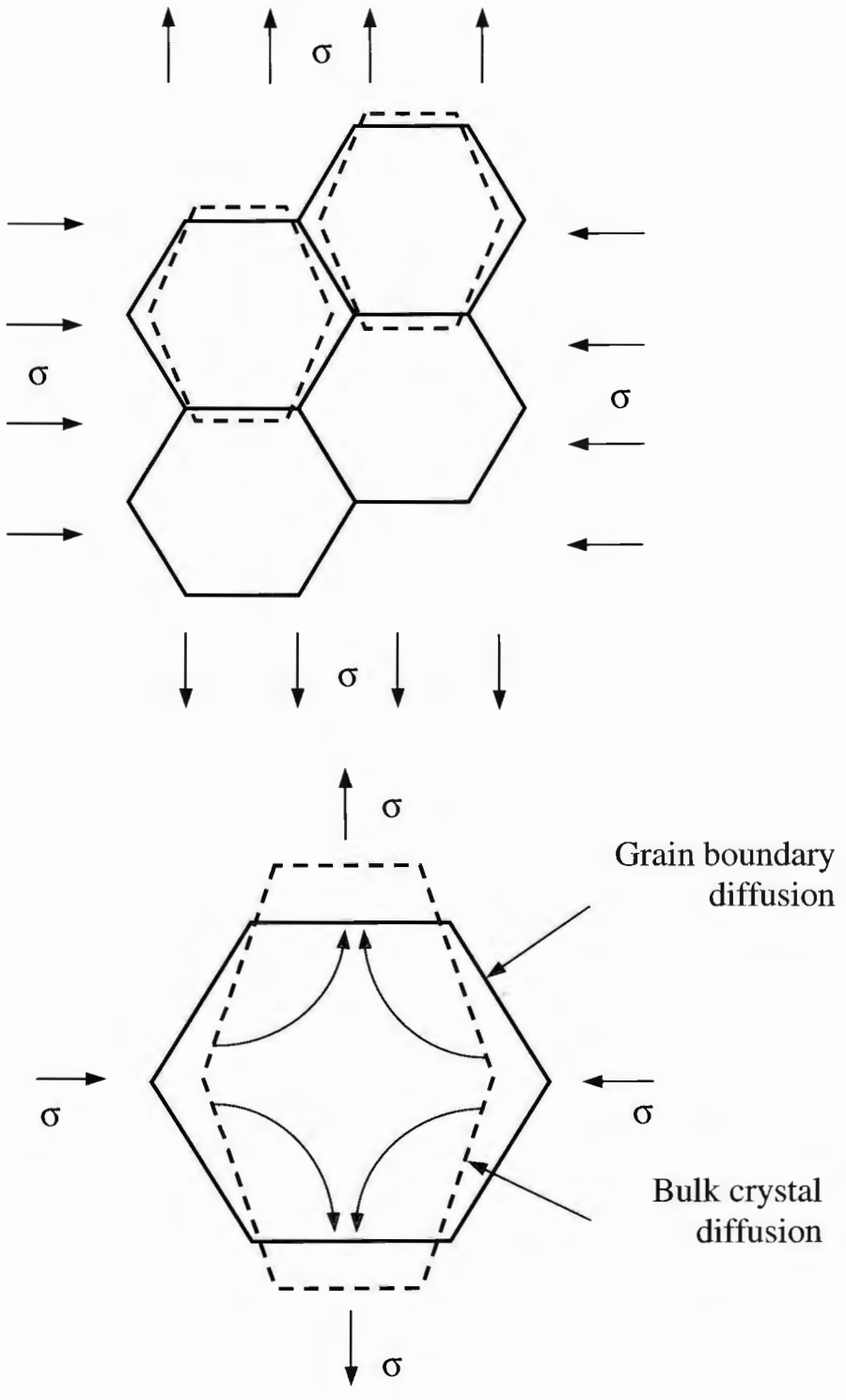

Figure A-4: Schematic representation of diffusion creep.

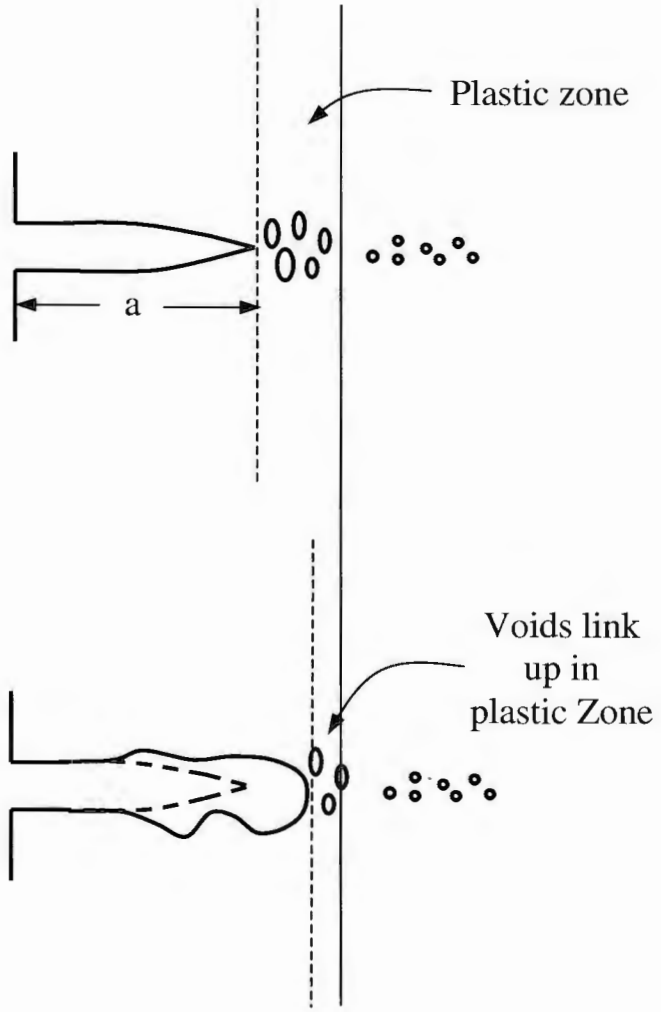

Figure A-5: Schematic representation of crack propagation by ductile tearing.

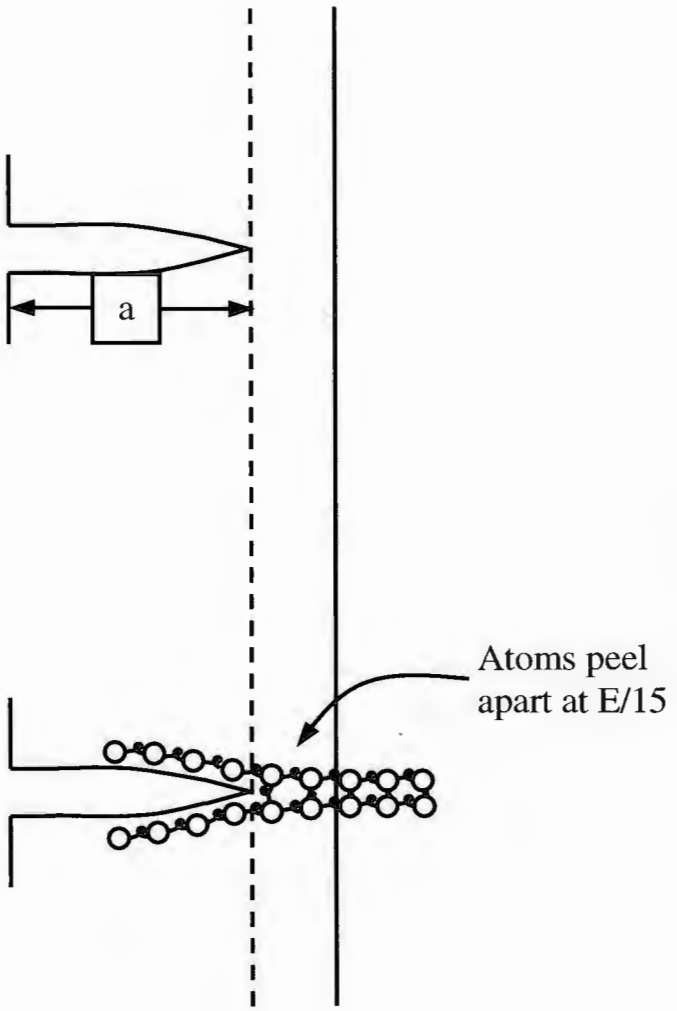

Figure A-6: Schematic representation of crack propagation by cleavage.

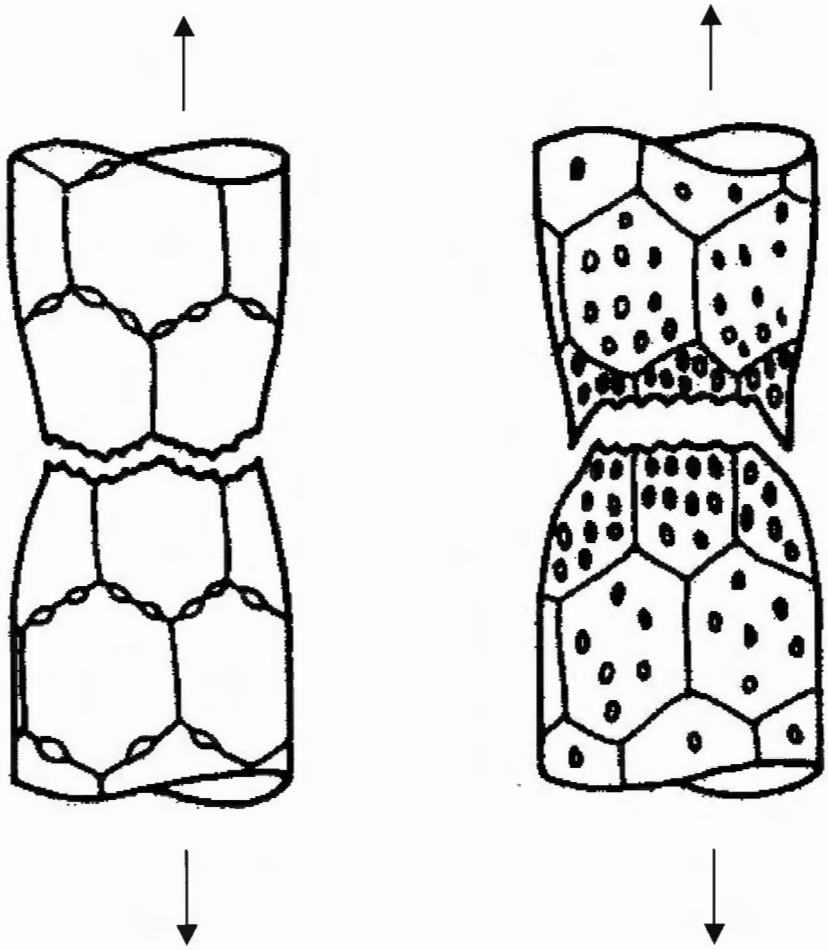

Figure A-7: Schematic representation of intergranular and transgranular fracture mechanisms.

List of references

1. Avallone, E. A.; Baumeister III, T. *Marks Standard Handbook for Mechanical Engineers*, Tenth Edition. New York: McGraw-Hill; 1996, pp. 6-91.

2. Titanium Alloys for Aerospace. *Advanced Materials & Processes*. Ohio: Metal Park; 1999.

3. Ruppen, J. A.; Hoffmann, C. L.; Radhakrishnan, V. M.; Evily, A. J. *The Effect of Environment and Temperature on the Fatigue Behavior of Titanium Alloys–in Fatigue, Environment, and Temperature Effects*. J. J. Burke and V. Weiss, New York: Plenum Press; 1980.

4. Eylon, D.; Fujishiro, S.; Postans, P. J.; Froes, F. H. High-Temperature Titanium Alloys—A Review. *Titanium Technology: Present Status and Future Trends*, Titanium Development Association, 1985, pp. 87-93.

5. Boyer, R. R. An Overview on the Use of Titanium in the Aerospace Industry, *Materials Science and Engineering A213*, 1996, pp. 103-114.

6. Shridar, G.; Kutumbarao, V. V.; Sarma, D. S. The Influence of Heat Treatment on the Structure of a Near-α titanium Alloy. *Metallurgical Transactions 18A*, May, 1987, pp. 877-891.

7. Gregory, J. K. Fatigue Crack Propagation in Titanium Alloys. *Handbook of Fatigue Crack Propagation in Metallic Structures*. Edited by A. Carpinteri. Elsevier Science B. V., 1994, p. 281.

8. Polmear, I. J. *Light Alloys—Metallurgy of the Light Metals*. Edwar Arnold, London, 1998, pp. 167-175.

9. Lütjering, G. Property Optimization Through Microstructural Control in Titanium and Aluminum Alloys. *Materials Science & Engineering A263*, 1999, pp.117-126.

10. *Titanium and Titanium Alloys*. Compiled by Consulting Editor J. Donachie, Jr. Metals Park, Ohio. American Society of Metals, 1982.

11. Weiss, I.; Semiatin, S. L. Thermomechanical Processing of Alpha Titanium Alloys—An Overview. *Materials Science & Engineering A263*, 1999, pp. 243-256.

12. Collings, E. W. Applied Superconductivity, *Metallurgy and Physics of Titanium Alloys, Volume I.* New York: Plenum Press; 1986.

13. Lütjering, G. Influence of Processing on microstructure and Mechanical Properties of (α + β) Titanium Alloys. *Materials Science & Engineering A243*, 1998, pp. 32-45.

14. Boyer, R. R.; Lütjering, G. Heat Treatment of Titanium Alloys: Overview. *Advances in the Science and Technology of Titanium Alloy Processing.* Edited by I. Weiss et al, The Minerals, Metals & Materials Society, 1997, p. 349.

15. Gregory, J. K. Fatigue Crack Propagation in Titanium Alloys, *Handbook of Fatigue Crack Propagation in Metallic Structures.* A. Carpinteri: Elsevier Science; 1994.

16. Bloyce, A.; Morton, P. H.; Bell, T. Surface Engineering of Titanium and Titanium Alloys, Surface Engineering, Volume 5, *ASM Handbook.* ASM International, 1995.

17. Ashby, M. F.; Jones, D. R. *Engineering Materials 1, An Introduction to Their Properties & Applications.* Second Edition. Butterworth-Heinemann, 1996.

18. Park, J. S. et al. The Effects of Processing on the Properties of Forgings for Two New High Temperature Titanium Alloys. *Sixth World Conference on Titanium Proceedings, Part I.* Société Française de Métallurgie; 1988; pp. 1283-1288.

19. Shridar, G.; Sarma, D. S. Structure and Properties of a β solution treated, Quenched, and Aged Si-Bearing Near-α Titanium Alloy. *Metallurgical Transactions A, Volume 20A*, January; 1989.

20. Ramachandra, C.; Singh, A. K.; Sarma, G. M. Microstructural Characterization of Near-α Titanium Alloy Ti-6Al-4Sn-4Zr-0.70Nb-0.50Mo-0.40Si. *Metallurgical Transactions A, Volume 24A*, June; 1993.

21. Singh, N.; Prasad, N.; Singh, V. Communications on the Occurrence of Dynamic Strain Aging in Near-Alpha Alloy Ti-5.8Al-4Sn-3.5Zr-0.7Nb-0.5Mo-0.35Si. *Metallurgical and Materials Transactions 30A*, 1999, p. 2547.

22. Paton, N. E.; Mahoney, M. W. Creep of Titanium-Silicon Alloys. *Metallurgical Transactions 7A*, November, 1976, p. 1685.

23. Ramachandra, C.; Singh, V. Effect of Silicides on tensile Properties and Fracture of Alloy Ti-6Al-5Zr-0.50Mo-0.25Si from 300 to 823K. *Journal of Materials Science 23*, 1988, pp. 835-841.

24. Neal, D. F. *Titanium Science and Technology*. Edited by G. Lütjering, U. Zwicker and W. Bunk. DGM, Oberusel, 1984, pp. 2419-2424.

25. Maier, H. J. High Temperature Fatigue of Titanium Alloys. *Materials at High temperatures 15(1)*, 1998, pp. 3-14.

26. Hardt, S.; Maier, H. J.; Christ, H. J. High-Temperature Fatigue Damage Mechanisms in Near-α Titanium Alloy IMI 834. *International Journal of Fatigue 21*, 1999, pp. 779-789.

27. Pototzky, P.; Maier, H. J.; Christ, H. J. Thermomechanical Fatigue Behavior of the High-Temperature Titanium Alloy IMI 834. *Metallurgical and Materials Transactions 29A*, December, 1998, p. 2995.

28. Maier, H. J.; Teteruk, R. G.; Christ, H. J. Modeling Thermomechanical Fatigue Life of High-Temperature Titanium Alloy IMI 834. *Metallurgical and Materials Transactions 31A*, February, 2000, p. 431.

29. Singh, N.; Gouthama; Singh, V. Low Cycle Fatigue of Ti Alloy 834 at Room Temperature. *Materials Science & Engineering A325*, 2002, pp. 324-332.

30. Kordisch, T.; Nowack, H. Life Prediction for the Titanium Alloy IMI 834 Under High Temperature Creep-Fatigue Loadings. *Fatigue & Fracture of Engineering & Structures 21*, 1998, pp. 47-63.

31. Es-Souni, M. Creep Deformation Behavior of Three High-Temperature Near α-Ti Alloys: IMI 834, IMI 829, IMI 685. *Metallurgical and Materials Transactions 32A*, February, 2001, p. 285-293.

32. Dowson, A. L.; Hollis, A. C.; Beevers, C. J. The Effect of Alpha-Phase Volume Fraction and Stress Ratio on the Fatigue Crack Growth Characteristics of the Near-Alpha IMI 834 Ti Alloy. *International Journal of Fatigue*, July, 1992, pp. 261-270.

33. Geary, B.; Bolam, V. J.; Jenkins, S. L.; Davies, D. P. High Temperature Titanium Sheet for Helicopter Exhaust Applications. Edited by P. A. Blenkinsop, W. A. Evans and H. M. Flowers. *Titanium '95: Science and Technology*. London, The Institute of Materials, 1996, p. 1638.

34. Spence, S. H.; Evans, W. J.; Medwell, N. Crack Growth Response of IMI 834 Under Variable Amplitude Loading. *International Journal of Fatigue 19*, 1997, pp. 33-41.

35. Kordisch, T.; Nowack, H. Creep-Fatigue Interaction and Life Behavior of the Titanium Alloy IMI 834 at 600°C. *8th World Conference on Titanium*, 22-26 October, Birmingham, UK, 1995, pp. 1179-1186.

36. Baxter, G. J.; Rainworth, W. M.; Grabowski, L. TEM Observations of fatigue Damage Accumulation at the Surface of the Near-α titanium Alloy IMI 834. *Acta Materialia, Volume 44*, No. 9, 1996, pp. 3453-3463.

37. Es-Souni, M. Creep Behavior of a High-Temperature Titanium Alloy Ti-5.8Al-4.0Sn-3.5Zr-0.7Nb-0.35Si-0.06C (Timetal 834) Part I. Primary and Steady State Creep. *Materials Characterization 46*, 2001, pp. 365-379.

38. Flower, H. M.; Lipscombe, K.; West, D. R. F. The Effect on the Structure and Mechanical Properties of an α+β Titanium Alloy. *Journal of Materials Science 17*, 1982, pp. 1221-1231.

39. Zhang, L.; Wu, J. Ti_5Si_3 and Ti_5Si_3-Based a Alloys: Alloying Behavior, Microstructure and Mechanical Property Evaluation. *Acta Materialia, Volume 46*, No. 10, 1998, pp. 3535-3546.

40. Zhang, X. D.; Wiezorek, J. M. K.; Baeslack III, W. A.; Evans, D. J.; Fraser, H. L. Precipitation of Ordered α_2 Phase in Ti-6-22-22 Alloy. *Acta Materialia, Volume 46*, No. 13, 1998, pp. 4485-4495.

41. Mendiratta, M. G.; Chakrabarti, A. K.; Roberson, J. A. Embrittlement of Ti-6Al-2Sn-4Zr-2Mo Alloy by α_2-Phase Precipitation. *Metallurgical Transactions, Volume 5*, August, 1974, pp. 1949-1951.

42. Gray III, G. T.; Luetjering, G.; Williams, J. C. The Influence on the Structure, Fracture, and Fatigue Crack Propagation Behavior of Ti-8.6 Wt Pct Al. *Metallurgical Transactions 21A*, January, 1990, pp. 95-105.

43. Liu, Z. Q.; Feng, J. Y.; Li, W. Z. Ti-Si Compounds Formation by High-Current Ion Implantation. Uncorrected Proof, *Journal of Crystal Growth*, 2002.

44. Ghosal, P.; Prasad, R.; Ramachandra, C. Microstructural Stability of the (α+β) Solution-Treated and Quenched Near-α titanium Alloy Ti-5.8Al-4Sn-3.5Zr-0.70Nb-0.50Mo-0.35Si-0.06C. *Metallurgical and Materials Transactions A, Volume 26A*, October, 1995, pp. 2751-2755.

45. Flower, H. M.; Swann, P.R.; West, D. R. F. Silicide Precipitation in the Ti-Zr-Al-Si System. *Metallurgical Transactions, Volume 2*, December, 1971, pp. 3289-3297.

46. Kotval P. S.; Calder, R. W. In Situ Identification of the Silicide Phase Super-α Titanium Alloys. *Metallurgical Transactions, Volume 3*, May, 1972, pp. 1308-1311.

47. Madsen A.; Andrieu, E.; Ghonem, H. Microstructural Changes During Aging of a Near-α Titanium Alloy. *Materials Science and Engineering A171*, 1993, pp. 191-197.

48. Foerch, R. A. *Mechanical Behavior and Micromechanisms of Creep-Fatigue Environment assisted Crack Growth in the Ti-1100 Alloy*, Master of Science in Mechanical Engineering and Applied Mechanics. University of Rhode Island; 1993.

49. Madsen, A.; Ghonem, H. Separating the Effects of Ti3Al and Silicide Precipitates on the Tensile and Crack Growth Behavior at Room Temperature and 593°C in the Near-Alpha Titanium Alloy. *Journal of Materials Engineering and Performance, Volume 4(3)*, June, 1995, pp. 301-307.

50. Lee, D. H.; Nam, S. W.; Choe, S. J. Effect of Microstructure on the High Temperature Low Cycle Fatigue of Near-α Ti-1100. *Materials Science and Engineering A291*, 2000, pp. 60-67.

51. Semiatin, S. L.; Seetharaman, V.; Weiss, I. The Thermomechanical Processing of Alpha/Beta Titanium Alloys. *Journal of Materials*, June; 1997; pp. 33-39.

52. Semiatin, S. L.; Seetharaman, V.; Weiss, I. Hot Working of Titanium Alloys-An Overview. *Advances in the Science and Technology of Titanium Alloy Processing*. Weiss et al: Metals and Materials Society; 1997; pp.3-73.

53. Madsen,A. *Effect of Aging on Uniaxial Tensile Characteristics of Fatigue Crack Growth Behavior in The Near-Alpha Titanium Alloys Ti-1100.* Masters of Science in Mechanical Engineering and Applied Mechanics. University of Rhode Island; 1993.

54. Beranger, A. S.; Feaugas, X.; Clavel, M. Low Cycle Fatigue of an α + β Titanium Alloy: Ti6246. *Materials Science and Engineering A172*, 1993, pp. 31-41.

55. Liu, K. W.; Zhang, J. S.; Wang, J. G.; Chen, G. L. Structure Evolution of Amorphous Ti-Al-Si During Annealing. *Journal of Non-Crystalline Solids, 215*, 1997, pp. 140-145.

56. Lim, J. Y.; McMahon, C. J.; Pope Jr., D. P.; Williams, J. C. *Metallurgical Transactions 7A*, 1976, p.139.

57. Blackburn, M. J. Transactions. *American Society for Metals, 239*, 1967, p. 1200.

58. Crossley, F. A. Transitions. *American Society for Metals, 242*, 1968, p. 726.

59. Williams, J. C. *Precipitation Processes in Solids*. Materials International Society Handbook, 1976, p. 191.

60. Chaze, A. M.; Béranger G.; Coddet, C. *Titanium Science and Technology*. DGM. Oberusel, 1984, pp. 2665-2672.

61. Ramachandra, C.; Singh, V. *Metallurgical Transactions A, Volume 13A*, 1982, pp. 771-775.

62. *ASM Handbook Volume 10*: Failure Analysis and Prevention, 8th edition. H. E. Boyer, editor, ASM International, Metals Park, Ohio1975, pp. 95-125.

63. *ASM Handbook Volume 19*: Fatigue and Fracture, A. C. Ruffin, editor, ASM International, Metals Park, Ohio, 1996.

64. Wulpi, D. J. *Understanding how Components Fail, Second Edition*, ASM International, Metals Park, Ohio, 1999.

Bibliography

Ashby, M. F.; Jones, D. R. *Engineering Materials 1, An Introduction to Their Properties & Applications. Second Edition.* Butterworth-Heinemann, 1996.

Avallone, E. A.; Baumeister III, T. *Marks Standard Handbook for Mechanical Engineers, Tenth Edition.* New York: McGraw-Hill; 1996, pp. 6-91.

Baxter, G. J.; Rainworth, W. M.; Grabowski, L. TEM Observations of fatigue Damage Accumulation at the Surface of the Near-α Titanium Alloy IMI 834. *Acta Materialia, Volume 44*, No. 9, 1996, pp. 3453-3463.

Bloyce, A.; Morton, P. H.; Bell, T. Surface Engineering of Titanium and Titanium Alloys. *Surface Engineering, Volume 5*, Materials International Society Handbook. ASM International, 1995.

Boyer, R. R. An Overview on the Use of Titanium in the Aerospace Industry, *Materials Science and Engineering A213*, 1996, pp. 103-114.

Boyer, R. R.; Lütjering, G. Heat Treatment of Titanium Alloys: Overview. *Advances in the Science and Technology of Titanium Alloy Processing.* Edited by I. Weiss et al, The Minerals, Metals & Materials Society, 1997, p. 349.

Collings, E. W. Applied Superconductivity, *Metallurgy and Physics of Titanium Alloys, Volume I.* New York: Plenum Press; 1986.

Dowson, A. L.; Hollis, A. C.; Beevers, C. J. The Effect of Alpha-Phase Volume Fraction and Stress Ratio on the Fatigue Crack Growth Characteristics of the Near-Alpha IMI 834 Ti Alloy. *International Journal of Fatigue*, July, 1992, pp. 261-270.

Es-Souni, M. Creep Behavior of a High-Temperature Titanium Alloy Ti-5.8Al-4.0Sn-3.5Zr-0.7Nb-0.35Si-0.06C (Timetal 834) Part I. Primary and Steady State Creep. *Materials Characterization 46*, 2001, pp. 365-379.

Es-Souni, M. Creep Deformation Behavior of Three High-Temperature Near α-Ti Alloys: IMI 834, IMI 829, IMI 685. *Metallurgical and Materials Transactions 32A*, February, 2001, p. 285-293.

Eylon, D.; Fujishiro, S.; Postans, P. J.; Froes, F. H. High-Temperature Titanium Alloys—A Review. *Titanium Technology: Present Status and Future Trends*, Titanium Development Association, 1985, pp. 87-93.

Flower, H. M.; Lipscombe, K.; West, D. R. F. The Effect on the Structure and Mechanical Properties of an α+β Titanium Alloy. *Journal of Materials Science 17*, 1982, pp. 1221-1231.

Flower, H. M.; Swann, P.R.; West, D. R. F. Silicide Precipitation in the Ti-Zr-Al-Si System. *Metallurgical Transactions, Volume 2*, December, 1971, pp. 3289-3297.

Foerch, R. A. *Mechanical Behavior and Micromechanisms of Creep-Fatigue Environment Assisted Crack Growth in the Ti-1100 Alloy*, Master of Science in Mechanical Engineering and Applied Mechanics. University of Rhode Island; 1993.

Geary, B.; Bolam, V. J.; Jenkins, S. L.; Davies, D. P. High Temperature Titanium Sheet for Helicopter Exhaust Applications. Edited by P. A. Blenkinsop, W. A. Evans and H. M. Flowers. *Titanium '95: Science and Technology.* London, The Institute of Materials, 1996, p. 1638.

Ghosal, P.; Prasad, R.; Ramachandra, C. Microstructural Stability of the (α+β) Solution-Treated and Quenched Near-α titanium Alloy Ti-5.8Al-4Sn-3.5Zr-0.70Nb-0.50Mo-0.35Si-0.06C. *Metallurgical and Materials Transactions A, Volume 26A*, October, 1995, pp. 2751-2755.

Gray III, G. T.; Luetjering, G.; Williams, J. C. The Influence on the Structure, Fracture, and Fatigue Crack Propagation Behavior of Ti-8.6 Wt Pct Al. *Metalurgical Transactions 21A*, January, 1990, pp. 95-105.

Gregory, J. K. Fatigue Crack Propagation in Titanium Alloys. *Handbook of Fatigue Crack Propagation in Metallic Structures.* Edited by A. Carpinteri. Elsevier Science B. V., 1994, p. 281.

Hardt, S.; Maier, H. J.; Christ, H. J. High-Temperature Fatigue Damage Mechanisms in Near-α Titanium Alloy IMI 834. *International Journal of Fatigue 21*, 1999, pp. 779-789.

Kordisch, T.; Nowack, H. Creep-Fatigue Interaction and Life Behavior of the Titanium Alloy IMI 834 at 600°C. *8th World Conference on Titanium*, 22-26 October, Birmingham, UK, 1995, pp. 1179-1186.

Kordisch, T.; Nowack, H. Life Prediction for the Titanium Alloy IMI 834 Under High Temperature Creep-Fatigue Loadings. *Fatigue & Fracture of Engineering & Structures 21*, 1998, pp. 47-63.

Kotval P. S.; Calder, R. W. In Situ Identification of the Silicide Phase Super-α Titanium Alloys. *Metallurgical Transactions, Volume 3*, May, 1972, pp. 1308-1311.

Liu, Z. Q.; Feng, J. Y.; Li, W. Z. Ti-Si Compounds Formation by High-Current Ion Implantation. Uncorrected Proof, *Journal of Crystal Growth*, 2002.

Lütjering, G. Influence of Processing on microstructure and Mechanical Properties of (α + β) Titanium Alloys. *Materials Science & Engineering A243*, 1998, pp. 32-45.

Lütjering, G. Property Optimization Through Microstructural Control in Titanium and Aluminum Alloys. *Materials Science & Engineering A263*, 1999, pp.117-126.

Madsen A.; Andrieu, E.; Ghonem, H. Microstructural Changes During Aging of a Near-α Titanium Alloy. *Materials Science and Engineering A171*, 1993, pp. 191-197.

Madsen, A.; Ghonem, H. Separating the Effects of Ti_3Al and Silicide Precipitates on the Tensile and Crack Growth Behavior at Room Temperature and 593°C in the Near-Alpha Titanium Alloy. *Journal of Materials Engineering and Performance, Volume 4(3)*, June, 1995, pp. 301-307.

Maier, H. J. High Temperature Fatigue of Titanium Alloys. *Materials at High Temperatures 15(1)*, 1998, pp. 3-14.

Maier, H. J.; Teteruk, R. G.; Christ, H. J. Modeling Thermomechanical Fatigue Life of High-Temperature Titanium Alloy IMI 834. *Metallurgical and Materials Transactions 31A*, February, 2000,.p. 431.

Mendiratta, M. G.; Chakrabarti, A. K.; Roberson, J. A. Embrittlement of Ti-6Al-2Sn-4Zr-2Mo Alloy by α_2-Phase Precipitation. *Metallurgical Transactions, Volume 5*, August, 1974, pp. 1949-1951.

Neal, D. F. *Titanium Science and Technology*. Edited by G. Lütjering, U. Zwicker and W. Bunk. DGM, Oberusel, 1984, pp. 2419-2424.

Park, J. S. et al. The Effects of Processing on the Properties of Forgings for Two New High Temperature Titanium Alloys. *Sixth World Conference on Titanium Proceedings, Part I.* Société Française de Métallurgie; 1988; pp. 1283-1288.

Paton, N. E.; Mahoney, M. W. Creep of Titanium-Silicon Alloys. *Metallurgical Transactions 7A*, November, 1976, p. 1685.

Polmear, I. J. *Light Alloys—Metallurgy of the Light Metals.* Edwar Arnold, London, 1998, pp. 167-175.

Pototzky, P.; Maier, H. J.; Christ, H. J. Thermomechanical Fatigue Behavior of the High-Temperature Titanium Alloy IMI 834. *Metallurgical and Materials Transactions 29A*, December, 1998, p. 2995.

Ramachandra, C.; Singh, A. K.; Sarma, G. M. Microstructural Characterization of Near-a Titanium Alloy Ti-6Al-4Sn-4Zr-0.70Nb-0.50Mo-0.40Si. *Metallurgical Transactions A, Volume 24A*, June; 1993.

Ramachandra, C.; Singh, V. Effect of Silicides on tensile Properties and Fracture of Alloy Ti-6Al-5Zr-0.50Mo-0.25Si from 300 to 823K. *Journal of Materials Science 23*, 1988, pp. 835-841.

Ruppen, J. A.; Hoffmann, C. L.; Radhakrishnan, V. M.; Evily, A. J. *The Effect of Environment and temperature on the Fatigue Behavior of Titanium Alloys–in Fatigue, Environment, and Temperature Effects.* J. J. Burke and V. Weiss, New York: Plenum Press; 1980.

Shridar, G.; Kutumbarao, V. V.; Sarma, D. S. The Influence of Heat Treatment on the Structure of a Near-α titanium Alloy. *Metallurgical Transactions 18A*, May, 1987, pp. 877-891.

Shridar, G.; Sarma, D. S. Structure and Properties of a b solution treated, Quenched, and Aged Si-Bearing Near-α Titanium Alloy. *Metallurgical Transactions A, Volume 20A*, January; 1989.

Singh, N.; Gouthama; Singh, V. Low Cycle Fatigue of Ti Alloy 834 at Room Temperature. *Materials Science & Engineering A325*, 2002, pp. 324-332.

Singh, N.; Prasad, N.; Singh, V. Communications on the Occurrence of Dynamic Strain Aging in Near-Alpha Alloy Ti-5.8Al-4Sn-3.5Zr-0.7Nb-0.5Mo-0.35Si. *Metallurgical and Materials Transactions 30A*, 1999, p. 2547.

Spence, S. H.; Evans, W. J.; Medwell, N. Crack Growth Response of IMI 834 Under Variable Amplitude Loading. *International Journal of Fatigue 19*, 1997, pp. 33-41.

Titanium Alloys for Aerospace. *Advanced Materials & Processes.* Ohio: Metal Park; 1999.

Titanium and Titanium Alloys. Compiled by Consulting Editor J. Donachie, Jr. Metals Park, Ohio. American Society of Metals, 1982.

Weiss, I.; Semiatin, S. L. Thermomechanical Processing of Alpha Titanium Alloys—An Overview. *Materials Science & Engineering A263*, 1999, pp. 243-256.

Zhang, L.; Wu, J. Ti_5Si_3 and Ti_5Si_3-Based α Alloys: Alloying Behavior, Microstructure and Mechanical Property Evaluation. *Acta Materialia, Vol. 46*, No. 10, 1998, pp. 3535-3546.

Zhang, X. D.; Wiezorek, J. M. K.; Baeslack III, W. A.; Evans, D. J.; Fraser, H. L. Precipitation of Ordered α_2 Phase in Ti-6-22-22 Alloy. *Acta Materialia, Volume 46*, No. 13, 1998, pp. 4485-4495.